Scientific Report No. 48

A STUDY OF RAIN EFFECTS ON ELECTROMAGNETIC WAVES IN THE 1-600 GHz RANGE

by

Charles Henry Zufferey

M.S. Thesis 1972

Reprinted 1979

A STUDY OF RAIN EFFECTS ON ELECTROMAGNETIC WAVES IN THE 1-600 GHZ RANGE.

by

Charles Henry Zufferey
Ingénieur Diplomé de l'Ecole Polytechnique
Fédérale, Lausanne, Switzerland, 1970

A thesis submitted to the Faculty of the Graduate School of the University of Colorado in partial fulfillment of the requirements for the degree of
Master of Science
Department of Electrical Engineering
1972

Zufferey, Charles Henry (M.S., Electrical Engineering)

A Study of Rain Effects on Electromagnetic Waves in the 1-600 GHz Range.

Thesis directed by Professor Warren L. Flock.

Intense rain is the most serious factor limiting the propagation of electromagnetic waves in the 10 to 300 GHz frequency range. Absorption by liquid water and raindrop dimensions that are comparable with the incident wavelength are responsible for the severity of the effects in this frequency range.

A Debye model is shown to describe adequately the absorption process for frequencies up to 300 GHz. A fast computer program designed to evaluate the Mie coefficients, for the case of diffraction by a single spherical water drop, is presented. The behavior of the complex forward-scattering function is then analyzed as a function of frequency and raindrop diameter. The influence of temperature on the real and imaginary parts of this function is also investigated.

Propagation of electromagnetic energy through rain is studied for the case of a plane wave. The statistically average parameters of a coherent signal, that has propagated through a slab of uniform rain, are obtained by using a Laws and Parsons drop-size distribution. A simple model, in terms of an equivalent refractive index or a complex transfer function, describes the effect of the slab of rain on the amplitude and phase of the signal. This model is extended to the case of non-uniform rain, along a path of length L, by defining a path-averaged rainfall rate. Under certain restrictions regarding the intensity of the diffuse energy, this model can be used to describe incoherent propagation.

Logarithmic and linear regression models that approximate the variation of the attenuation coefficient as a function of rainfall rate are discussed. A comparison of the Laws and Parson theoretical model and measured average attenuations, published in the literature since Medhurst's survey (1965), shows reasonable agreement. The crude manner in which meteorological data are handled, however, makes this comparison difficult.

Computations of the average excess propagation time as a function of frequency do not indicate any appreciable bandwidth limitations resulting from delay distortion.

The influence of temperature, drop-size distribution, and uncertainty of drop velocity on the average propagation parameters are treated in this study. Some suggestions for future experiments are given.

This abstract is approved as to form and content.

Signed Warren L. Flock
Faculty member in charge of thesis.

ACKNOWLEDGMENTS

The author wishes to express his sincere gratitude to Dr. Warren L. Flock who supervised this work and acted as Chairman of his thesis committee.

To Dr. Moody C. Thompson, Jr., he is indebted for suggesting the subject of this study and making it possible to work in collaboration with his group at the Institute for Telecommunication Sciences (ITS) in Boulder. The cooperation with ITS has proven to be an invaluable educational experience.

Special thanks are due to L.E. Vogler from ITS and to Dick Brockway from Westinghouse Georesearch Laboratories in Boulder for many stimulating, thought provocating discussions.

The subroutine QUEUES provided by E.J. Dutton (ITS) was of inestimable value in testing the results of our own program.

Dr. S.W. Maley and Dr. P. Beckmann served on my thesis committee.

Miss Ellen J. Mohr is to be congratulated for the perfect, accurate typing of the final version of this thesis.

This work was supported jointly by the National Aeronautics and Space Administration (NASA) and the European Space Research Organization (ESRO).

TABLE OF CONTENTS

LIST OF FIGURES

LIST OF TABLES

CHAPTER 1

INTRODUCTION

1.1 The potential of millimeter waves.

The development of telecommunication systems has been characterized by the use of higher and higher frequencies, in an attempt to meet the never satisfied demand for increased channel capacity (Martin 1971). There is no leveling in sight of this trend towards higher frequencies, especially in view of the needs of high speed digital data transmission, advanced space exploration programs, and broadband video transmission, either for communication (picturephone) or for monitoring the environment. All these new tasks require high transmission rates which can be accomodated only by the use of higher carrier frequency.

The next unused region of the electromagnetic spectrum lies above 10 GHz, a domain that marks the transition from classical electromagnetic waves to optics. The main potentialities of this part of the spectrum are: a) large bandwidth capability, b) highly directive beams, obtained with relatively small antennas, c) low transmitter power requirement, and d) better penetration of media with high ion density. Some of these properties make those frequencies ideal for space communication systems.

Some microwave relay systems already use a frequency band near 11 GHz; short distance optical links operate in a quite satisfactory fashion in the near infrared as well as in the visible range. However, intermediate frequencies, especially those in the band ranging from 30 to 300 GHz, known as the EHF or the millimeter wavelength band, still lie idle despite their enormous potentialities; telecommunication systems using those frequencies seem to have a hard time passing beyond the stage of research and development. The reason for this slow evolution is to be found in the severe effects exerted on waves in this frequency band by the atmosphere (mainly the troposphere) and the lack of the meteorological information required for a reliable yet economic link design.

1.2. Atmospheric effects at cm and mm wavelengths.

The actual atmosphere (as opposed to free space) affects the amplitude, phase, and polarization of electromagnetic waves at short wavelengths. Among the physical phenomena that cause these effects are a) dispersive molecular absorption, the two main absorbers being water vapor and oxygen, b) refractive effects that cause amplitude and phase scintillations (rapid fading), c) thermal emission that increases the background noise level and, last but not least, d) scattering and absorption by hydrometeors.

Some of these effects, such as gaseous absorption, are very strongly frequency dependent; selective fading,

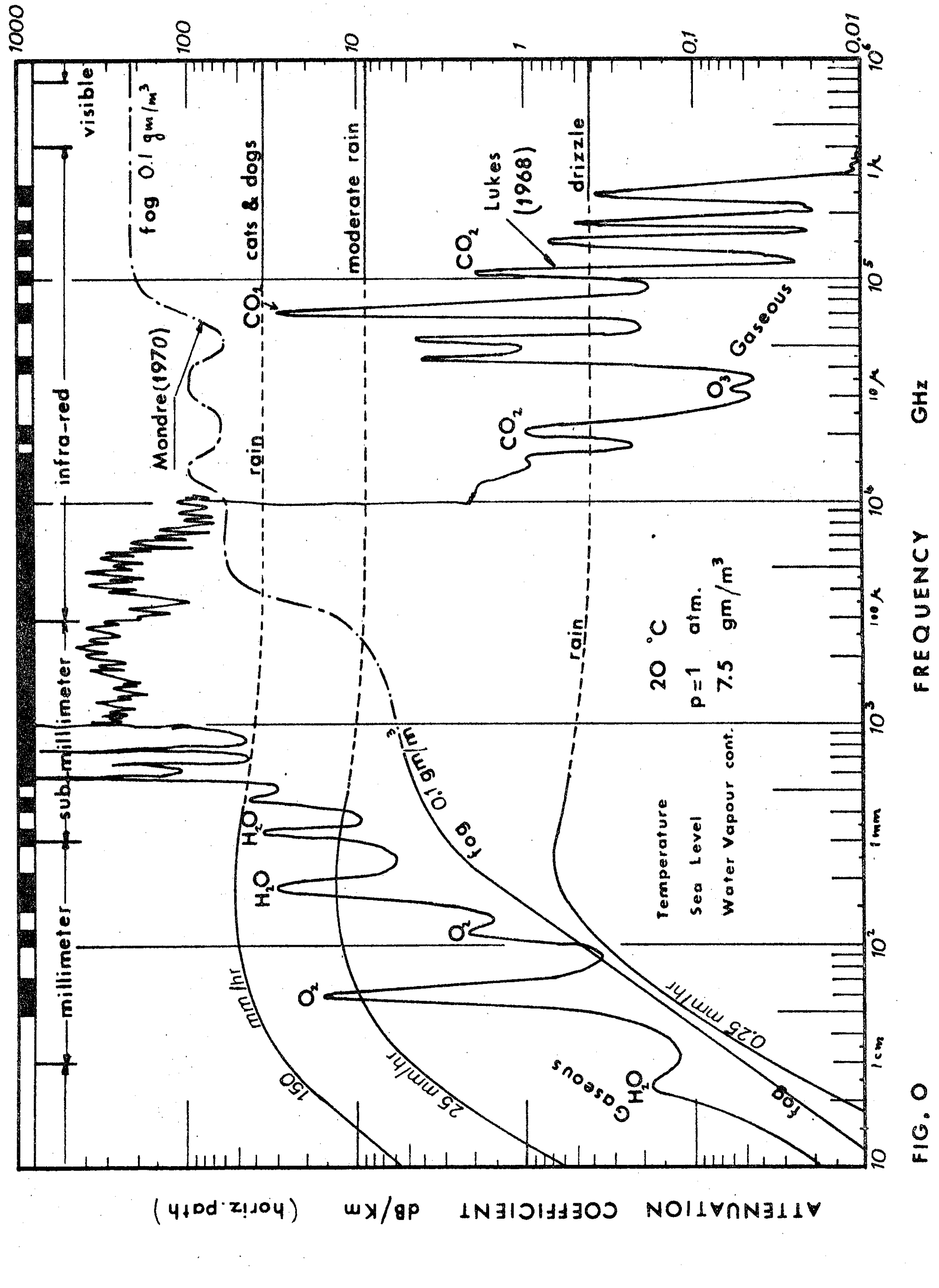

millimeter
sub-millimeter
infra-red
visible
fog 0.1 gm/m³
cats & dogs
moderate rain
drizzle
Lukes (1968)
Mondre (1970)
CO_2
O_3
Gaseous
H_2O
O_2
rain
150 mm/hr
25 mm/hr
0.25 mm/hr
fog
fog 0.1 gm/m³
20 °C
p=1 atm.
7.5 gm/m³
Temperature
Sea Level
Water Vapour cont.
1 cm
1 mm
100 μ
10 μ
1 μ
10
10^2
10^3
10^4
10^5
10^6
1000
100
10
1
0.1
0.01
FREQUENCY GHz
ATTENUATION COEFFICIENT dB/Km (horiz. path)

FIG. O

however, varies only slightly with frequency. Among all these effects, the one due to hydrometeors, especially rain, is certainly the most significant at centimeter and millimeter wavelengths (see Figure 0). As a matter of fact these effects may become so severe at high frequencies that transmission through the atmosphere may become impractical, except for certain applications, such as satellite communications, where advantage is taken of the relatively short path length through the rainy atmosphere. The effect of other hydrometeors is variable. Hail causes only a small attenuation compared to rain. The effect of snow depends on temperature, flake size, and water content. Fog and clouds can be treated as very light rains at microwave frequencies but not at optical frequencies (see Figure 0). Except for the case of melting hail or wet snow, the effects due to other hydrometeors are relatively minor at cm and mm wavelengths. Furthermore, since the frequency of occurence of such phenomena is very low compared to rain, their effects will not be discussed in this study.

1.3. The effects due to rain.

Condensed water in the atmosphere in the form of rain affects the propagation of electromagnetic waves in two ways: a) water absorbs part of the incident energy, which is thus converted into heat, b) raindrops scatter the electromagnetic energy. Considered from the point of view of its frequency of occurence and the magnitude of its effects, rain appears to be the most severe limiting factor for propagation of waves in the 10 to 100 GHz band. The very strong effects of rain are due to two important phenomena that occur in this frequency band:

a) Water exhibits a strong, relaxation-type, absorption characteristic in this range. The location of the peak of absorption is temperature dependent and shifts from about 13 GHz to 50 GHz (see Appendix 1).

b) Raindrops, which range in diameter from 0.5 to 7 mm, reach their Mie region in this band, i.e. the ratio D/λ is of the order of unity, yielding a maximum value for the various cross-sections.

This is not the case for fog, in which the drop diameters range from 0.1 to 100 microns and reach the Mie region only for infrared frequencies.

The problem of the interaction of electromagnetic energy with rain has two major aspects.

a) The first aspect is a purely <u>electromagnetic</u> problem, namely that of the interaction of a given shape and dimension. The solution of this problem is adequately known.

b) The second aspect is a <u>meteorological</u> problem, which involves the random distribution of raindrops in size, space, and time for a given rain.

> The amount of meteorological data needed to describe adequately such a medium would be prohibitively detailed and therefore seems impossible to gather; only a statistical approach is of practical interest.

Even when considering the simpler problem of uniform rain, the number of parameters governing electromagnetic propagation through the medium remains considerable. The main parameters are a) the polarization characteristic of the incident wave, b) the shape and dimension of the raindrop, c) the drop-size distribution, and d) the complex refractive index of water, which is itself a function of frequency and temperature. In the case of actual rain we must add the spatial and temporal distribution of the raindrops.

1.4. The scope of this study.

This study considers the spectral range from 1 to 600 GHz, where the interesting phenomena due to rain are supposed to happen. The study of this frequency spectrum has been undertaken in an attempt to evaluate the frequency dependence of rain effects on electromagnetic waves. A spherical shape has been adopted for the model of a raindrop, so that no polarization effects can be shown by using this model. References for treating the more complete problem of an oblate raindrop are however indicated along the text.

The theory used in this study is not new, although the attempt to formulate the propagation through rain in terms of a complex transfer function, a familiar concept to system analysts, is relatively modern. The main contribution of this study comes from the rather exhaustive analysis of the influence of the different parameters on the propagation constants. This analysis became possible after the design of a fast computer program (presented in Appendix 2) which allowed obtaining the results rather inexpensively. All the curves presented in this study (except where explicitly referenced) are drawn from original computations by the author.

The material has been arranged for presentation in the following way. Chapter 1 is the present introduction. Chapter 2 is a review of the complex refractive index of water in the frequency region of interest, in order to evaluate the accuracy of a Debye relaxation model. The main results of the electromagnetic problem are then presented in Chapter 3, for the case of a spherical water drop. The influence of different parameters such as temperature, drop diameter, are examined in this chapter. In Chapter 4 a model for studying coherent propagation through rain is presented in the form of a complex transfer function for a rainy atmosphere. Chapter 5 then deals with the imaginary part of the propagation constant or attenuation coefficient; a comparison of this model with measurements published in the literature since

Medhurst's survey (1965) is also included in this chapter. Chapter 6 examines the dispersive properties of rain (from the real part of the propagation constant) in an attempt to point out possible bandwidth limitations due to delay distortion. Chapter seven summarizes the chief conclusions from this study.

It may be worthwhile mentioning here that the results presented in this study include only the additional effects due to rain and neglect free space or clear atmosphere effects. Neither does this work deal with statistical properties of rainfall rates; the design of microwave links requires information about the maximum possible outage time. Obviously this information cannot be obtained from average effects; it must take into account the uncertainty of the model. It is hoped that the estimation of the influence of various parameters presented in this study may be useful in setting a bound to this uncertainty. A treatment of the statistical property of a signal emerging from rain has not yet been done satisfactorily.

CHAPTER 2

THE REFRACTIVE INDEX OF WATER AT CM AND MM WAVELENGTHS

2.1. Introduction

In this chapter, the dielectric properties of liquid water are critically reviewed. It is found that Debye's formula is suitable for calculations of rain effects in the centimeter and millimeter wavelength region. However, the same formula cannot be used for calculations in the submillimeter region, where resonant absorption phenomena take place.

2.2. Debye's formula

Liquid water exhibits some very strong, frequency dependent absorption in that part of the electromagnetic spectrum, that is of interest in this study. This phenomena may be explained in terms of reorientation of the water molecule dipole along the electric field, giving rise to non-resonant, viscously damped absorption.

Such behavior, for the case of a time-harmonic field, may be described by means of a complex dielectric constant, $\hat{\varepsilon}$, which is readily obtained from Maxwell's equations and has the form

$$\hat{\varepsilon} = (\varepsilon' - j\varepsilon'') = (\varepsilon_r - j \frac{\sigma\omega}{\varepsilon_o}) \qquad (2.1)$$

where

ε_r = is the relative dielectric constant,

σ = is the conductivity in mhos/m,

ω = $2\pi f$ is the angular frequency (rad/s)

ε_o = 8.85 (pF/m)

The theory introduced by Debye (1929), in his work on polar molecules, provides a formula of the form

$$\hat{\varepsilon}(\lambda,T) = \frac{\varepsilon_o(T) - \varepsilon_\infty}{1 + j\,\frac{\Delta\lambda(T)}{\lambda}} + \varepsilon_\infty \qquad (2.2)$$

where ε_o, ε_∞, $\Delta\lambda$ are temperature dependent parameters, adjusted to fit the experimental data and λ is the wavelength of the incident radiation, usually expressed in cm. Those parameters are listed in Table I, from Kerr (1951); notice the corrections that have been made to some parameters of his Table 8.8. Unfortunately, these mistakes, which certainly may be attributed to a misprint, have been carried on for decades (see for example Fowler and La Grone 1969).

More recently (1957), Grant et al. found better agreement between theory and experimental data when a double relaxation-type formula is used as in

$$\hat{\varepsilon}(\lambda,T) = \frac{\varepsilon_o - \varepsilon_\infty}{\left[1 + j\,\frac{\Delta\lambda}{\lambda}\right]^{(1-\alpha)}} + \varepsilon_\infty \qquad (2.3)$$

The best fit was obtained for α = .02; the other parameters as given in Table I.

However, calculations by Crane (1966) have shown less than 3% deviation between the two formulas at 0 °C,

T	ε_∞	$\Delta\lambda$ (cm)	ε_o	$\Delta\lambda$ (cm)	ε_∞
°C	Debye's form. (2.2)			Grant et al. (2.3)	
0	5.5[1)]	3.59	88	3.33	4.5[3)]
10	5.5	2.24	84	2.38	4.5
18	5.5	1.66	81	-	4.5
20	5.5	1.53	80	1.74	4.5
30	5.5	1.12[2)]	76.4	1.36	4.5
40	5.5	.859[2)]	73	1.09	4.5

TABLE I

Parameters for use in the complex dielectric constant formulas (2.2) and (2.3).

1.) Saxton later used a value of 4.9 for better fit (Saxton 1952).

2.) Values corrected from Kerr.

3.) A good fit is obtained using this value when α is taken as 0.02.

over the frequency range 8 - 70 GHz. Furthermore, a comparison of the rain scattering parameters, obtained using the two models, showed negligible differences. The weak effects of a variation of the refractive index on the rain scattering parameters has also been noticed by the author.

Because the differences are small and since most of the calculations reported are based on Debye's model, this latter formulation has been chosen for the present study.

The <u>complex refractive index</u> of liquid water is then defined in terms of the complex relative dielectric constant (2.2) as indicated by

$$\hat{m}(\lambda,T) = \sqrt{\mu\hat{\varepsilon}} = m' - jm'' \qquad (2.4)$$

where μ, the permeability of water, is taken as 1. It is a matter of simple algebraic manipulation to show that

$$m'' = \left[\left(\frac{\varepsilon'^2+\varepsilon''^2}{4}\right)^{\frac{1}{2}} - \frac{\varepsilon'}{2}\right]^{\frac{1}{2}} \qquad (2.5)$$

$$m' = \left[\left(\frac{\varepsilon'^2+\varepsilon''^2}{4}\right)^{\frac{1}{2}} + \frac{\varepsilon'}{2}\right]^{\frac{1}{2}} \qquad (2.6)$$

A computer subroutine, called DIELEC, that calculates the complex refractive index of water has been writtern as a function of λ and T. It uses the values of the parameters given in Table I for Debye's formula and has a built-in interpolation subroutine for intermediate

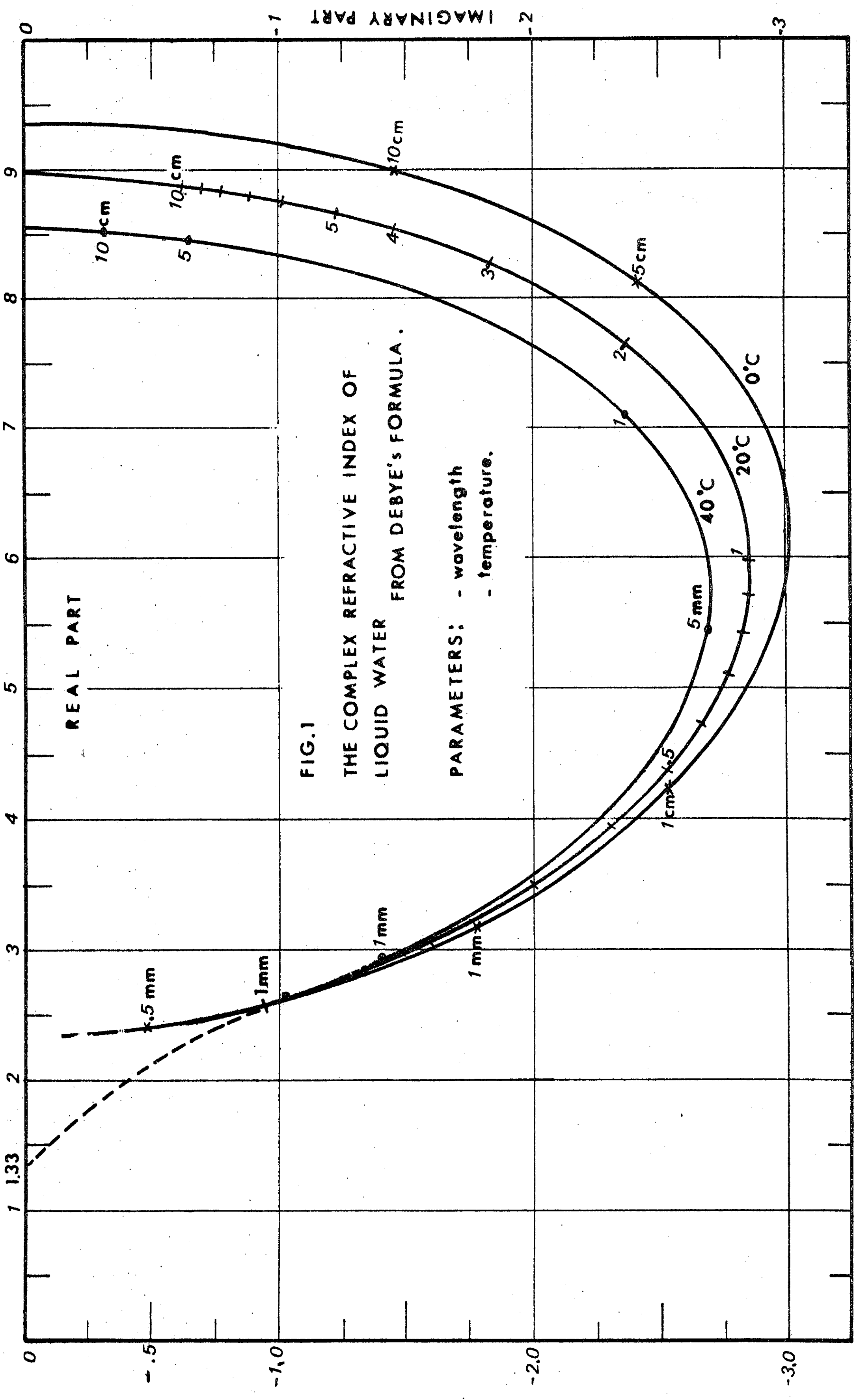

FIG.1

THE COMPLEX REFRACTIVE INDEX OF LIQUID WATER FROM DEBYE's FORMULA.

PARAMETERS: - wavelength
- temperature.

values of T.

2.3. Numerical computations

In Figure 1, the results of calculations are shown in the complex $\hat{m}$-plane, for three different temperatures (0,20, and 40 °C) and for values of λ ranging from 1 mm to 10 cm. A cartesian plot of the real and imaginary part of $\hat{m}$ versus frequency, together with some selected values of the refractive index, may be found in Appendix 1. From these plots, it appears that the strongest temperature dependence occurs for the longer wavelengths (1-10 cm). At very high frequency, this model doesn't give a value of $|\hat{m}|$ which approaches 1.33, the well-known refractive index of water at optical frequencies. An asymptotic value of 2.3 is reached for all temperatures instead. Thus, the question naturally arises, how far can this model be extrapolated?

2.4. Comparison of theory and measurements

Good agreement between the Debye model and measurements has been reported for frequencies up to 48.5 GHZ (0.62 cm) (Lane and Saxton 1952). Since the curves are very smooth, there seems to be good reason for extrapolating towards higher frequencies. To the author's knowledge, no measurements have been made between 6.2 mm and 2 mm. The only data between 2 mm and 70 μm are those by Stanevich and Yaroslavskii (1961) and those by Chamberlain et al. (1966). Both investigators find that

Debye's model predicts too much refraction and too little absorption in the submillimeter range.

A very complete survey of data for the refractive index of water in the 10 cm to 0.1 μm range has been published recently by Lukes (1968). In his Figure 5.a (page 46) the real and imaginary parts of the refractive index of water are plotted for the above mentioned range. The points for frequencies below 100 GHz are for a temperature of 10 °C; the others are for temperatures ranging from 10 to 20 °C. These curves have been obtained by selecting more than 550 data points among 20 reference sources; however, it is not always clear whether they are experimental or calculated points.

A comparison of Debye's model with the curves given by Lukes is shown in Figure 2. Some disagreement is noticed for frequencies higher than 150 GHz, the error becoming appreciable for wavelengths shorter than 1 mm. This is not surprising since the absorption in this region is due to a different mechanism than that in the microwave range. It is usually admitted that the high-frequency absorption is a resonant type of absorption due to the intramolecular modes of the liquid lattice for which Debye's theory no longer applies. The formulas of resonant absorption for water have been derived by Saxton (1952), based on a theory for resonance absorption in polar media by Fröhlich (1949). This theory shows a peak in the absorption at a wavelength near 70 μm and

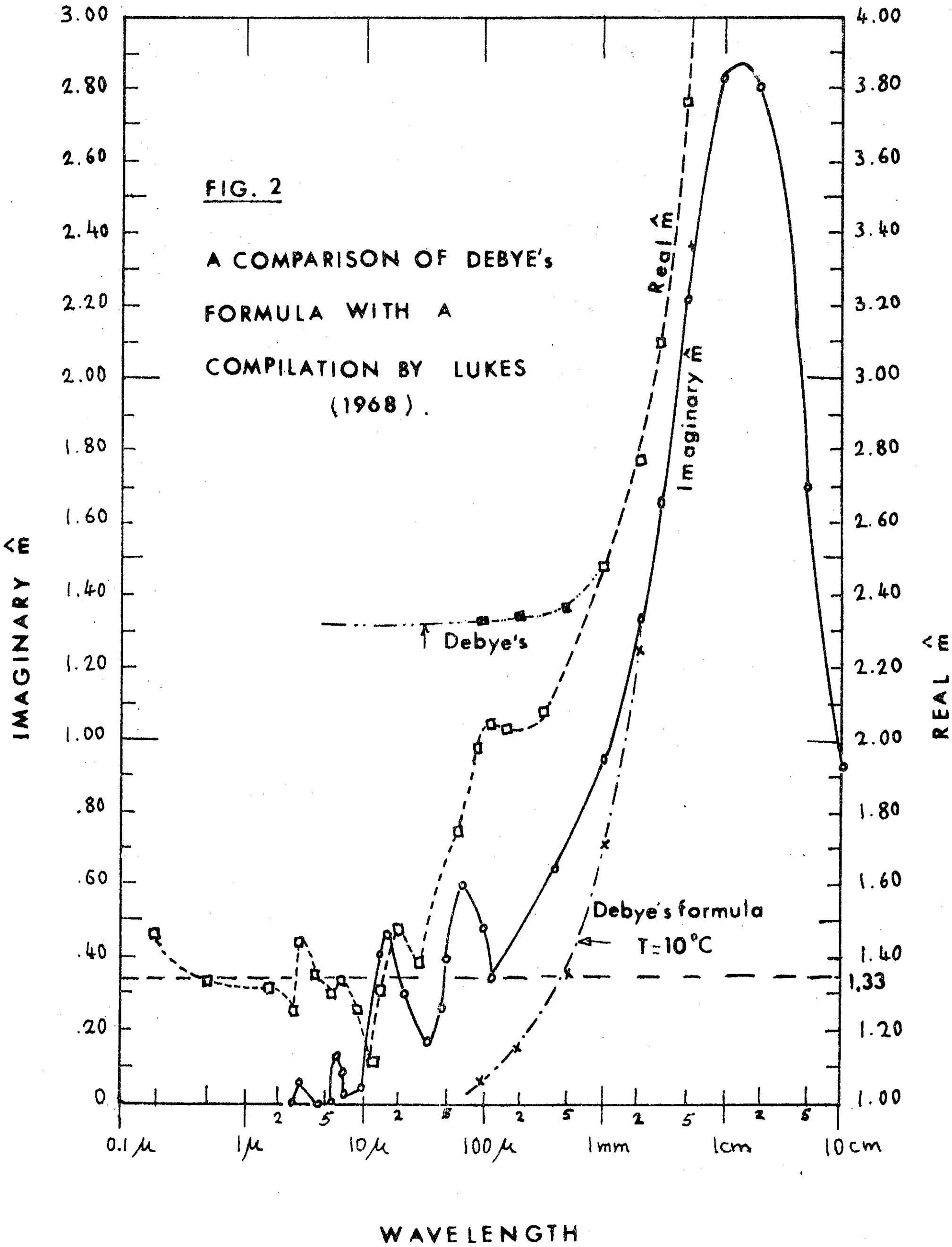

FIG. 2
A COMPARISON OF DEBYE's FORMULA WITH A COMPILATION BY LUKES (1968).
IMAGINARY <E
REAL <E
Real <E
Imaginary <E
Debye's
Debye's formula
T=10°C
1,33
0.1 μ
1 μ
10 μ
100 μ
1mm
1cm
10cm
WAVELENGTH

is in good agreement with measurements.

2.5. Conclusion

The absorption and dispersion of liquid water in the radio-frequency and far infrared regions can be divided into two parts. The first, occurring at wavelengths greater than 1 mm, can be associated with non-resonant, viscously damped, reorientation of the water molecule dipole and is accounted for by Debye's theory; the second, occurring at wavelengths less than 1 mm, is attributed to resonant absorption by the intramolecular modes of the liquid lattice. The two phenomena overlap near 1 mm.

A good fit to the microwave and submillimeter experimental data cannot be obtained with a Debye function. However, for practical reasons, and because of the weak influence of refractive index variations on the rain scattering parameters, a Debye formula has been used in this study over the range 10 cm to 0.5 mm. A critical attitude is recommended for results obtained at 600 GHz.

Next, we consider the fundamental electromagnetic problem of diffraction of a plane wave by an imperfectly conducting sphere, for which treatment the complex refractive index derived in this chapter will be used.

CHAPTER 3

SCATTERING OF A PLANE ELECTROMAGNETIC WAVE BY A SINGLE SPHERICAL WATER DROP

3.1. Introduction

This chapter is a treatment of the scattering of a plane electromagnetic wave by a water drop, according to Mie's approach (1908). A quick review of the theory points out the most useful equations. Computations of the forward scattering function in the cm and mm wavelength range, for drop sizes usually encountered in rain showers, are presented. The relative roles of scattering and absorption in the total extinction process have also been investigated, since they are of interest to radar meteorologists. A study of temperature sensitivity is also presented followed by a summary of the influence of non-sphericity of the drops, as derived by Oguchi (1960). Finally, a computer program written to evaluate Mie's series is described in Appendix 2, and some results obtained for the cross-sections of water drops in the cm and mm range are presented in Appendix 3.

A widely used model for studying the effects of rain on microwave propagation treats raindrops as homogeneous spheres having a complex dielectric constant. Although the shape of falling raindrops as observed by means of a raindrop camera (such as the one developed by Jones (1959)), exhibits, at least for large drops, a marked flattening on its lower surface and a smoothly rounded curvature on its upper surface, the spherical shape can be treated with reasonable mathematical complexity and is the only one that will be considered in this study.

The general solution to the problem of diffraction of a plane electromagnetic wave by a lossy dielectric sphere was given by Mie (1908) in the form of an infinite series expansion. Some other excellent treatments of this problem are found in Stratton (1941), Kerr (1951), van de Hulst (1957) and Kerker (1969). Some of the results are briefly reviewed in the next section.

3.2. A summary of the far-field solution

Consider, as in Figure 3, a linearly polarized plane wave (E_x, H_y), propagating along the z-axis of a cartesian coordinate system such that

$$\bar{E}^i = \hat{E}^i \, \bar{e}_x = E^i \exp(-jk_o z + jwt)\bar{e}_x \tag{3.1}$$

$$\bar{H}^i = \hat{H}^i \, \bar{e}_y = H^i \exp(-jk_o z + jwt)\bar{e}_y \tag{3.2}$$

where $k_o = \dfrac{2\pi}{\lambda_o} = \dfrac{\omega}{c}$ and is the free space wavenumber (3.3)

and $\bar{e}_x$, $\bar{e}_y$ are unit vectors in the x,y direction respectively.

A spherical water drop of diameter D is located at the center of the cartesian coordinate system. The solution for the scattered far-field (E-field has been chosen) may be written in a matrix notation as

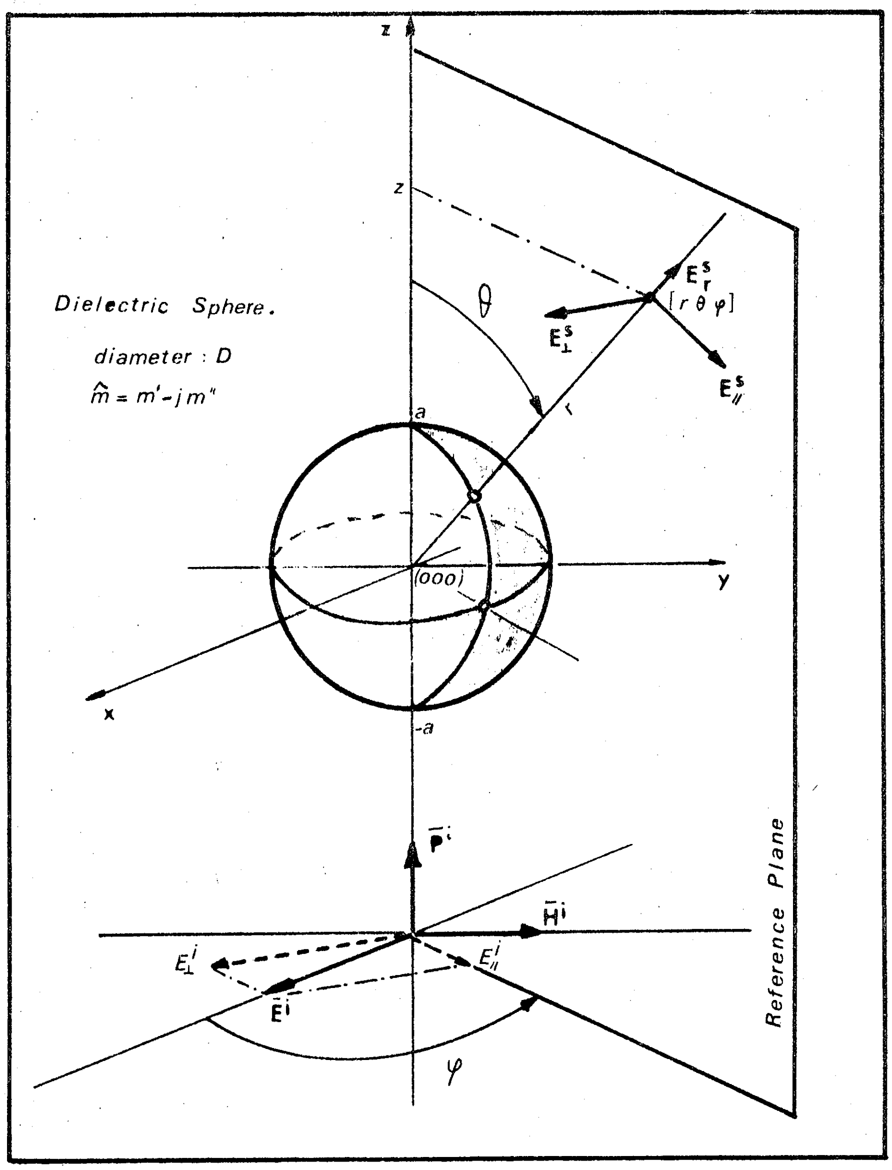

FIG. 3

GEOMETRY USED IN STUDYING THE SCATTERING OF A PLANE WAVE BY A SPHERE

$$\begin{pmatrix} \hat{E}_{\perp}^{s} \\ \hat{E}_{\parallel}^{s} \end{pmatrix} = \underbrace{\begin{pmatrix} \hat{S}_1(\hat{m},D,\theta) & 0 \\ 0 & \hat{S}_2(\hat{m},D,\theta) \end{pmatrix}}_{\substack{\text{scattering matrix} \\ (S)}} \begin{pmatrix} E_{\perp}^{i} \\ E_{\parallel}^{i} \end{pmatrix} \cdot \frac{e^{-jK_o r + jwt}}{jK_o r} \qquad (3.4)$$

where $\hat{E}_{\perp}^{s}$ $(\hat{E}_{\parallel}^{s})$ is the component of the scattered far-field perpendicular (parallel) to a reference plane, chosen as the one containing the z-axis and the observation point (r,θ,φ).

The coefficients of the scattering matrix (S) are given by:

$$\hat{S}_1(\hat{m},D,\theta) = \sum_{n=1}^{\infty} \frac{(2n+1)}{n(n+1)} \left[\hat{a}_n \Pi_n(\cos\theta) + \hat{b}_n \tau_n(\cos\theta) \right] \qquad (3.5)$$

$$\hat{S}_2(\hat{m},D,\theta) = \sum_{n=1}^{\infty} \frac{(2n+1)}{n(n+1)} \left[\hat{b}_n \Pi_n(\cos\theta) + \hat{a}_n \tau_n(\cos\theta) \right] \qquad (3.6)$$

where

$$\Pi_n(\cos\theta) = \frac{1}{\sin\theta} \; P_n^1(\cos\theta) \qquad (3.7)$$

$$\tau_n(\cos\theta) = \frac{d}{d\theta} (P_n^1(\cos\theta) \qquad (3.8)$$

The P_n^1 are the first order associated Legendre Polynomials, and $\hat{m}(\lambda,T)$ is the complex refractive index of the drop as studied in Chapter 2. The Mie scattering coefficients $\hat{a}_n$ and $\hat{b}_n$ are expressed in terms of spherical Bessel and Hankel functions as follows:

$$\hat{a}_n(\hat{m},D,z) = \frac{j_n(z)\,[\hat{m}z\ j_n(\hat{m}z)]' - \hat{m}^2 j_n(\hat{m}z)\,[z\ j_n(z)]'}{h_n^{(2)}(z)\,[\hat{m}z\ j_n(\hat{m}z)]' - \hat{m}^2\ j_n(\hat{m}z)\,[zh_n^{(2)}(z)]'} \tag{3.9}$$

$$\hat{b}_n(m,D,z) = \frac{j_n(z)\,[\hat{m}z\ j_n(\hat{m}z)]' - j_n(\hat{m}z)\,[z\ j_n(z)]'}{h_n^{(2)}(z)\,[\hat{m}z\ j_n(\hat{m}z)]' - j_n(\hat{m}z)\,[z\ h_n^{(2)}(z)]'} \tag{3.10}$$

where $$z = \frac{\pi D}{\lambda_o} = k_o a \quad \left[a = D/2\right] \tag{3.11}$$

$$\hat{m} = m' - jm''$$

$j_n(z)$ and $h_n^{(2)}(z)$ are the spherical Bessel and Hankel functions in Sommerfeld's notation:

$$j_n(z) = \sqrt{\frac{\pi}{2z}} \cdot J_{n+\frac{1}{2}}(z) \tag{3.12}$$

$$h_n^{(2)}(z) = j_n(z) - jy_n(z) \tag{3.13}$$

The prime denotes derivative with respect to the argument. The total far-field is expressed by:

$$\bar{E}^t = \bar{E}^i + \bar{E}^s \tag{3.14}$$

$$\begin{pmatrix} \hat{E}^t_\perp \\ \hat{E}^t_\parallel \end{pmatrix} = \begin{pmatrix} \hat{E}^i_\perp \\ \hat{E}^i_\parallel \end{pmatrix} + \begin{pmatrix} \hat{S}_1 & 0 \\ 0 & \hat{S}_2 \end{pmatrix} \begin{pmatrix} \hat{E}^i \\ \hat{E}^i \end{pmatrix} \frac{\exp(-jk_o \cdot (r-z))}{jk_o r} \tag{3.15}$$

The $\bar{E}$ and $\bar{H}$ fields are related by:

$$H^t_\perp = \frac{E^t_\parallel}{\eta_o} \quad \text{and} \quad H^t_\parallel = -\frac{E^t_\perp}{\eta_o} \tag{3.16}$$

where $\eta_o = \sqrt{\frac{\mu_o}{\varepsilon_o}} \sim 120\pi$, is the free space impedance.

The resulting far-field is thus an outgoing spherical wave. However, the amplitude of the field varies significantly with θ. In the near-field, there is a radial component $\bar{E}_r$, but its amplitude decreases with r faster than 1/r, so that it has been neglected in (3.4) and (3.15).

3.3. Forward direction ($\theta=0$).

In the forward direction, the above expressions simplify considerably. In that case, since

$$\Pi_n(1) = \tau_n(1) = n(n+1)/2 \tag{3.16}$$

we get

$$\hat{S}_1(\hat{m},D,0) = \hat{S}_2(\hat{m},D,0) = \hat{S}_o(\lambda,D) \tag{3.17}$$

$$\hat{S}_o(\lambda,D) = \sum_{n=1}^{\infty} \tfrac{1}{2}(2n+1)(\hat{a}_n + \hat{b}_n) \tag{3.18}$$

This function, called the forward-scattering function, is complex and thus carries both amplitude and phase information. We may write it in the form

$$\hat{S}_o(\lambda,D) = s(0).\exp(j\sigma(0)) \tag{3.19}$$

It is also a function of temperature through the complex refractive index of water, $\hat{m}$.

Thus, in the forward direction, the wave is transmitted without change in polarization; the scattering matrix reduces to a single term and the total far-field may be written as

$$\hat{E}_o^{\,t} = \hat{E}^i \left(1 + \frac{\hat{S}_o(\lambda, D)}{jk_o r}\right) \qquad (3.20)$$

This result implies that the intensity of the field in the forward direction is independent of the position of the scattering particle and is only a function of λ, D, and T.

3.4. Cross-sections

Very often one is interested in finding how much power has been extracted from the incident beam due to the presence of the drop. The mechanism by which power loss occurs is twofold:

a. Due to the presence of an imaginary term in the expression for the refractive index, some power is absorbed inside the drop and dissipated into heat.

b. Some power is simply scattered out of the beam by a diffraction mechanism.

The importance with which each mechanism contributes to the total attenuation may be characterized by a single-drop albedo coefficient (see below). In the following, we shall refer to extinction as the total power loss by either mechanism.

Extinction = absorption + scattering.

This total loss can be characterized by means of an extinction cross-section, defined as:

$$C_{ext} = \frac{\text{total power loss}}{\text{incident power density}} = \frac{P_{loss}}{|\hat{E}^i|^2/2\eta_o} \quad (3.21)$$

The total energy loss may thus be viewed as the amount of energy of the incident plane wave that is intercepted by an area C_{ext}.

The value of this area can be found by integrating the Poynting vector over an infinitely large sphere containing the drop. It is found to be

$$C_{ext} = \frac{\lambda_o^2}{2\pi} \operatorname{Re} \sum_{n=1}^{\infty} (2n+1)(\hat{a}_n + \hat{b}_n) = \frac{4\pi}{k_o^2} \operatorname{Re}\left[\hat{S}_o(\lambda, D)\right] \quad (3.22)$$

In the same manner, we can define a <u>scattering cross-section</u> as

$$C_{scat} = \frac{\text{total scattered power}}{\text{incident power density}}$$

and find

$$C_{scat} = \frac{\lambda_o^2}{2\pi} \sum_{n=1}^{\infty} (2n+1)(|a_n|^2 + |b_n|^2) \quad (3.23)$$

Also

$$C_{abs} = C_{ext} - C_{scat} \quad (3.24)$$

3.5. Efficiency factors

Normalizing the cross-sections by the geometrical cross-section of the drop $G = \pi D^2/4$, we get the <u>efficiency factors</u>. Those are so called, because they are a measure of how efficiently a drop extracts energy from the beam. We get:

$$Q_{ext} = \frac{C_{ext}}{G} = \frac{4}{z^2} \cdot \operatorname{Re}\left[\hat{S}_o(\lambda, D)\right] \quad (3.25)$$

$$Q_{scat} = \frac{C_{scat}}{G} \quad \text{and } Q_{abs} = \frac{C_{abs}}{G} \tag{3.26}$$

If we define

$$Q_{im} = \frac{4}{z^2} \text{ Im} \left[\hat{S}_o(\lambda, D)\right] \tag{3.27}$$

we get a relationship between those efficiency factors and the forward-scattering function of the form

$$\frac{\hat{S}_o(\lambda, D)}{z^2} = \tfrac{1}{4} (Q_{ext} + jQ_{im}) \tag{3.28}$$

where

$$z = k_o a = \frac{\pi D}{\lambda_o} \tag{3.29}$$

The forward and backscattering efficiency factors may also be obtained and are of the form

$$S_{forw} = \lim_{R\to\infty} \frac{4\pi R^2}{\pi a^2} \left| \frac{E^s}{E^i} \frac{(\theta=0)}{} \right|^2 = \frac{4}{z^2} \left| \hat{S}_o(\lambda, D) \right|^2 \tag{3.30}$$

$$S_{back} = \lim_{R\to\infty} \frac{4\pi R^2}{\pi a^2} \left| \frac{E^s}{E^i} \frac{(\theta=\pi)}{} \right|^2 = \frac{1}{z^2} \left| \sum_{n=1}^{\infty} (-1)^n (2n+1)(\hat{a}_n - \hat{b}_n) \right|^2$$

$$= \frac{4}{z^2} \left| (\hat{S}_\pi(\lambda, D) \right|^2 \tag{3.31}$$

These factors are related to the energy density present in the forward or in the backward direction respectively.

3.6. Rayleigh approximation

Rayleigh scattering is a limiting case of the above theory, when the drop is small compared to the incident radiation wavelength ($z = k_o a \ll 1$ and $|\hat{m}z| < 1$). Expanding

Mie's series in power of z and neglecting terms of order higher than 6, it can be shown that the above formulas reduce to the one derived by Rayleigh (1881):

$$\hat{S}_o^R(\lambda,D) = \underbrace{j\ \hat{K}\ z^3}_{\text{absorption}} + \underbrace{\frac{2}{3}\ |\hat{K}|^2\ z^6}_{\text{scattering}} + \mathcal{O}(z^9) \tag{3.32}$$

where

$$\hat{K} = \frac{\hat{m}^2 - 1}{\hat{m}^2 + 2} \tag{3.33}$$

From (3.32) we obtain:

$$C^R_{scat} = \frac{2}{3}\frac{\pi^2}{\lambda_o^4}\ |\hat{K}|^2\ D^6 \tag{3.34}$$

$$C^R_{abs} = \frac{\pi^2}{\lambda_o}\ \mathrm{Im}(-\hat{K})\ D^3 \tag{3.35}$$

$$C^R_{ext} = C^R_{abs} + C^R_{scat} \tag{3.36}$$

$$S^R_{back} = \frac{3}{2}\ C^R_{scat} = S^R_{forw} \tag{3.37}$$

Since Rayleigh scattering is proportional to z^6 and the absorption to z^3, in practical calculations involving water drops, scattering effects may be neglected when $z < 0.01$. The term "Rayleigh approximation" is often used when scattering is negligible compared to absorption and the extinction is proportional to the volume of water in the path. It has been found experimentally by Crane (1966) that this condition holds for frequencies below 2 GHz when calculating atten uation, and up to 10 GHz when

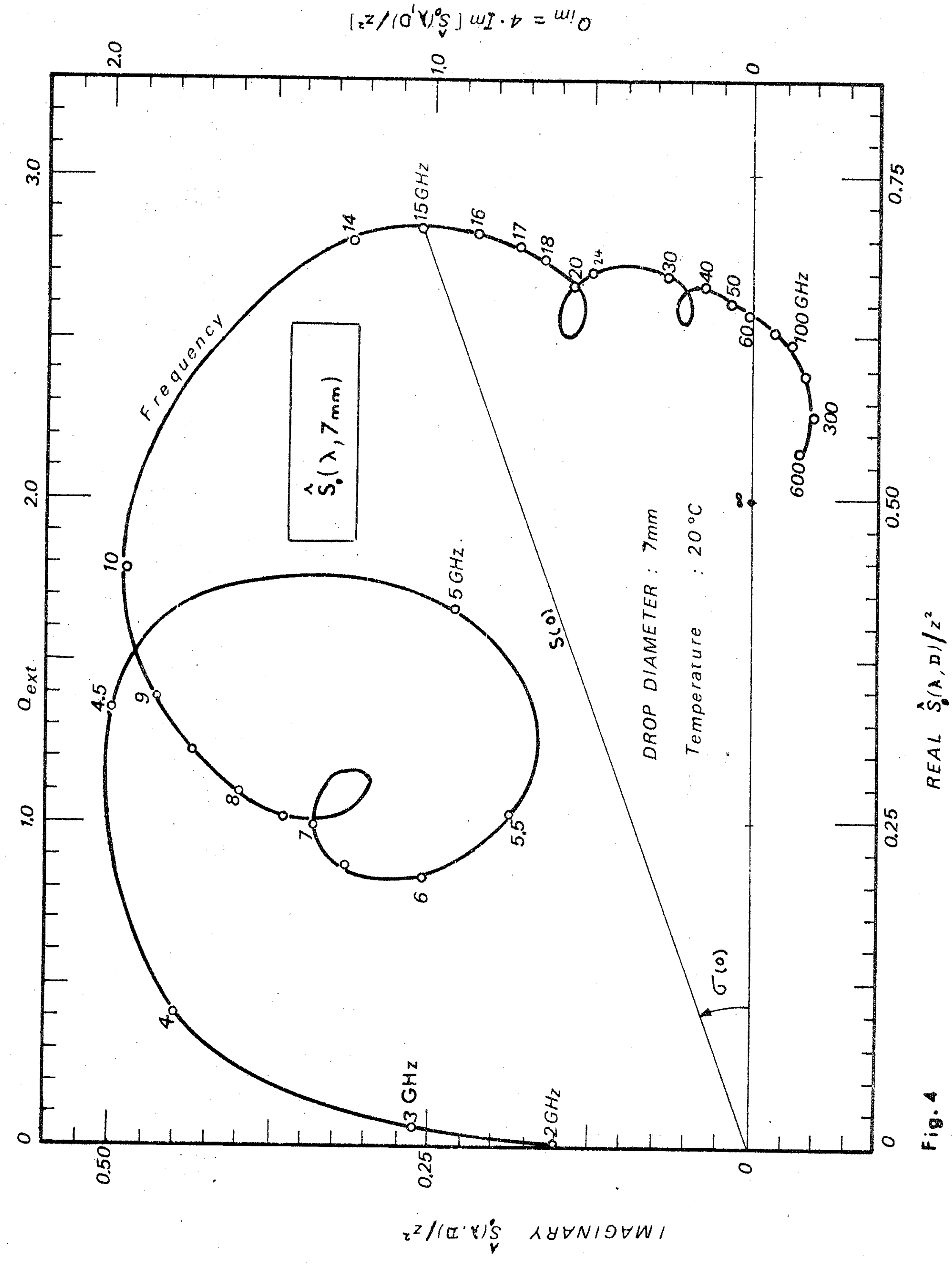
$a_{im} = 4 \cdot Im[\hat{S}_0(\lambda, D)/z^2]$
a_{ext}
IMAGINARY $\hat{S}_0(\lambda, D)/z^2$
REAL $\hat{S}_0(\lambda, D)/z^2$
$\hat{S}_0(\lambda, 7_{mm})$
Frequency
DROP DIAMETER : 7mm
Temperature : 20 °C
S(0)
σ(0)
2 GHz
3 GHz
5 GHz
15 GHz
100 GHz
∞

Fig. 4

calculating reflectivity.

3.7. Numerical Computations

In actual use, the Mie theory is somewhat cumbersome because it requires summing of a slowly convergent infinite series. This is especially true for large values of the argument, such as the one that occur in the upper mm range.

To avoid this difficulty, investigators in the past have tried to use approximations (the Rayleigh approximation has often been extrapolated too far), or have looked into limiting cases (perfectly conducting spheres).

The availability of high speed digital computers has somewhat changed this situation, but the computer time still remains excessively high, if one tries to calculate the spherical Bessel and Hankel functions of complex argument and their derivatives (3.9 and 3.10) by their series expansions.

The introduction of logarithmic derivatives by Aden (1951), reduces the evaluation to a recurrence formula, thus considerably diminishing the time required to compute the functions. A fortran subroutine, named ADEN, based on this method, has been written by the author and is presented in some detail in Appendix 2. The results obtained from this program for a single water-drop are presented next.

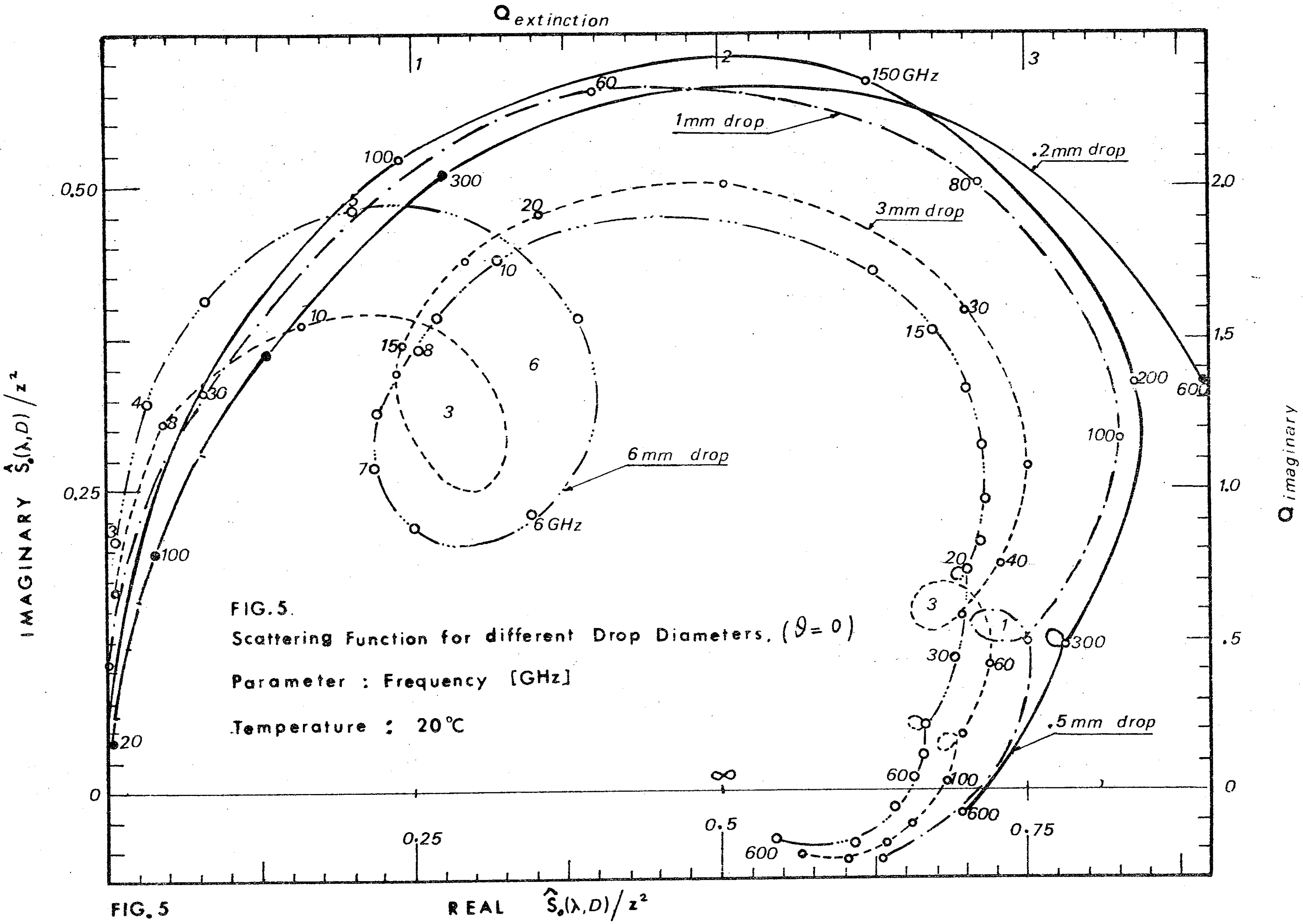

FIG. 5.
Scattering Function for different Drop Diameters, ($\vartheta = 0$)
Parameter : Frequency [GHz]
Temperature : 20°C

FIG. 5

3.8. Forward scattering function: $\hat{S}_o(\lambda,D)$

A normalized form of the forward scattering function is plotted in the complex plane in Figures 4 and 5. The different curves correspond to various drop diameters and the parameter on the curves is frequency, expressed in GHz. Cartesian plots of the real and imaginary parts of the same function can be found in Appendix 3, displayed versus frequency and drop diameter.

Regarding $\hat{S}_o(\lambda,D)$, the following comments can be formulated:

a. $\hat{S}_o(\lambda,D)/z^2$ is contained inside a circle of unit diameter, centered at (0.5, 0).

b. Some resonances, especially pronounced in the case of large drops for frequencies below 15 GHz, appear on the curves; they are severely damped when they occur in a region where the absorption is high (λ<1 cm).

c. The real part (extinction) has a maximum occuring at a frequency approximately equal to $\frac{100}{D\,(\mathrm{mm})}$ GHz; the value of the peak increases with decreasing drop diameters.

d. The imaginary part has a sharper maximum than the real part and occurs slightly before that of the latter.

e. In general, a drop has significant influence only for $D \gtrsim 0.1\lambda$.

f. When $D/\lambda \to \infty$, $\hat{S}_o(\lambda,D)$ becomes purely real and Q_{ext} approaches the value of 2, which means that C_{ext} is twice the geometrical cross-section. This "extinction paradox" has been investigated, among others, by van de Hulst (1957) (page 107) and by Kerker (1969) (page 106). It can only be explained by the laws of physical optics and is a consequence of Babinet's principle.

g. It is worthwhile pointing out that the imaginary part becomes negative, for a frequency that is dependent on the drop diameter:

D (mm)	7	6	5	4	3	2	1	.5
f_c (GHz)	64	72	80	92	120	146	280	500

(3.38)

This fact will have some consequences later on.

h. The fact that the maxima of the cross-sections occur at different frequencies for each drop diameter may be useful in determing the drop-size distribution from multiple-frequency propagation measurements.

3.9. Single-drop scattering albedo

Next, we examine the relative part of scattering and absorption in the total extinction process. Such a distinction is important, because a simplified formula for evaluating attenuation from radiometric measurements neglect scattering (e.g. see Fañin (1971).

The ratio of scattering energy to the total energy loss is called single-drop scattering albedo

$$A(\lambda,D) = \frac{Q_{scat}}{Q_{ext}} \tag{3.39}$$

FIG. 6

SINGLE-DROP SCATTERING ALBEDO COEFFICIENT

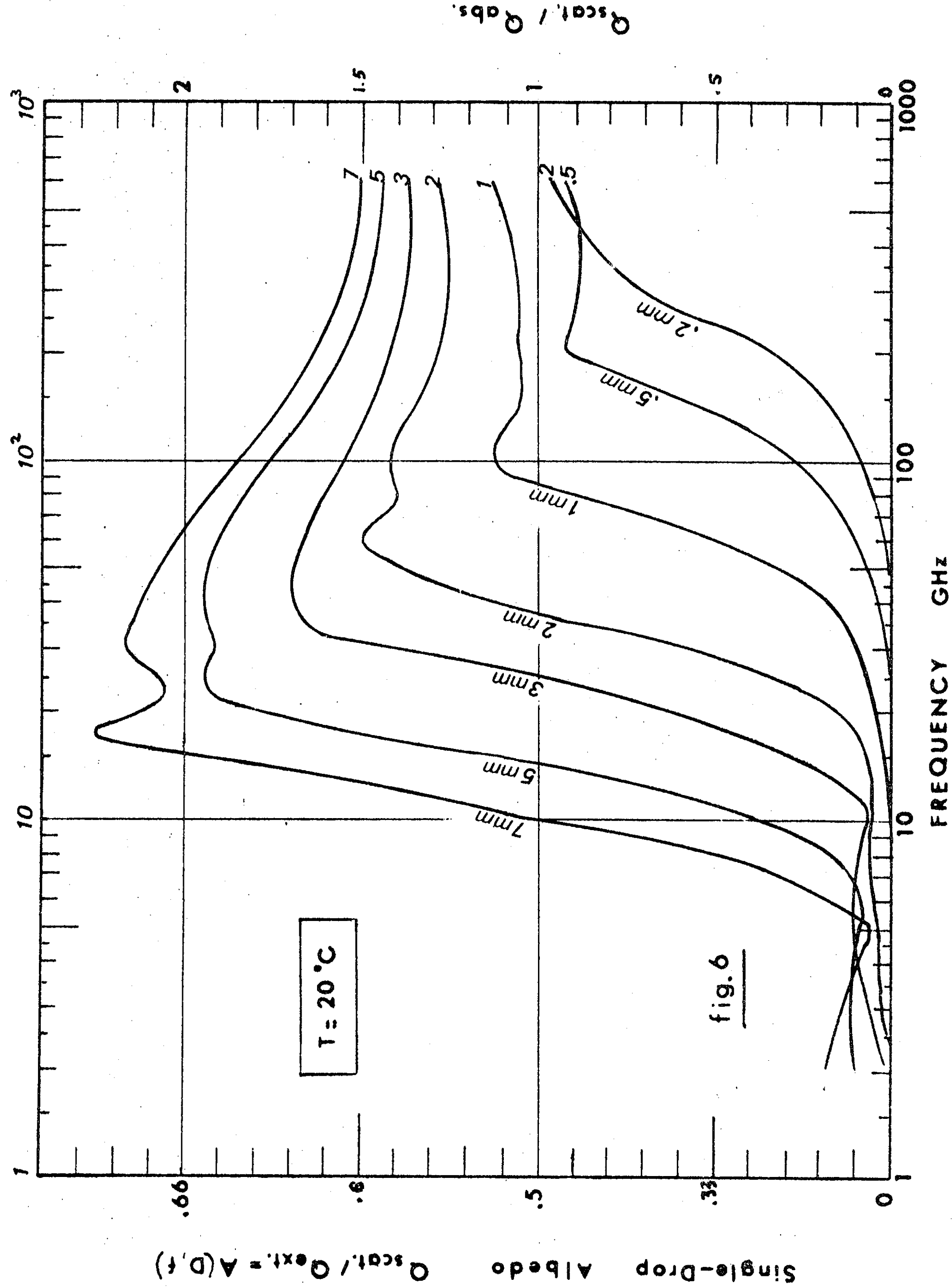

This function is plotted in Figure 6 versus frequency, for a temperature of 20 °C. (Actually, the ratio $Q_{scat}/Q_{abs} = A/(1-A)$ has been plotted, so that the A scale is not linear !). The quantity (1-A) is the percentage of energy that is absorbed.

As can be seen from this plot, a drop starts scattering energy only when $\lambda \approx 10D$; the scattering effect is maximum for $\lambda \approx D$ (Mie region); for rain drops, (1 mm < diam < 7 mm), this maximum occurs in the EHF band. At higher frequencies, the albedo has a tendency to stabilize around 0.5, which means that there is as much energy scattered as there is absorbed. The limit as D/λ becomes very large is one, since the absorption is negligible in the visible region.

3.10. Temperature dependence

All the results obtained until now have been for a temperature of 20 °C. Since the refractive index is very strongly temperature dependent, the forward scattering function must depend on temperature also.

Figures 7 to 9 illustrate this dependence for Q_{ext}; the temperature of 20 °C has been chosen as the reference and the correction factor is multiplicative.

Figure 7 shows that large drops are very sensitive to temperature in the region below 10 GHz; for small drops the influence of temperature can extend up to 100 GHz. This condition accounts for the strong temperature

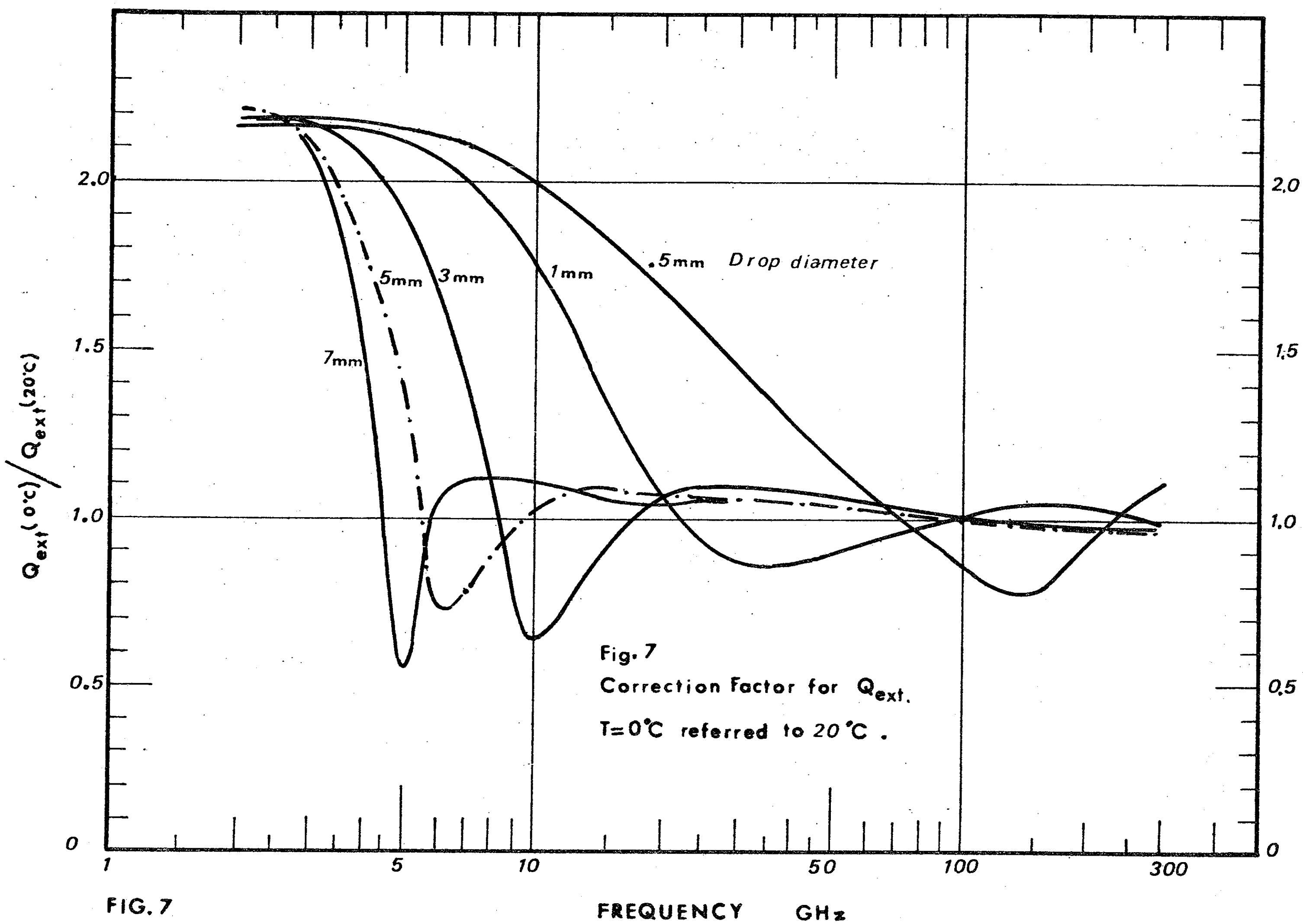

$Q_{ext}(0°C) / Q_{ext}(20°C)$
2.0
1.5
1.0
0.5
0
.5mm Drop diameter
1mm
3mm
5mm
7mm
Fig. 7
Correction Factor for $Q_{ext.}$
T=0°C referred to 20°C .
1
5
10
50
100
300
FREQUENCY GHz

FIG. 7

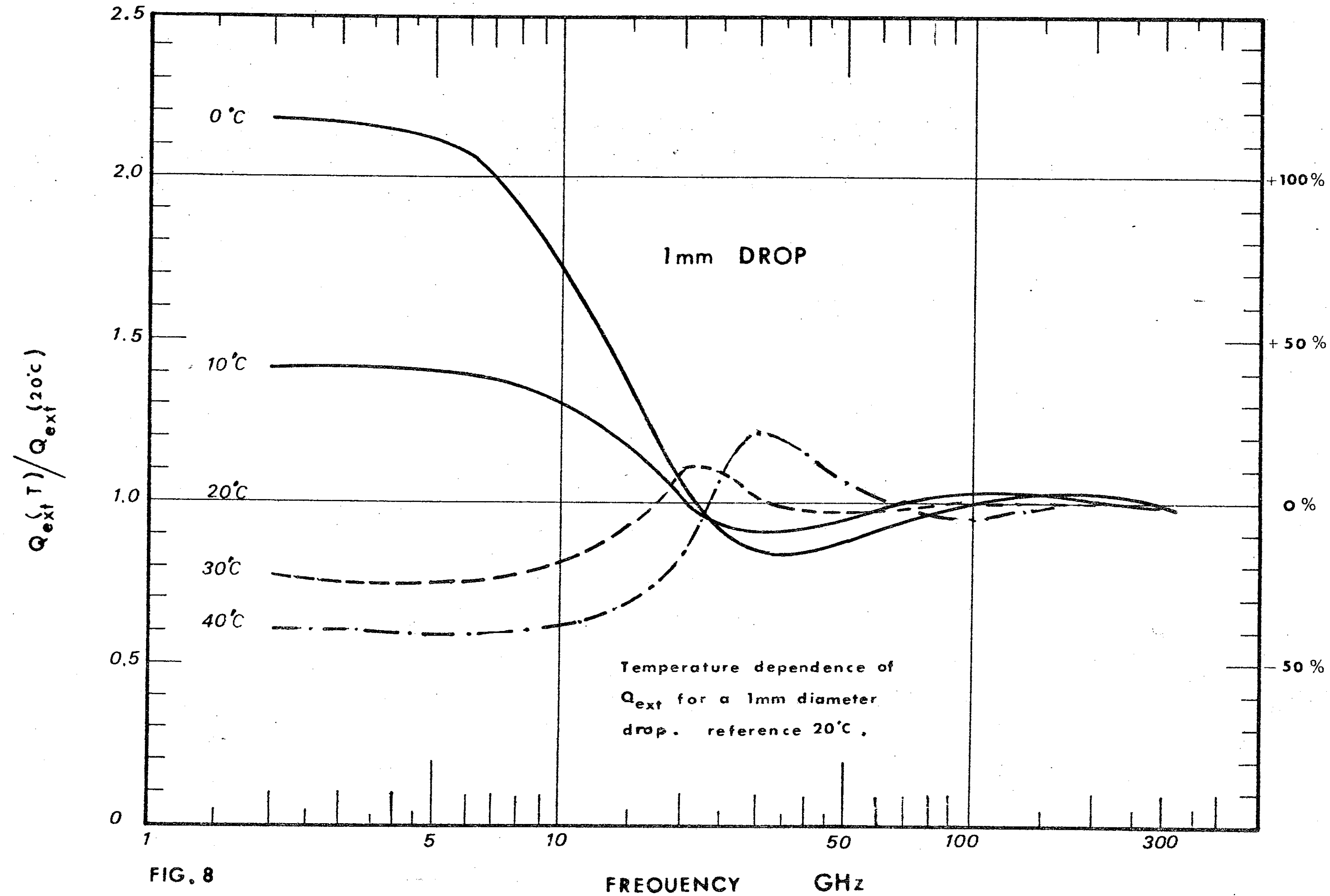

1mm DROP
0 °C
10 °C
20 °C
30 °C
40 °C
2.5
2.0
1.5
1.0
0.5
0
+100 %
+ 50 %
0 %
− 50 %
1
5
10
50
100
300
$Q_{ext}(T) / Q_{ext}(20°C)$
FREQUENCY GHz
Temperature dependence of
Q_{ext} for a 1mm diameter
drop. reference 20°C.

FIG. 8

dependence of the attenuation observed in fog and the somewhat less important effect observed in rain.

Figure 8 shows the relative effect of different temperatures for a single drop diameter (1 mm). The effects due to a decrease in temperature are larger than those for an increase by the same amount. The frequency range over which the influence extends is approximately the same for all temperatures.

An attempt to plot the 3 dimensional surface $Q_{ext}(0°C)/Q_{ext}(20\ °C)$ as a function of λ and D has been made in Figure 9. The graph shows a narrow valley (-50%) in the region $\lambda \approx 10D$ and a maximum sensitivity for small drops and large wavelengths.

The temperature dependence for the <u>imaginary part</u> of the same function has also been investigated. For frequencies below 30 GHz (where the large resonances occur) it showed a similar behavior to that of the real part; however, the error was always within 50% whereas for the real part the correction exceeded 100%. But, unlike the real part dependence, some very strong effects occur for frequencies where the imaginary part is changing sign (see sect. 3.8). This fact seems to be due to the strong frequency gradient of the function near this point. A small shift of the curve, due to a temperature change, alters the relative value drastically.

3.11. Non-sphericity of the drop

A falling raindrop has more nearly the form of an

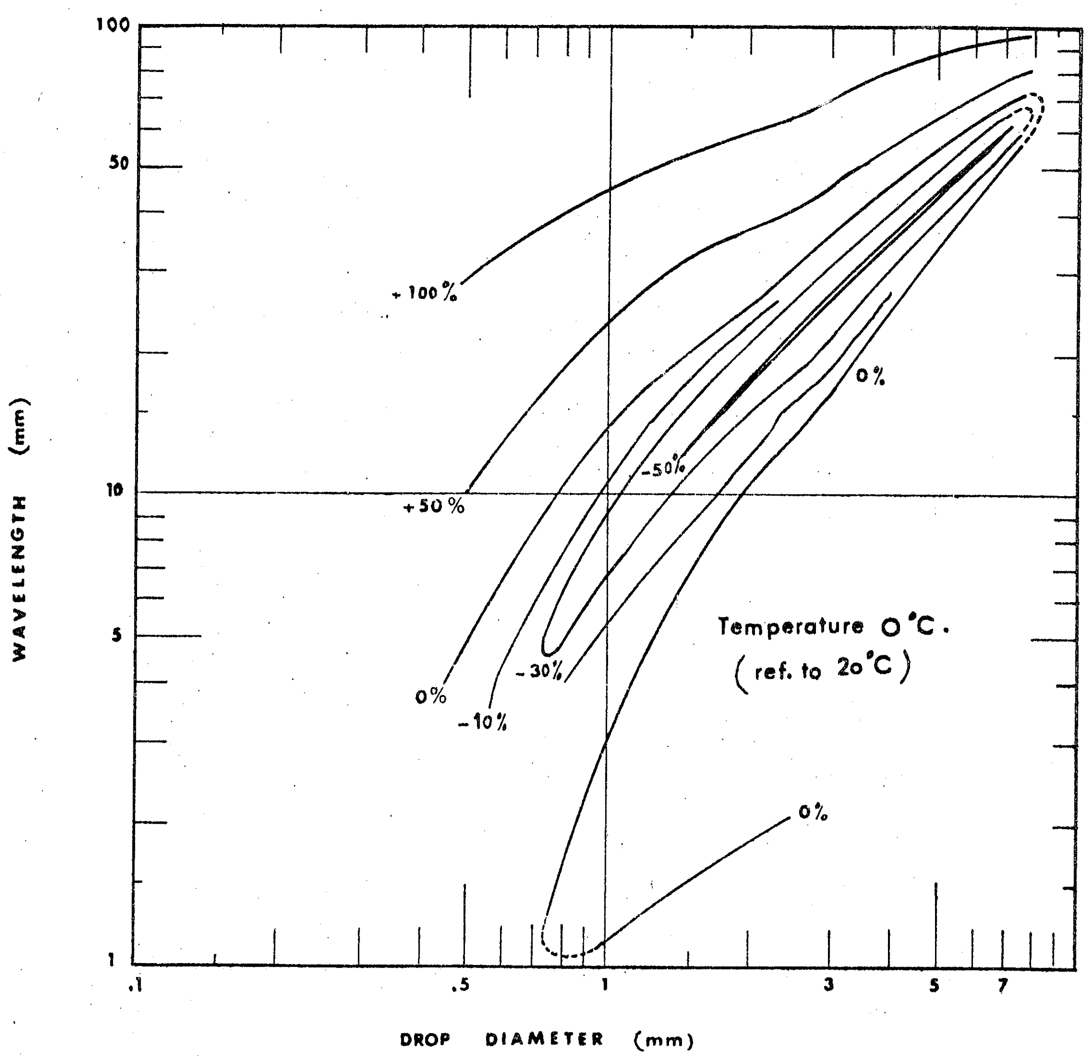

FIG. 9

THE RATIO OF THE EXTINCTION CROSS-SECTION AT 0°C TO THE ONE AT 20°C (PERCENT VARIATION) oblate spheroid than a sphere. Assuming that the eccentricity is small, spheroids can be treated by considering perturbations from the spherical form. The theory has been developed by Oguchi (1960, 1964).

The forward scattering functions are no longer independent of the polarization of the incident wave, as shown by the relations

$$\hat{S}_1(\lambda,D) = \hat{S}_o(\lambda,D) + \nu\hat{S}_\perp(\lambda,D) \tag{3.40}$$

$$\hat{S}_2(\lambda,D) = \hat{S}_o(\lambda,D) + \nu\hat{S}_\parallel(\lambda,D) \tag{3.41}$$

where $\nu = 1 - \frac{a^2}{b^2}$,

a is the minor axis,

b is the major axis,

$\hat{S}_o(\lambda,D)$ is the forward-scattering function for a sphere,

and $\hat{S}_\perp(\lambda,D)$, $\hat{S}_\parallel(\lambda,D)$ are complicated expressions to be found in Oguchi's paper.

The efficiency factors are larger for horizontal polarization than for vertical polarization. When the incidence is not normal ($\theta \neq 0$), some cross-terms appear in the scattering matrix, giving rise to cross-polarization interference. This effect has been studied by Saunders (1971) and also by Thomas (1971).

3.12. Conclusion

In this chapter, the forward scattering function for a water sphere has been analyzed. Although such phenomena as higher attenuation observed for horizontal than for vertical polarization, cross-polarization effects, cannot be explained by means of a spherical-drop model, no attempt has been made to systematically analyze the oblate spheroid model; non-sphericity effects can always be considered as perturbations from the spherical drop model and be accounted for by means of a correction factor. Tabulations of those corrections factors exist for a limited number of frequencies; they can always be obtained, when needed, from Oguchi's formulas.

A complete study of the diffraction problem would include the angular dependence of the scattering function; this is needed, for instance, when studying the interference between two radio-links due to coupling by energy scattered by rain. However, the angular dependence is not very sharp around zero degrees and for our purpose $\hat{S}_o(\lambda,D)$ will be considered as a sufficient approximation for angles up to 10 degrees on each side of the normal. This does not imply, however, that scattering from a spherical drop is isotropic. Rain drops are strongly <u>anisotropic scatterers</u> and the ratio of forward to backward scattering cross-section, which is frequency dependent, can reach values as high as 10^3 at 300 GHz.

We are ready now to consider the effect of an ensemble of drops and to try to model propagation in rain.

CHAPTER 4

ELECTROMAGNETIC PROPAGATION THROUGH RAIN

4.1. Introduction

As shown in the previous chapter, rain drops both absorb and scatter electromagnetic energy in the centimeter and millimeter wavelength range. The equations governing electromagnetic propagation through rain are thus those of radiative transfer theory (Crane 1971). The intensity of the radiation at a given point inside the medium can be viewed as made up from two components, an unscattered (coherent) wave that has been attenuated by absorption and scattering and a diffuse (incoherent) wave that results from scattering and thermal emission by the drops. In the case of one-dimensional propagation through an isotropic medium ,the differential equation takes the simple form

$$dI(s') = \underbrace{-\, I(s')\beta(s')\, ds'}_{\text{coherent}} + \underbrace{S[I(s')]\, ds'}_{\text{incoherent}} \qquad (4.1)$$

where $\beta(s')$ is the extinction coefficient per unit volume (cm^{-1})

$S[I(s')]$ is the incoherent source term due to scattering and thermal emission

A first-order approximation of the integral equation may be obtained by replacing the incoherent source term

$S[I(s')]$ by $\varepsilon(s)\cdot I'(s')$ where $I'(s')$ is the solution of (4.1) obtained for the coherent source only. By integration we obtain the intensity, after propagating a distance s

$$I(s) = I_o \exp\left(-\int_o^s \beta(s')ds'\right) + I_o \int_o^s \varepsilon(s') \exp\left(-\int_o^s \beta(s'')ds''\right) ds' \qquad (4.2)$$

where I_o is the incident intensity (W/m^2)

and $\varepsilon(s')$ describes the scattering- and thermal emission process inside the medium.

The first term characterizes the behavior of the coherent wave, whereas the second term gives the intensity of the diffuse, incoherent component inside the medium. If we neglect thermal emission, the incoherent radiation is only due to scattering. The scattering properties of the medium may be described by means of a single-scattering albedo coefficient, which is an indication of the fraction of the total energy loss per unit volume that is due to scattering. This coefficient has been calculated for different rain intensities, assuming homogeneous rain with a Laws and Parsons (1943) drop-size distribution, (see section 4.4). Figure 10 shows this coefficient versus frequency and clearly indicates that at millimeter wavelengths rain cannot be considered as a purely absorbing medium.

In general scattering is anisotropic and an angular dependence has to be introduced in (4.2). A recent

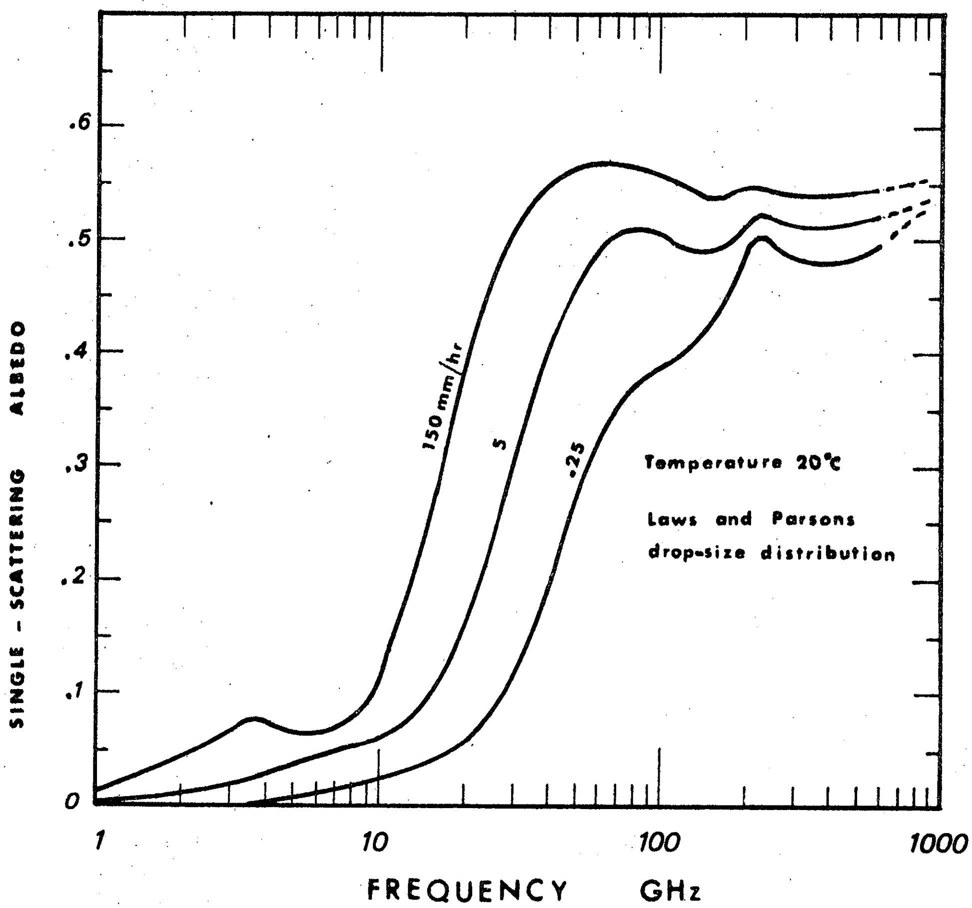

FIG. 10

VOLUME SINGLE-SCATTERING ALBEDO COEFFICIENT
FOR SELECTED RAINFALL RATES

survey of the approximate solutions that have been obtained for the general radiative transfer problem, including the secondary source term, can be found in a paper by Lerner and Holland (1970). Another approach, which leads to the same kind of mathematical complexity, considers randomly distributed discrete scatterers (Twersky 1962). This approach looks into the microscopic detail of the scattering process, whereas the radiative transfer approach is a macroscopic one, averaging the phenomena inside an elementary volume. A solution of the integral equation derived by Twersky has recently been obtained by Lin and Ishimaru (1971), under the assumption of isotropic scattering, but raindrops are far from being isotropic scatterers (see section 3.12).

The complexity of the general problem is beyond the scope of this work. For the purpose of this study we investigate the simple case of coherent propagation, for which the scattered energy is a loss of the same kind as the one caused by absorption. The background noise due to thermal emission is also neglected. In section (4.3) we examine the conditions under which this model for coherent propagation can be used in studying incoherent systems.

4.2. Hypotheses

Furthermore, we simplify the problem of coherent propagation through rain, by introducing the following hypotheses:

a. The incident radiation is a plane wave. This assumption limits the spatial variation to a single variable and eliminates all angular dependence. Only the forward scattering properties of a particle are thus needed. In the case of a reflector type antenna, this assumption is justified in the far-field zone, which is considered to start at a distance Z such that

$$Z \geq \frac{2}{\lambda} \text{Diam}^2 \text{ (antenna)}. \qquad (4.3)$$

For a satellite receiver earth-station this distance can be quite large.

b. The shape of the drops is assumed to be spherical and their dielectric properties homogeneous, in order to make use of the theory developed in the previous chapter. However, no polarization effects in the forward direction can be accounted for by this model. We also assume the drops do not carry electrostatic charges.

c. The random motion of the drops is such as to destroy all cooperation effects in scattering. We shall call this type of scattering independent (sometimes also misleadingly referred to as incoherent). This assumption implies that the distance between the drops is large compared to the wavelength; this point has been questioned by Medhurst (1965) who speaks of drop "clustering" in actual rains.

d. In the forward direction the interference between the incident and the scattered wave takes place independently of the location of the drop. Thus the amplitudes may be coherently added.

e. The rain medium is assumed to be relatively transparent, so that each drop is illuminated by the incident plane wave. This seems a reasonable hypothesis, considering that the portion of the total volume occupied by the drops is of the order of 10^{-7} for a 10 mm/hr rain and 10^{-6} for a 150 mm/hr. (See curves for liquid water content as a function of rainfall intensity, section 4.4).

f. The diffuse intensity, whether scattered once or several times, is considered as a loss from the coherent beam. The total energy loss is thus simply proportional to the number of particles present in the rain volume considered.

With these restrictions in mind, we proceed now to the calculation of the propagation parameters per unit volume of homogeneous rain.

4.3. Volume propagation parameters.

Two approaches are possible in order to evaluate the extinction coefficient per unit volume of uniform rain. We shall show that both lead to the same final result.

A. - The first approach, used by Ryde (1941), considers a plane wave incident on a slab of rain of width dx located at a distance x along the path (see Figure 11). The number of drops per unit volume is expressed by $n(D,x,t)$. The power extracted from the incident wave by scattering and absorption inside this slab, is given under the assumption of single-scattering, by the sum of the effects due to each drop

$$dP = -P \cdot \int_D n(D,x,t) C_{ext}(\lambda,D) dD \cdot dx \qquad (4.4)$$

or

$$dP = -P \cdot \beta(\lambda,x,t) \cdot dx \qquad (4.5)$$

where $\beta(\lambda,x,t)$ is the power extinction coefficient per Unit volume for the coherent wave, expressed in cm^{-1} if

$C_{ext}(\lambda,D)$ as given by equation (3.22) is in cm^2.

The remaining signal power, after propagating a distance L through rain, is obtained by integration of (4.5)

$$P = P^i \exp\left(-\int_0^L \beta(\lambda,x,t) dx\right) \qquad (4.6)$$

where P^i is the incident power.

Equation (4.6) is the same as the one obtained from radiative transfer theory, neglecting the diffuse component of the signal. Part of the energy extracted from the incident beam will be present at the receiver, however, in the form of incoherent noise. This approach, as well as the radiative transfer approach, involves only the

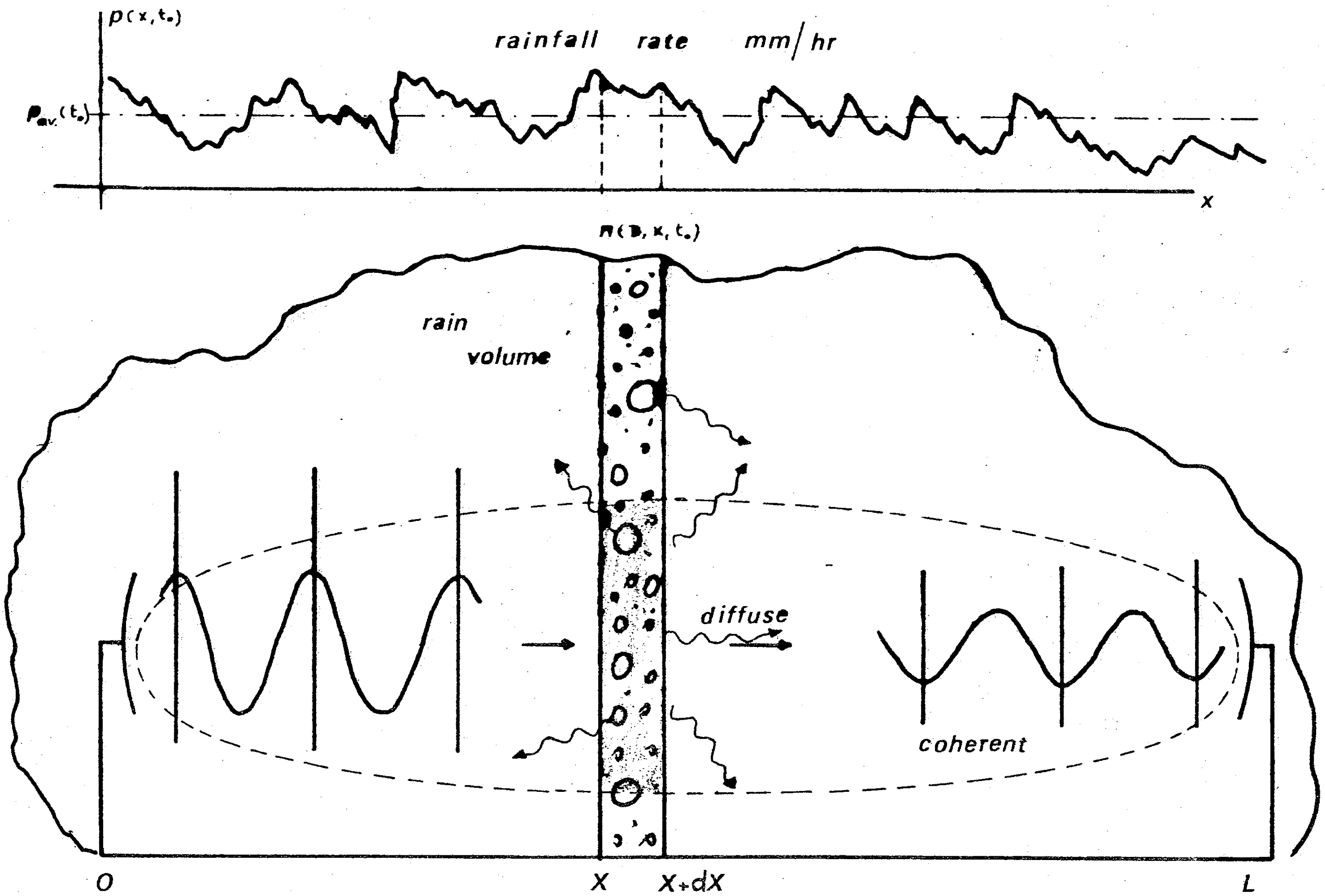

FIG. 11 GEOMETRY

power (modulus squared) of the signal and does not give any information on the phase of the attenuated coherent wave.

B. Another approach, first used by Rayleigh (1881) and developed by van de Hulst (1957), considers the wave propagating in the direction of incidence to be the result of interference between the incident plane wave and waves scattered in the forward direction or close to that direction. Summing the field intensities in an arbitrary direction is a very complicated task, since one must take into account the phase shifts introduced by the random position of the drops inside the slab. Furthermore, the resulting field intensity is very likely to be zero, due to the uniform distribution of the effective phase, to be expected with such a degree of randomness. Thus only a power approach is possible, since the resulting rms value will in general be different from zero.

This task is much simpler in the direction of propagation of the incident wave, since the interference takes place regardless of the position of the drop along x. The only phase shifts that occur are due to the scattering process itself ($\hat{S}_o(\lambda,D)$ is a complex function).

It is reasonable to assume that the incident plane wave is coherently influenced only by those scattered waves, originating in a volume delimited by the first Fresnel-zone (see Figure 11). The elementary volume dV is thus given by

$$dV = (L-x)\ \lambda\ dx = \frac{2\pi}{k_o}\ (L-x)\ dx \tag{4.7}$$

The hypothesis of single-scattering allows us to write the scattered field in the forward direction as the sum of the scattered waves by each individual drop inside the volume dV. We can thus write the far-field in the direction of the propagation as

$$\hat{E}^R = \hat{E}^i\ (1 + \int_D n(D,x,t)\cdot\hat{E}^s\cdot dD \cdot dV) \tag{4.8}$$

From equation (3.20) we get the intensity of the scattered field in the forward direction, expressed by

$$\hat{E}^s = \frac{\hat{E}^i}{jk_o(L-x)}\ \hat{S}_o(\lambda,D) \tag{4.9}$$

The forward-scattering function is assumed to be constant for small variations of the angle θ. From equations (4.7) to (4.9) we get

$$\hat{E}^R = \hat{E}^i\ (1 + \frac{(-j)}{jk_o(L-x)} \int_D n(D,x,t)\hat{S}_o(\lambda,D)dD\ \frac{2\pi(L-x)}{k_o}\ dx) \tag{4.10}$$

The factor (-j) has been introduced because the average phase lag over the first Fresnel-zone is $(-\frac{\pi}{2})$. The resulting far-field, after propagation through a slab of rain of width dx, may finally be expressed by

$$\hat{E}^R = \hat{E}^i\ (1 - \frac{2\pi}{k_o^2} \int_D n(D,x,t)\hat{S}_o(\lambda,D)dD \cdot dx) \tag{4.11}$$

and $\hat{S}_o(\lambda,D)$ is given by equation (3.18).

By comparing equation (4.11) with the result obtained for propagation of a plane wave through a medium of complex refractive index $|\hat{m}_e|<<1$

$$\hat{E}^R = \hat{E}^i \exp\ (-jk_o\hat{m}_e dx) \approx \hat{E}^i (1 - jk_o\hat{m}_e dx) \qquad (4.12)$$

we can characterize the slab of rain by an equivalent complex refractive index

$$\hat{m}_e(\lambda,x,t) = m_e' - j\ m_e'' = \frac{2\pi}{k_o{}^3} \int_D n(D,x,t)\hat{S}_o(\lambda,D)dD \qquad (4.13)$$

The free space propagation constant is included in $\hat{E}^i$. The assumption $|\hat{m}_e|<<1$ is verified by the computations (see section 4.6). From equation (3.28) it is easily found that

$$m_e'(\lambda,x,t) = \frac{1}{2k_o} \int_D n(D,x,t)C_{im}(\lambda,D)dD \qquad (4.14)$$

and

$$m_e''(\lambda,x,t) = \frac{1}{2k_o} \int_D n(D,x,t)C_{ext}(\lambda,D)dD \qquad (4.15)$$

The power extinction coefficient per unit volume is thus given by

$$\beta(\lambda,x,t) = 2k_o \cdot m_e''(\lambda,x,t) = \int_D n(D,x,t)C_{ext}(\lambda,D)dD \qquad (4.16)$$

which is the same result as the one derived in equation (4.5). Similarly, the excess phase due to propagation through rain may be obtained from

$$\varphi(\lambda,x,t) = k_o\, m_e'(\lambda,x,t) \text{ (rad/cm)} \tag{4.17}$$

It must be reminded here that this analogy with a continuous slab of equivalent complex refractive index is valid only for the coherent wave in the forward direction. It may not be used, for example, for calculating the energy reflected from rain; the reflectivity from rain must be calculated using the backward scattering function $\hat{S}_\pi(\lambda,D)$ (see equation 3.31).

4.4. Multiple-scattering and incoherent propagation

The effect of multiple-scattering on the coherent wave has been studied by Twersky (1962), who derived a first order solution for the equivalent refractive index of the form

$$\hat{m}_m = \hat{m}_e + \left[\left(\frac{2\pi}{k_o^3}\right) \int_D n(D,x,t)\ \hat{S}_\pi(\lambda,D)\,dD \right]^2 \tag{4.18}$$

Since the backscattered amplitude is usually small compared to the forward scattered amplitude, the effect of multiple-scattering on the coherent wave is negligible. Some investigations with the computer confirmed this statement. Thus, single-scattering formulas are sufficient to describe coherent propagation through rain (Crane 1966). The problem of multiple-scattering in the case of incoherent propagation still remains to be treated; in any case the effect is not expected to be negligible.

We examine now the applicability of the above theory in the case of an incoherent telecommunication system. It was shown by Crane (1971) that a Born approximation to the complete radiative transfer problem, i.e. the one including the incoherent source, reduces to the coherent propagation problem, under the condition

$$\beta_{scat} \cdot L < 1 \tag{4.19}$$

The maximum distance through uniform rain for which this criterion is satisfied has been calculated and is displayed in Figure 12. It is apparent that for frequencies less than 20 GHz rain can be treated as a purely absorbing medium for all rainfall rates and path length usually encountered (see also Figure 11). For frequencies larger than 20 GHz multiple-scattering is no longer negligible and its effects may appear for short paths in intense rain or for long paths in light rain. The average path length through rain for an earth-satellite link (Hogg 1971) is also shown on this graph.

Using the coherent channel formula for predicting the attenuation for incoherent systems will usually be a pessimistic approach, since part of the energy scattered in the medium will finally reach the receiver after multiple scattering. The trend is reversed when predicting bandwidth capability, since multiple-scattering will be associated with multipath fading and its bandwidth deterioration effects.

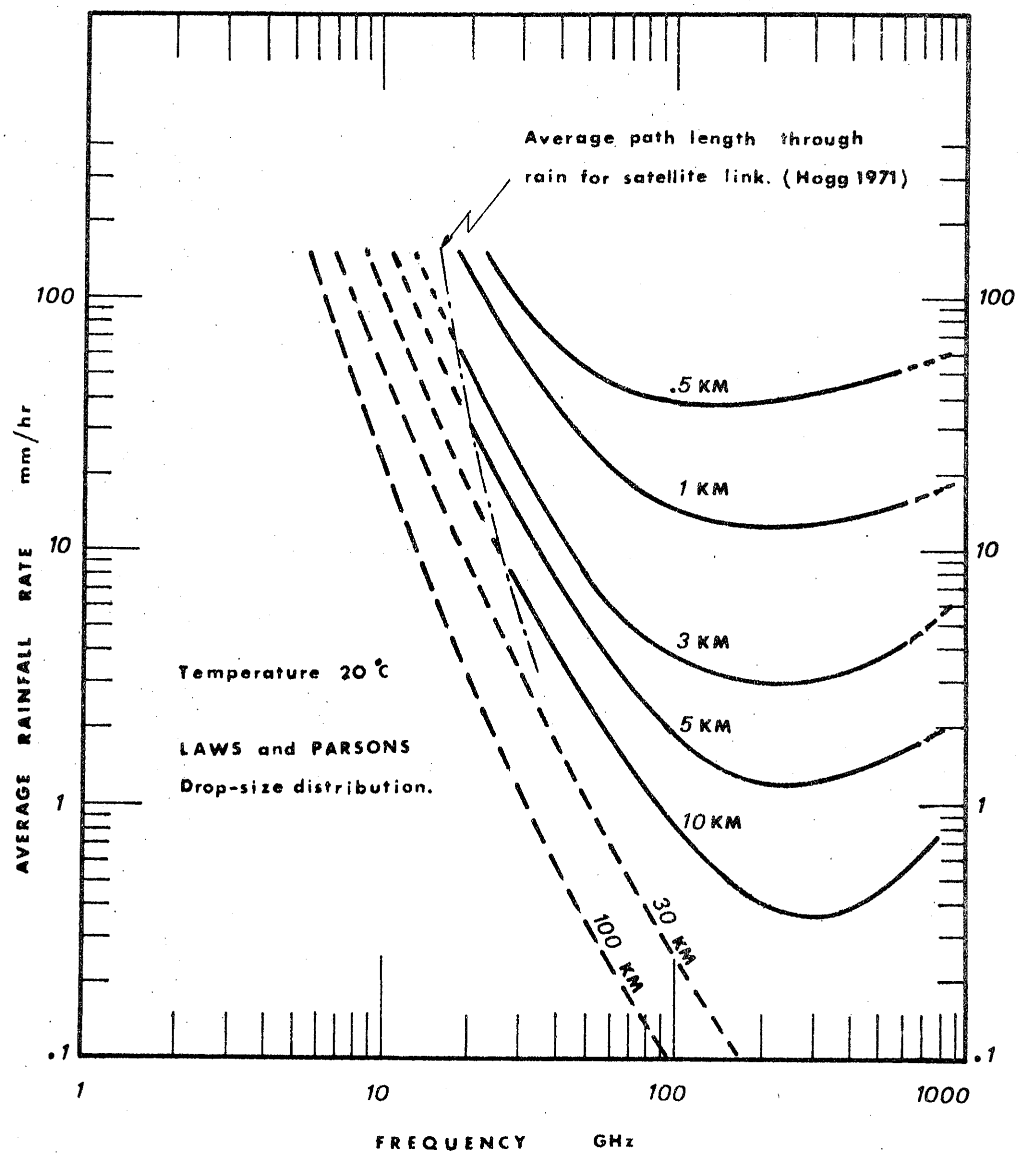

FIG. 12

MAXIMUM DISTANCE IN UNIFORM RAIN FOR WHICH MULTIPLE-SCATTERING EFFECTS CAN BE NEGLECTED

The only unknown left in the above equations is the drop-size distribution per unit volume which will be examined now.

4.5. Meteorologicals parameters

Rain is essentially an ensemble of scatterers randomly distributed in number, size, space, and time. The true meteorological parameter governing electromagnetic propagation through rain is thus the distribution of rain drops in number and size, at a given point and moment.

Meteorologists have studied drop-size distribution in rain for about one century; a good summary of their work may be found in Hardy (1962). The numerous investigators found these distributions to vary significantly with type of rain, geographic location, and season of the year. Rain associated with thunderstorms shows wider drop-size distribution than other rainfall; rain-drop distribution varies both in the vertical and horizontal direction as well as with time for a given shower. Evaporation, coalescence, accretion, and wind direction and intensity are the main physical mechanisms governing these fluctuations.

Measurements of drop-size distribution in rain have been performed using such diversified techniques as flour pellets, filter paper, raindrop camera, Doppler radar, photoelectric devices and acoustic microphones. Each method has its advantages and disadvantages and in a certain sense they are complementary. All of these, with the possible exception of the last two mentioned, are very tedious when it comes to reducing data, and they show a wide scatter in the measured points. This clearly shows the statistical nature of drop-size distribution in rain. Except for very low frequencies, the water content is not enough to describe the effect of rain on an electromagnetic wave; the way the total volume of water is distributed among rain drops of different sizes plays an important role. However, due to difficulties in measuring the drop-size distribution $n(D,x,t)$, this parameter is not commonly used. A more easily measurable, and therefore more commonly available parameter, is the point rainfall rate $p(x,t)$. Both parameters are related by

$$p(x,t) = 1.885\ 10^6 \int_D n(D,x,t)\,[v(D)-w(x,t)]\,D^3\, dD \qquad (4.20)$$

where D is the drop diameter (cm)

$v(D)$ is the terminal velocity of the drop (m/sec)

$w(x,t)$ is an uncertainty factor on the vertical velocity of the drop, due to turbulence (m/sec)

$n(D,x,t)$ is the instantaneous, local drop-size distribution (drops/cm^3 cm^{-1}) and

$p(x,t)$ is the ground instantaneous point rainfall rate as measured by a fast raingauge (mm/hr).

The terminal velocity of a falling raindrop has been measured by Gunn and Kinzer (1949) and values can be found in Medhurst (1965). The uncertainty factor $W(x,t)$ is a difficult parameter to measure and it has been usually disregarded and taken equal to zero. This assumption can lead to a substantial amount of error as will be shown later. Values of $p(x,t)$ are available from weather bureaus, usually averaged over one-hour periods. More recently, rain-gauges with a resolution time better than one second have been designed (Semplak 1966).

From equation (4.16) it is evident that $p(x,t)$ is not a single-valued function of $n(D,x,t)$. Even when neglecting the randomness introduced by the vertical component of the wind, there is an infinite set of distributions $n_i(D,x,t)$ that, when integrated, will lead to the same rainfall rate. Since the propagation parameters are related to the drop-size distribution, not to the integrated water content, a scatter of points will appear in the $(\beta\text{-}p)$ plane, for example, when relating specific attenuation to rainfall-rate. Notice that we have not yet introduced the fluctuations due to the variations of precipitation rate in space and time.

If we define the statistical average of the n_i distributions for a given rain intensity p(mm/hr) as

$$N(p,D) = \langle n_i(D,x,t) \rangle \quad , \tag{4.21}$$

then the relationship between p and N becomes single-valued. The first investigators to measure such average distributions were Laws and Parsons (1943); their data are the result of three years of measurements in the

Washington, D.C. area. In fact the did not measure $N(p,D)$ but a related distribution $M(p,D)$ which expresses the average percentage of precipitation rate, P, that is due to drops of diameter D. $N(p,D)$ may be obtained from this distribution through

$$N(p,D) = \frac{M(p,D)\cdot p}{1.885\ 10^{8}(v(D)-W)D^{3}}\ (\text{drops/cc}\cdot\text{cm}^{-1}) \qquad (4.22)$$

if D the drop diameter is in cm

p the precipitation rate in mm/hr

v(D) and w are in m/sec,

M(p,D) in percent.

The function $M(p,D)$ is given for a number of precipitation rates and for a discrete number of drop diameter intervals ΔD, centered at D. A median drop diameter D_o is obtained such that half the intensity of rainfall is caused by drops of diameter smaller or equal to D_o. This median diameter is related to the precipitation rate by

$$D_o(\text{mm}) = 1.24\ p^{0.182}\ (\text{mm/hr}) \qquad (4.23)$$

Laws and Parsons' tables also show a maximum diameter for the drops, which is a function of the intensity of precipitation. Rain drops of diameter larger than 7 mm very seldom exist, since the surface tension is not strong enough to keep them together. The median and maximum diameters are shown in Figure 13 as a function of rainfall rate. The tendency for intense rain to have

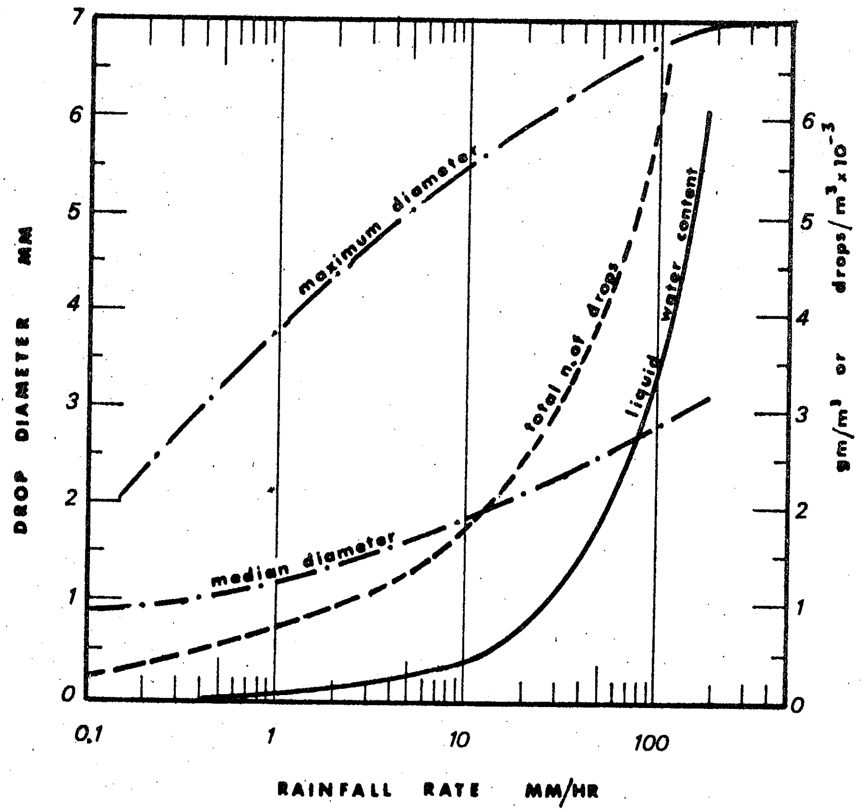

FIG. 13

THE LAWS AND PARSONS DROP-SIZE DISTRIBUTION
AND SOME RELATED PARAMETERS

larger drops and also a wider distribution of drop diameters is clearly evidenced. The total number of drops per unit volume N_t and the liquid water content L are also shown in this figure.

$$N_t \ (p) = \int_D N(p,D) \ dD \quad (\text{drops/cc}) \qquad (4.24)$$

and

$$L \ (p) = \int_D N(p,D) \ \frac{\pi D^3}{6} \ dD \ (\text{gm/cc}) \qquad (4.25)$$

since the density of water is approximately equal to 1 gm/cc.

It has been shown by Crane (1966) that the theoretical curve using Laws and Parsons (L.P.) distribution provides the best fit for measurements in New England rain. In a recent paper by Semplak (1971) a similar conclusion is reached for measurements in New Jersey. Since the L.P. distribution is the most widely used today, it will be adopted for this study, keeping in mind that it may not be suitable for all types of rain.

Numerous workers have tried to fit a continuous mathematical function to the Laws and Parsons discrete distribution. The advantage of having a continuous distribution rather than a discrete one is that it allows to choose adaptative integration steps or to use a Gaussian quadrature technique.

The simplest of those fits, since it contains only one adjustable parameter, is due to Marshall and Palmer

(1948). They found that the Laws and Parsons distribution can be reasonably well approximated by

$$N(p,D) = N_o \exp(-C \cdot D) \qquad (4.26)$$

where

$$N_o = 8.10^{-2} \ (\text{drops/cc.cm}^{-1})$$

$$C = 41.\ p^{-0.21} \ (\text{cm}^{-1} \text{ if } p \text{ is in mm/hr})$$

Figure 14 shows a comparison of this distribution with data points obtained from the Laws and Parsons distribution using equation (4.18). It appears that the Marshall-Palmer distribution approximates the measured distribution quite well for large drop diameters and low to moderate rain intensities. For drop diameters less than 1.5 mm however, it has a tendency to exaggerate the number of drops. Also, it does not go to zero for zero drop diameter, as might be expected. For practical calculations the range of D may be limited to

$$0.5\,(\text{mm}) \leq D \leq 2.75\ p^{0.21}\ (\text{mm}). \qquad (4.27)$$

The upper bound is found by setting $N(p,D) \leq 10^{-6}$ (drops/cc.cm^{-1}). Some more sophisticated fits, having more than one parameter, may be found in the literature (e.g. Fowler and LaGrone 1969). Due to their greater complexity, they have not been as widely used as the Marshall-Palmer distribution, and will not be discussed further in this study.

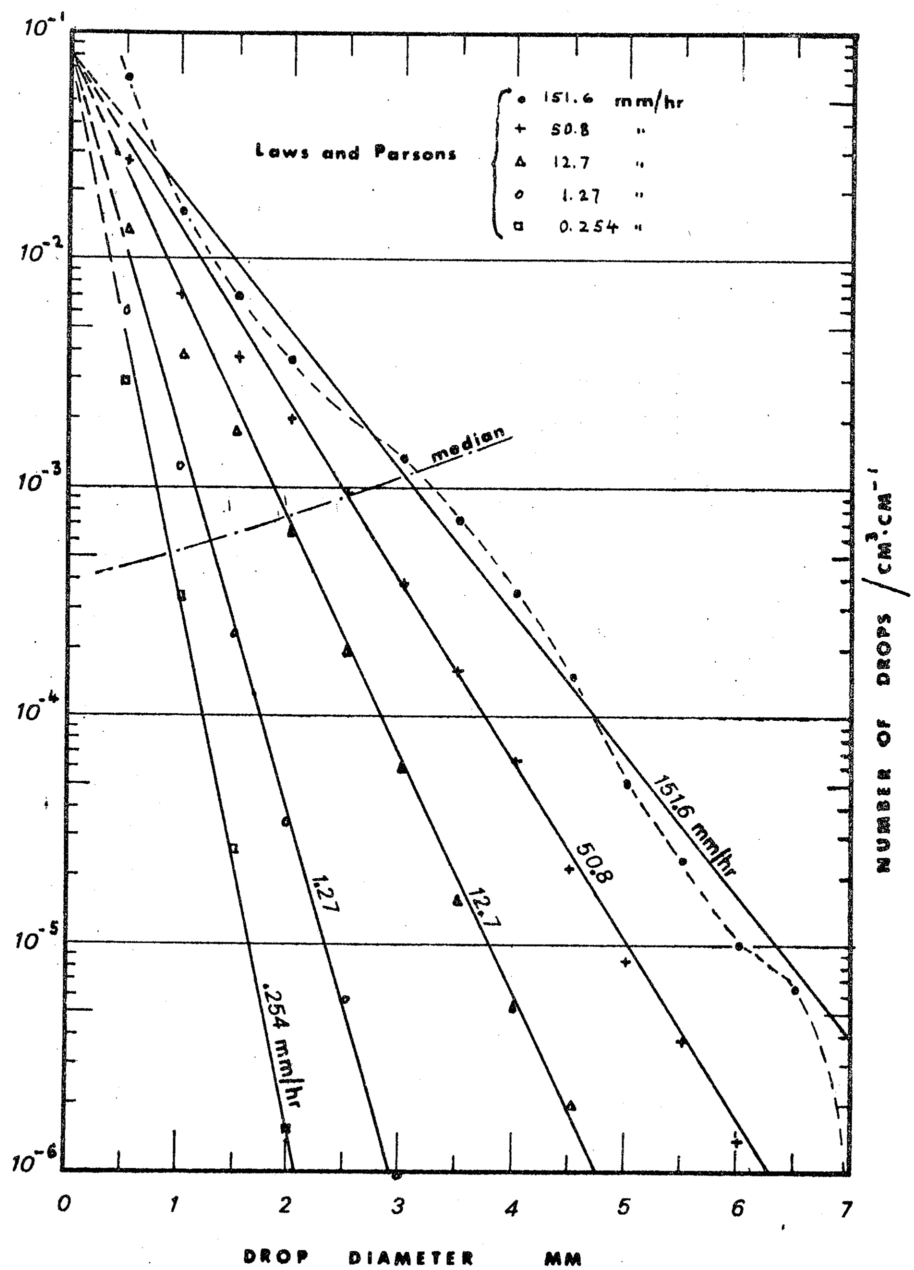

FIG. 14

COMPARISON OF THE MARSHALL-PALMER DROP-SIZE DISTRIBUTION (SOLID LINES) WITH THE LAWS AND PARSONS, FOR SELECTED RAINFALL INTENSITIES

4.6. The rainy atmosphere transfer function

We have shown in section (4.3) that the propagation of the coherent radiation through rain could be expressed in the case of a plane wave by

$$\hat{E}^R = \hat{E}^i \exp(-jk_o \hat{m}_e(\lambda,x,t)dx) \tag{4.28}$$

where $\hat{m}_e(\lambda,x,t)$ is still a random function of space and time, due to the random characteristics of $n(D,x,t)$. If we assume that the statistical averaged drop-size distribution is given by the Laws and Parsons distribution, we can derive the average intensity of the field as a function of the point rainfall rate $p(t)$

$$<\hat{E}^R> = \hat{E}^i \exp(-jk_o <\hat{m}_e(\lambda,p)>dx) \tag{4.29}$$

where

$$<\hat{m}_e(\lambda,p)> = \frac{2\pi}{k_o^3} \int_D N(p,D)\hat{S}_o(\lambda,D)dD \tag{4.30}$$

The function $<\hat{m}_e(\lambda,p)>$ is now a deterministic function of the rainfall rate and is time varying according to $p(t)$.

Uniform rain of intensity p(mm/hr) can thus be viewed as having a transfer function

$$\hat{H}(\lambda,P) = \exp\left[-jk_o(1+<\hat{m}_e(\lambda,p)>)dx\right] \tag{4.31}$$

or, since $k_o|<\hat{m}_e(\lambda,p)>|$ is less than one (see Figure 15).

$$\hat{H}(\lambda,P) \approx \exp(-jk_o dx)\cdot(1-jk_o<\hat{m}_e(\lambda,p)>dx) \tag{4.32}$$

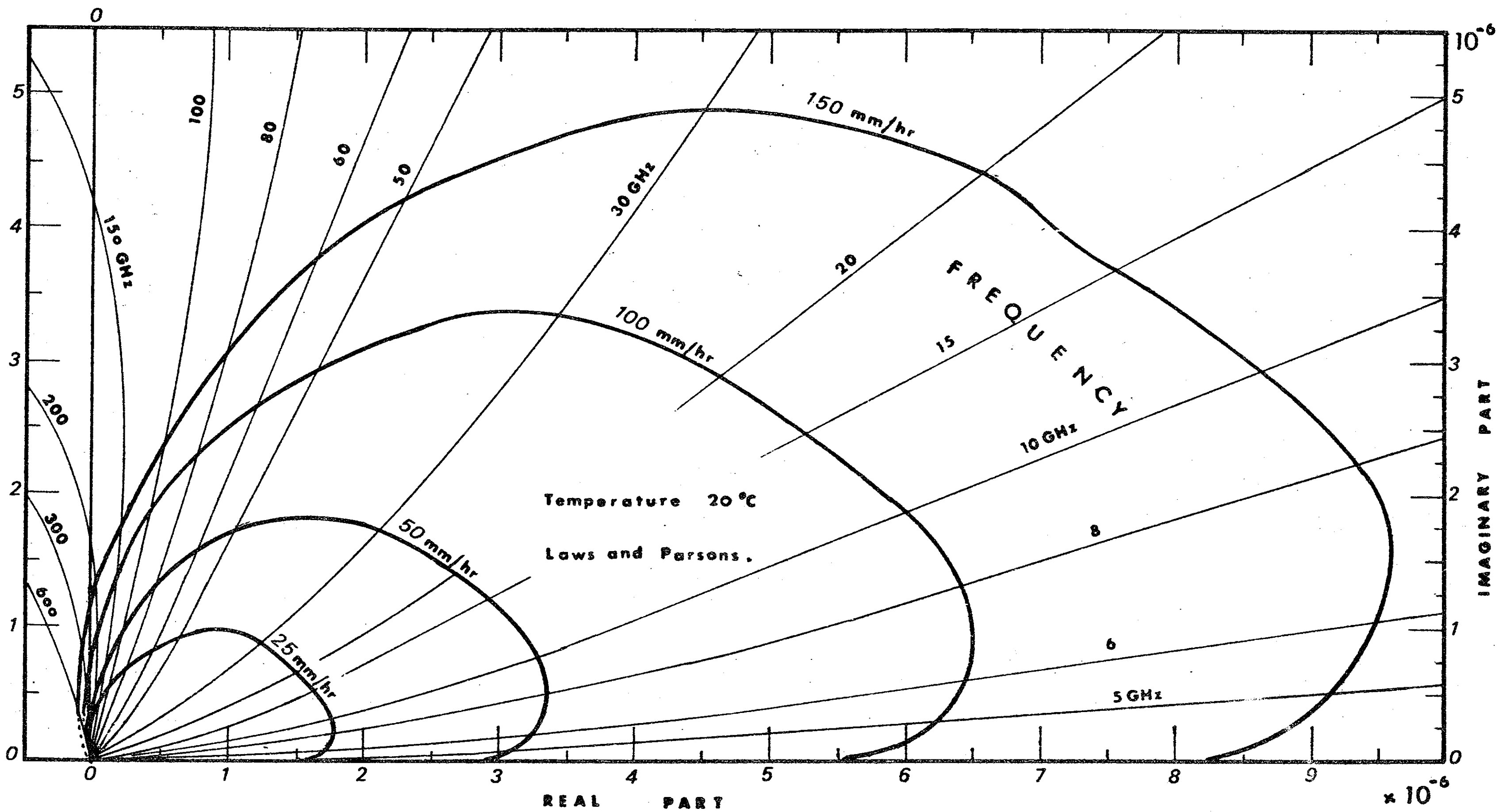

FIG. 15. THE FUNCTION $<m_e(\lambda,p)>$ IN THE COMPLEX PLANE.

per unit length of propagation, for the average field component. The term $\exp(-jk_s x)$ is the free space propagation delay. The function $\langle m_e(\lambda,p)\rangle$ is plotted in Figure 15 for selected values of the precipitation rate. Notice the 10^{-6} scale factor. It is also shown in its real and imaginary part versus frequency in Figures 16 a and b. The negative value of the real part for frequencies larger than 200 GHz at high rainfall rates is less than -0.1 (10^{-6} units) and thus almost negligible in comparison with the positive values that may be reached.

It seemed interesting to compare the complex refractive index of water (see Appendix I) with the equivalent refractive index for rain at different intensities. Since the latter is 10^{-6} smaller in absolute value than the former, we compare a one micron thick slab of water with a one meter slab of rain (see Figures 16 a and b.). From Figure 16a it is apparent that water has stronger phase shift effects at millimeter wavelengths than rain of any intensity. Also from Figure 16b we deduce that a rain of 100 mm/hr has about the same absorption characteristics as a slab of water one million times thinner. This fact illustrates the good transparency of rain medium in the microwave region.

In the Rayleigh region ($|\hat{m}z| \ll 1$), the forward scattering function can be approximated by (see Section 3.6)

$$\hat{S}_o^R(\lambda,D) \approx j\,\hat{K}\,z^3 \tag{4.33}$$

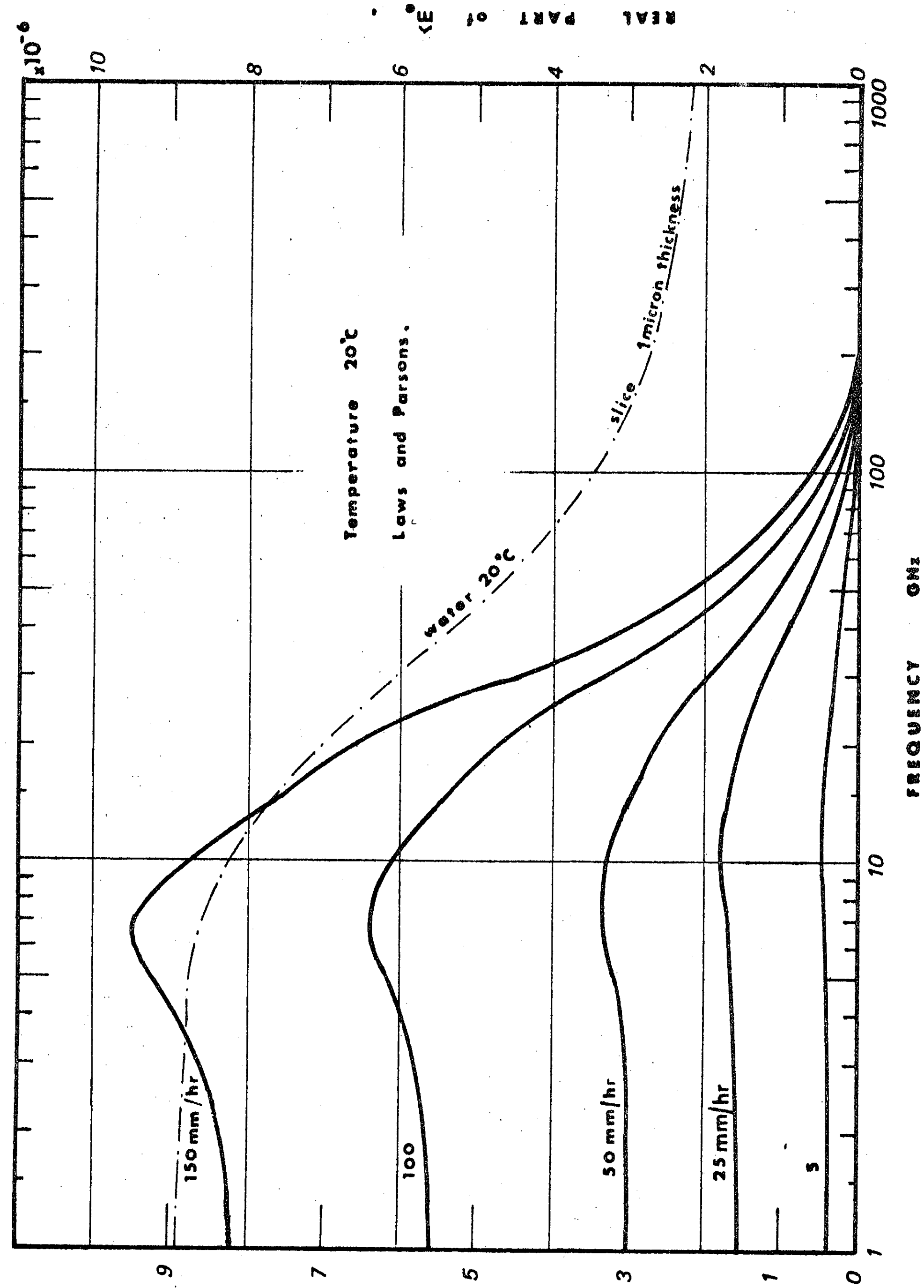

FIG. 16a

THE REAL PART OF THE EQUIVALENT REFRACTIVE INDEX

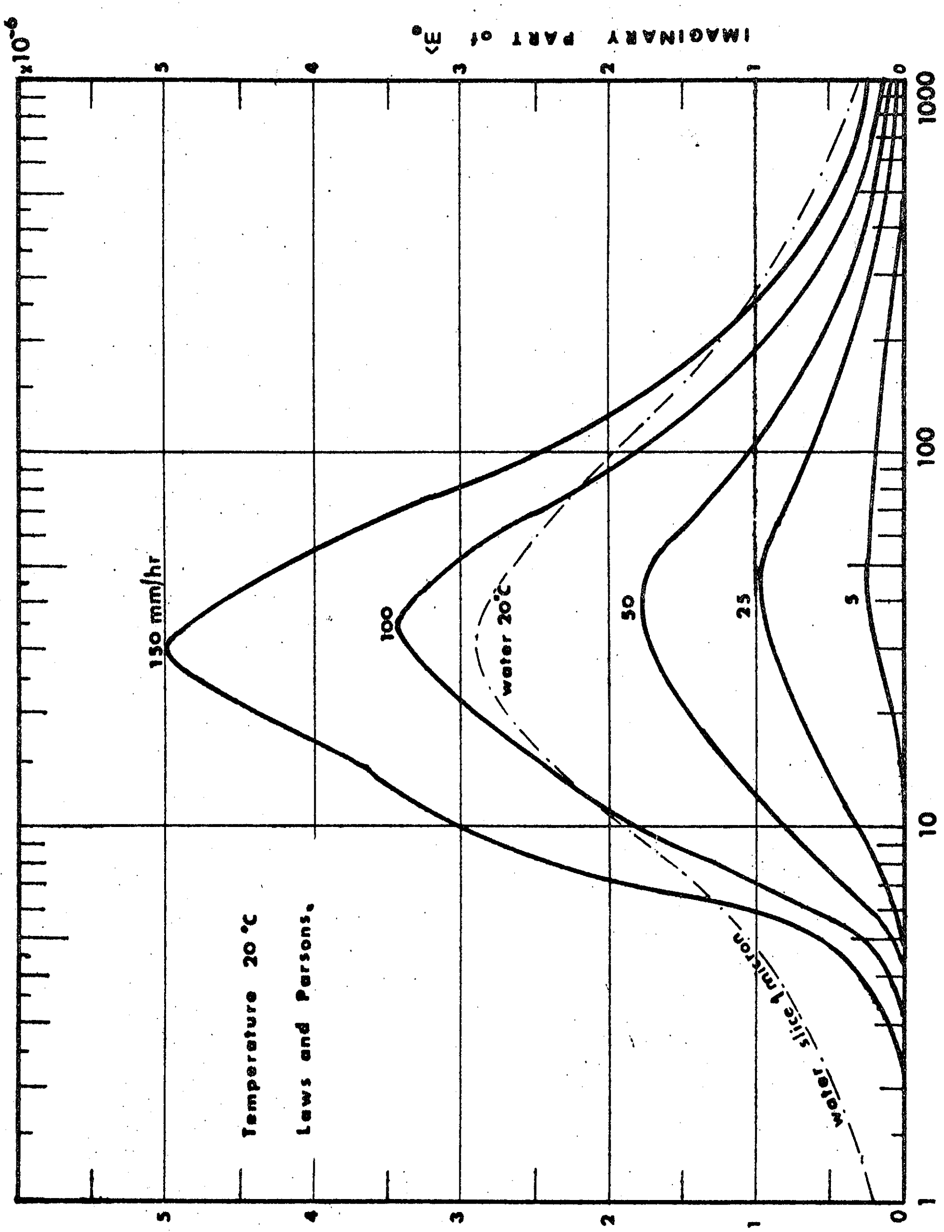

FIG. 16b

THE IMAGINARY PART OF THE EQUIVALENT REFRACTIVE INDEX where

$$\hat{K} = \frac{\hat{m}^2 - 1}{\hat{m}^2 + 2} = K' - j\, K'' \tag{4.34}$$

and $\hat{m}$ is the complex refractive index for water. Hence, the equivalent refractive index for the medium takes the from

$$\langle \hat{m}_e^R(\lambda, P) \rangle = j\frac{3}{2}\, \hat{K}\ (\lambda)\ L(p) \tag{4.35}$$

where L(p) is the liquid water content, as defined by (4.25). Equation (4.35) shows that, whenever scattering is negligible as compared to absorption, the propagation phenomena depend only on the amount of water that is present in the path (the first Fresnel ellipsoid volume in the case of coherent propagation) and not on the way it is distributed among the different drop diameters. This situation mainly occurs for fog at centimeter and millimeter wavelengths.

4.7. Propagation in non-uniform rain

When studying the propagation along a path of length L, we have to take into account the contribution of all the slices of width dx, limited by the first Fresnel ellipsoid (see Figure 11). The hypotheses of single-scattering and transparency of the rain medium allow us to write, for the resulting coherent field at the receiver

$$\hat{E}^R = \hat{E}^i\ \left(1 - \frac{2\pi}{k_o^2} \int_o^L \int_D n(D,x,t)\, \hat{S}_o(\lambda,d)\, dD \cdot dx\right) \tag{4.36}$$

The statistical average of the field is obtained using a Laws and Parsons drop-size distribution

$$\langle \hat{E}^R \rangle = \hat{E}^i \left(1 - \frac{2\pi}{k_o^2} \int_o^L \int_D N(p,D)\hat{S}_o(\lambda,D)\,dD \cdot dx\right) \qquad (4.37)$$

This function is still random, since the point rainfall rate is a random function of space and time (see Figure 11). In order to get an estimate of the average field component at the receiver we introduce a path-averaged rainfall rate defined by

$$R_{av}(t) = \frac{1}{L} \int_o^L p(x,t)\,dx \qquad (4.38)$$

or, in the case of a finite number of sampling points along the path

$$R_{av}(t) = \frac{1}{L} \sum_{i=1}^{N} p(x_i,t) \cdot \Delta x_i \qquad (4.39)$$

where x_i is the estimated zone of influence of the ith gauge, with the condition $\sum \Delta x_i = L$. The field component $\langle E^R \rangle$ is now given by

$$\langle \hat{E}^R \rangle_{av.} = \hat{E}^i \left(1 - \frac{2\pi}{k_o^2} \int_D N(R_{av},D)\hat{S}_o(\lambda,D)\,dD\right) \qquad (4.40)$$

and is only a random function of time, as in the case of uniform rain. It can be noted that this procedure is analog to defining an equivalent refractive index by

$\langle m_e(\lambda, R_{av}) \rangle$ (see equation 4.30)

Equation (4.40) still leads to an interpretation in

COHERENT PROPAGATION THROUGH UNIFORM RAIN.

$$\langle \hat{E}^R \rangle = \hat{E}^i \left(1 - \frac{2\pi L}{k_o^2} \int_D N(R_{av}, D)\, \hat{S}_o(\lambda, D)\, dD \right)$$

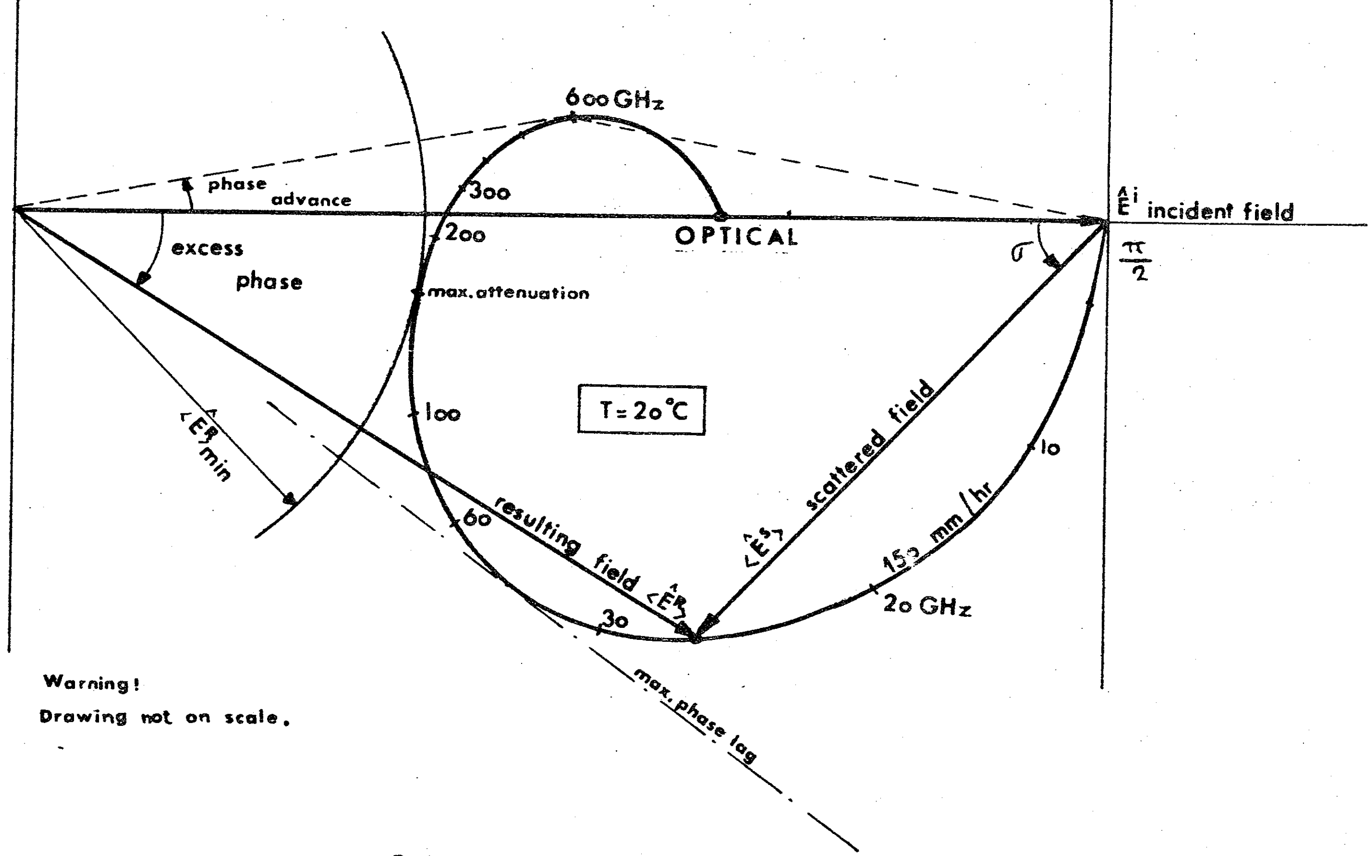

FIGURE 17.

terms of a transfer function. An example of coherent propagation through rain for a path length of 0.3 km and a path-averaged intensity of 150 mm/hr is given in Figure 17 which indicates the locus of the resulting phasor as a function of frequency. This graph is purely qualitative and has not been drawn on scale. However, the main characteristics of coherent propagation through rain, such as maximum phase lag, maximum attenuation, phase advance at high frequencies, clearly appear on the graph. Such locus could be drawn for any rainfall intensity, resulting in a family of curves. The effect of an increase in path length is to distort the locus, according to a geometric transformation which is an affinity + a rotation.

4.8. Propagation effects due to rain in earth-space links

For a satellite path, at a fairly high elevation angle, both vertical and horizontal drop-size variations are important. It is expected that the median diameter of the drops trends towards larger values when moving from the base of the cloud towards the earth surface; this is due to such phenomena as coalescence and accretion. Since propagation parameters are very sensitive to drop-size distribution, it is not impossible that for a vertical path the effect of rain may be less than for an equivalent horizontal path. To the author's knowledge no satisfactory study of this problem has been made yet.

The ground measured rainfall rate, even if measured below the path, is of not much use in predicting attenuation for earth-space paths. Increasing delays, due to the finite falling speed of raindrops, are introduced in the measurements when going away from the transmitter. However, good correlation has been obtained by Ippolito (1971) when weighting the ground measured precipitation rates by a formula of the type

$$R_{av}(t) = \frac{1}{N} \sum_{i=1}^{N} (1-\frac{h_i}{H}) \; P_i(t) \qquad (4.34)$$

where h_i is the height of the path above the ith gauge

$P_i(t)$ is the point rainfall rate measured by the ith gauge

H is the maximum height of the path in the rain cell.

Measurement of the water content in the path could also be determined by radar. However, radar is very sensitive to snow and hail particles, which cause only little attenuation, and its quantitative indications are tarnished by error due to absorption by the drops.

A recent analysis by Hogg (1971) of sun tracker measurements at two different frequencies provides us with an effective path length through rain for an earth-space path. Hogg's curve is reproduced in Figure 18; it shows that intense showers are limited in extent, whereas light rain is spread out over tens of km. Using

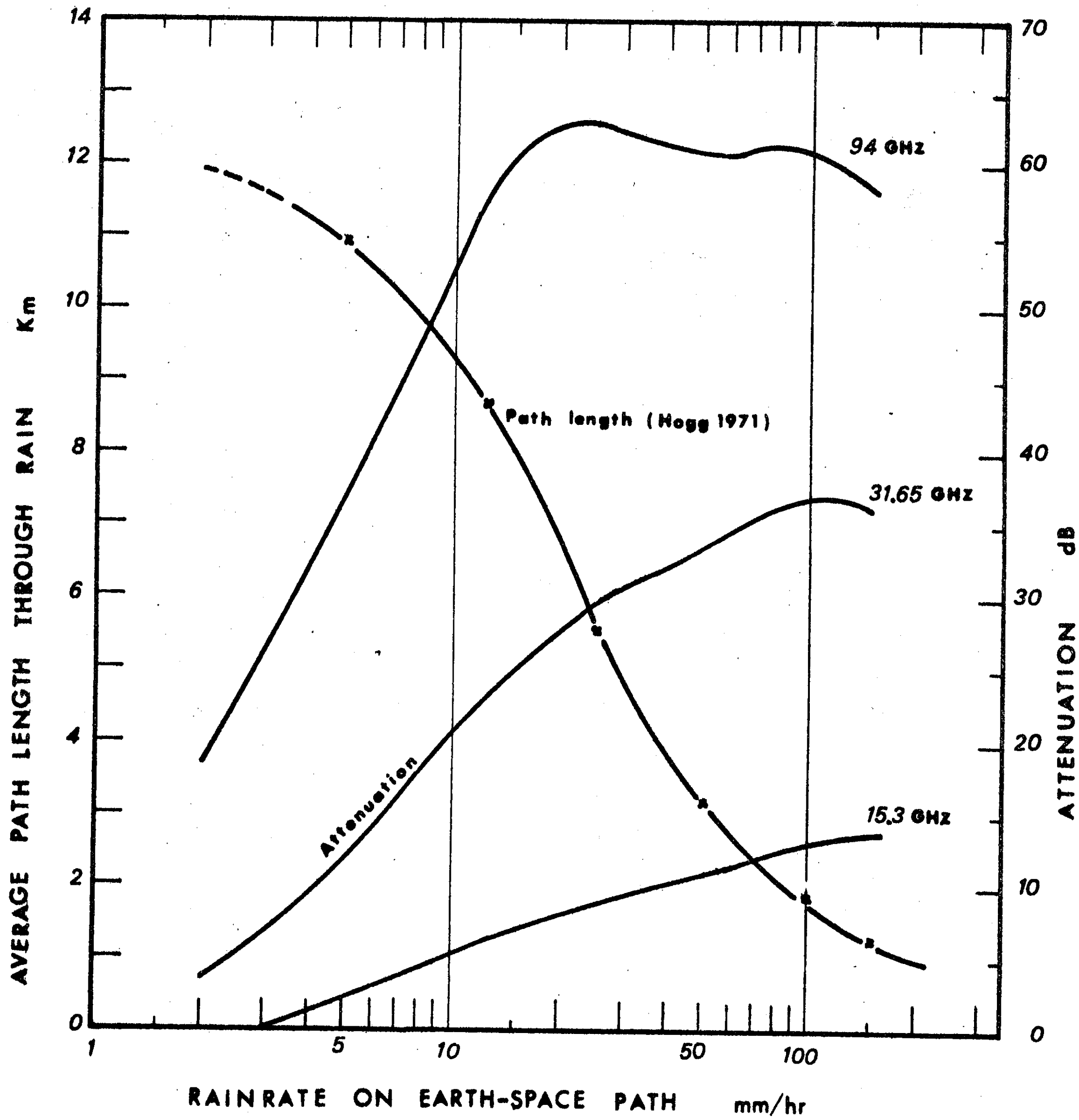

FIG. 18

CALCULATED AVERAGE ATTENUATION ON EARTH-SPACE PATH, AS A FUNCTION OF RAINFALL RATE this effective path length, the excess attenuation due to rain, at three different frequencies, has been calculated and is shown on the same plot (in db). It is apparent that a 15 db fade margin may be sufficient at 15.3 GHz, whereas it has to be increased to about 40 db at 31.65 GHz and to an excessive 65 db at 94 GHz. The curve for 15.3 GHz is in good agreement with the ATS-V experimental results (Ippolito, 1971).

4.9. Conclusion

In this chapter the rainy atmosphere has been shown to have a behavior equivalent to a lossy dispersive medium; this is exactly true for coherent propagation in uniform rain. The model can be extended to non-uniform rain, by introducing a path-averaged rainfall rate, and to incoherent propagation, under the condition that scattering is reasonably small compared to absorption.

Such a model enables us to compare average measured variations of the signal with those calculated from almost instantaneous rainfall rates, measured along the path. This is what is done in experiments designed to verify the validity of this theory. To the author's knowledge, none of these experiments have treated meteorological data with enough accuracy to be able to decide as to the validity or the non-validity of this theory.

In the design of microwave links, there is no need for instantaneous rainfall rates; a cumulative distribution of rainfall rates along the path is sufficient. It has been shown by Bussey (1950) that under certain restrictions, not yet fully determined, the path statistics may be dervied from the point statistics. It has also been shown by Ruthroff (1970) that a cumulative distribution curve for the attenuation obtained from point rainfall data using Laws and Parsons' drop-size distribution, provides an upper-bound to the measured curve.

In both cases, however, there is a need for a theoretical relationship between attenuation and/or phase velocity and rainfall rate, which is what we are going to investigate in the next two chapters.

CHAPTER 5

THE ATTENUATION COEFFICIENT FOR COHERENT PROPAGATION THROUGH RAIN

5.1. Introduction

In this chapter we are interested in the power attenuation of the coherent signal after propagating through homogeneous rain of average intensity R_{av}. Two models relating the attenuation coefficient to the precipitation rate will be examined. The influence of the drop-size distribution and temperature of the rain drops on the attentuation coefficient is then discussed. A comparison of measurements with theory concludes this chapter.

5.2. The attenuation coefficient

From the equivalent refractive index model for a rainy atmosphere we deduce the power attenuation coefficient

$$<\beta(\lambda,R_{av})> = 2k_o<m_e''(\lambda,R_{av})> = \int_{D_{min}}^{D_{max}} N(R_{av},D)\,C_{ext}(\lambda,D)\,dD \tag{5.1}$$

The attenuation coefficient obtained this way is expressed in (cm^{-1}). A more practical coefficient is defined in dB/Km; we have

$$<\gamma> = 4.343\ 10^5\ <\beta>\ \text{(dB/Km)} \tag{5.2}$$

From equation (5.1), it appears that the attenuation coefficient is a function of frequency and path-averaged rainfall rate; it also depends from temperature and drop-size distribution. In this study we have adopted the Laws and Parsons distribution and a drop temperature of 20 °C.

Calculations of attenuation coefficients have been undertaken by several investigators: Ryde and Ryde (1945), Gunn and East (1954), Oguchi (1964), Medhurst (1965) and Setzer (1971). The first calculations suffered some inaccuracy, due to the lack of adquate automatic computing devices. Modern high-speed digital computers allow us to obtain those coefficients quite rapidly and inexpensively. Our own computations were compared with those of previous workers; they agreed within reasonable accuracy with Medhurst's computations, the slight differences being attributed to differences in the value of the refractive index of water. Setzer's results, however, are slightly larger than ours, although he uses the same values for the refractive index of water; this tendency towards exaggeration is especially marked at low rainfall rates, where his results are 30 to 40% larger than ours.

The author does not believe that a tabulation of these coefficients for different values of rainfall rate, temperature, frequencies, raindrop distributions, etc. would be very useful. In a particular problem, when such coefficients are needed, they can be obtained quite inexpensively using a computer program such as the one described in Appendix 2 of this study. However, in order

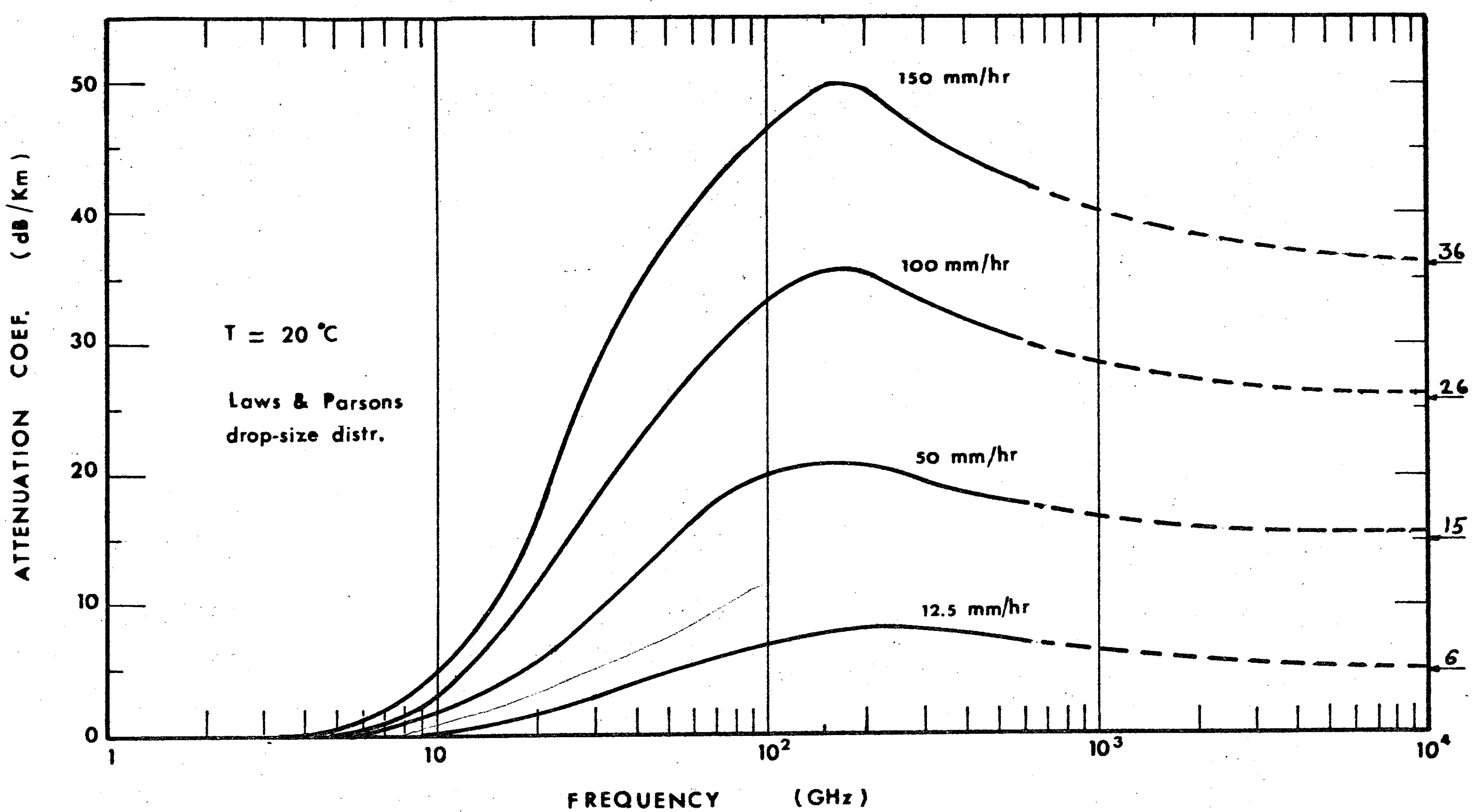

FIG. 19

THE AVERAGE ATTENUATION COEFFICIENT AS A FUNCTION OF FREQUENCY, FOR SELECTED RAINFALL RATES.

to discuss general trends, the attenuation coefficient due to rain has been plotted in Figure 19 as a function of frequency, for selected values of rainfall intensity. This plot serves to illustrate the fact that the attenuation reaches a maximum at a frequency of about 150 GHz; this maximum is more pronounced for intense showers than for light rains, and is of the order of 50 dB/Km for a 150 mm/hr rain. The decrease of the attenuation coefficient at wavelengths less than about 2 mm is not due, like many authors pretend, to the pronounced effect of forward scattering at those frequencies; in this model, all scattered energy is considered as a loss and the decreasing trend may only be explained by the fact that the drops responsible for the chief part of attenuation are no longer in the Mie region at those frequencies. Asymptotic values of those coefficients are obtained using the geometric cross-section of the drop; they are indicated by arrows on the right hand vertical scale. In the far infrared region, a smooth transition has been assumed, although values of the refractive index from Chapter 2 should be introduced into the computer program in order to calculate those coefficients. Another useful plot is an isocontour plot in the frequency - rainfall intensity plane; this allows us to visualize immediately the regions of high attenuation or to find the order of magnitude of the attenuation to be expected in given circumstances. Figure 20 indicates that the attenuation

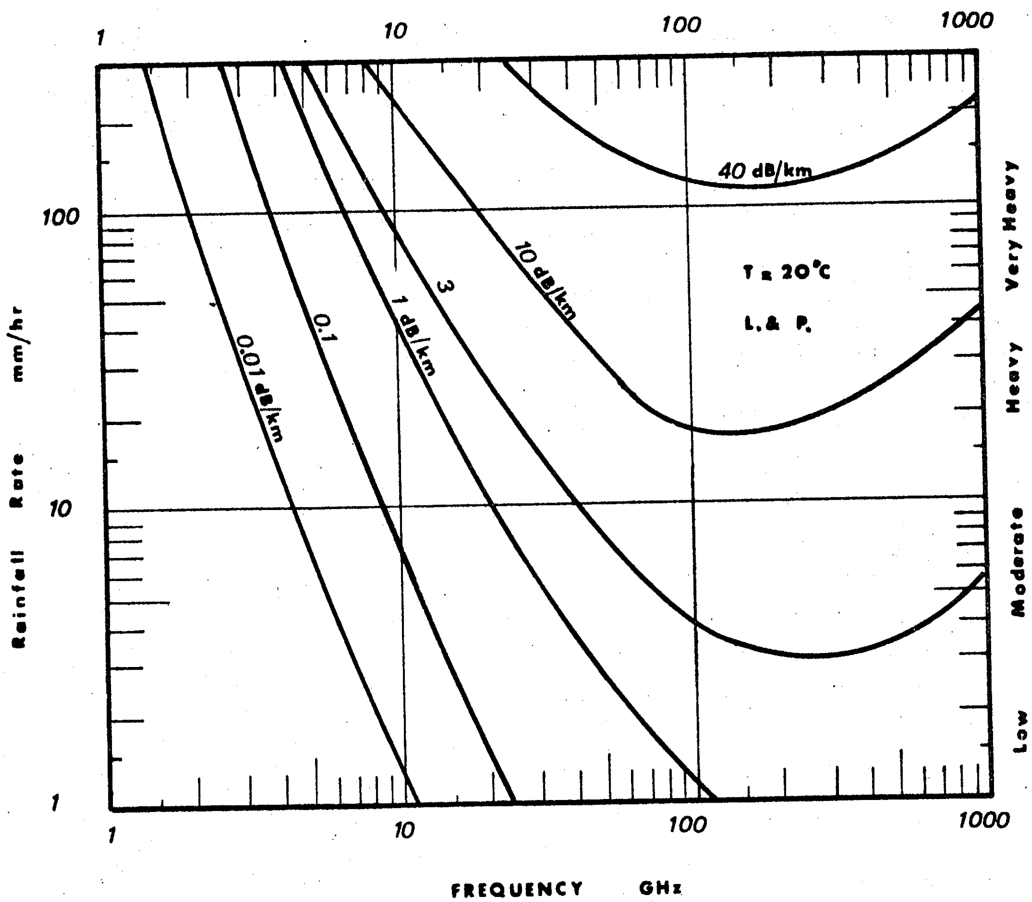

FIG. 20

THE AVERAGE ATTENUATION COEFFICIENT AS A FUNC- OF FREQUENCY AND RAINFALL RATE

rate to be expected at frequencies below 10 GHz is less than 3 dB/Km for rainfall rates less than 100/hr; that is why attenuation due to rain is commonly considered as a problem of minor importance at those frequencies.

5.3 Attenuation as a function of rainfall intensity

The specific attenuation coefficient can be defined as the ratio of the attenuation coefficient to the rainfall intensity that causes the attenuation. This ratio is shown in Figure 21 as a function of rainfall rate. Extreme variations of about one order of magnitude can be seen in Figure 21, the largest changes occuring at both extremes of the frequency range considered in this study. This leaves no hope of establishing a linear relationship between attenuation and rainfall rate, except in the 30 to 50 GHz band where the curves are nearly horizontal.

The attenuation coefficient as a function of rainfall rate can be obtained accurately from the computer program; parameters such as frequency, temperature, raindrop distribution, etc. can be changed at will. Thus, there seems to be no need for constructing a simple model. However, people measuring attenuation coefficient as a function of rain intensity obtain a scatter of points in the ($\langle\beta\rangle$, R_{av}) plane. To compare their measurements with theory, they try to fit least-square error regression curves to their data. Two of the most popular regressions are the linear and the logarithmic.

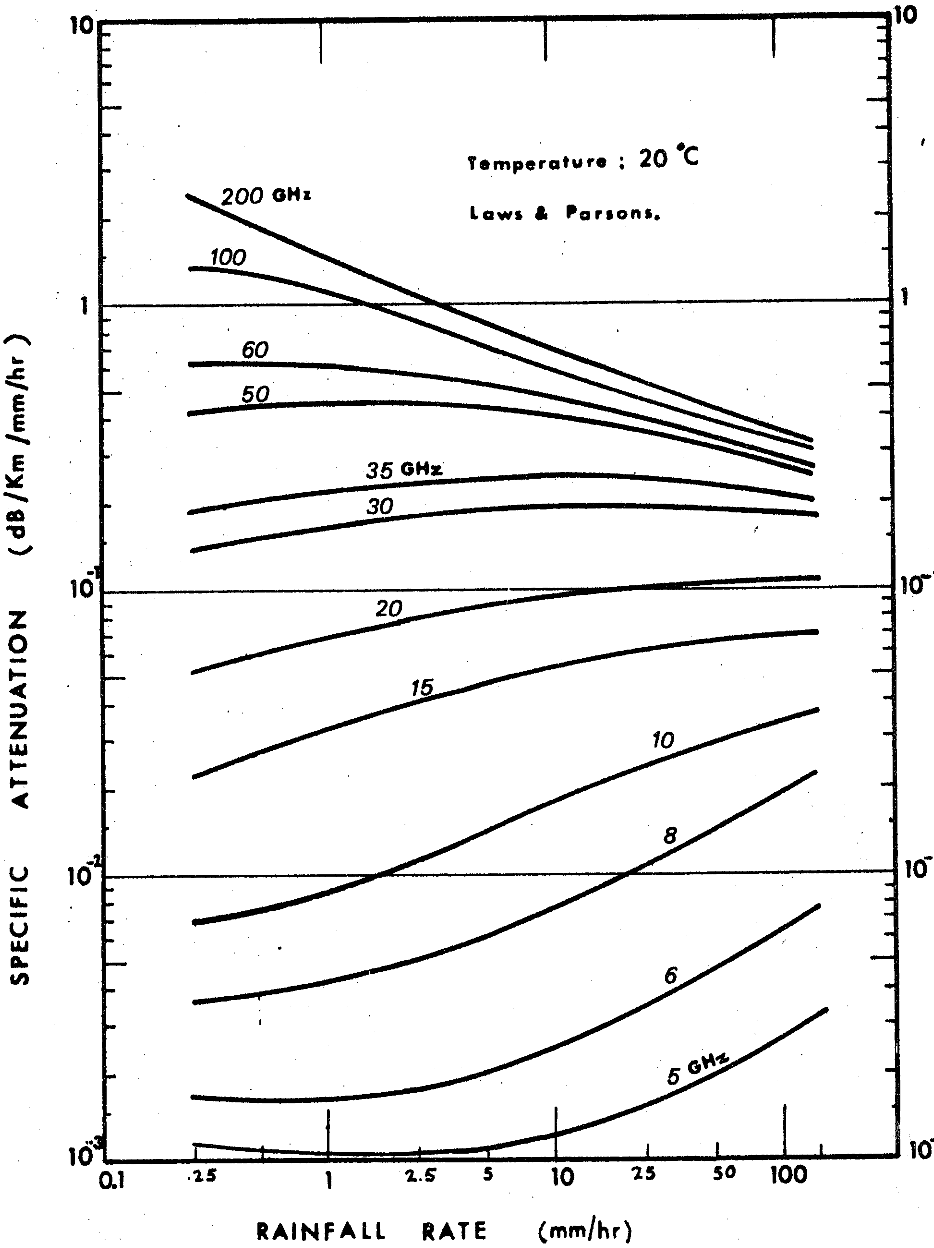

FIG. 21

THE SPECIFIC ATTENUATION COEFFICIENT AS A FUNCTION OF RAINFALL RATE

5.4. A linear regression model

As explained in the previous section, the attenuation coefficient is not proportional to the rainfall intensity. Many experimentalists, however, have derived empirical formulas of the form

$$\langle\gamma\rangle = K(\lambda)\ R_{av} \quad (\text{dB/Km}) \tag{5.3}$$

Their reason for choosing a linear regression model is that the uncertainty is such that a more sophisticated fit is not justified. The coefficient of proportionality $K(\lambda)$ should, however, compare with the specific attenuation coefficient given in Figure 21, which is strongly dependent on rainfall rate.

In order to compare their measurements with the theory, we have divided rainfall in two categories:

a. light rains, with intensity less than 10 mm/hr

b. intense rains, with intensity larges than 10 mm/hr.

The reason for this choice of 10 mm/hr will be explained in the next section. We can thus approximate the curves of Figure 21 by two horizontal segments, which define two specific attenuation coefficients independent of rainfall rate. These two coefficients are shown in Figure 22 (continuous lines) as a function of frequency. As expected, they intersect at about 37 GHz, where the specific attenuation was found to be independent of rainfall rate (Figure 21).

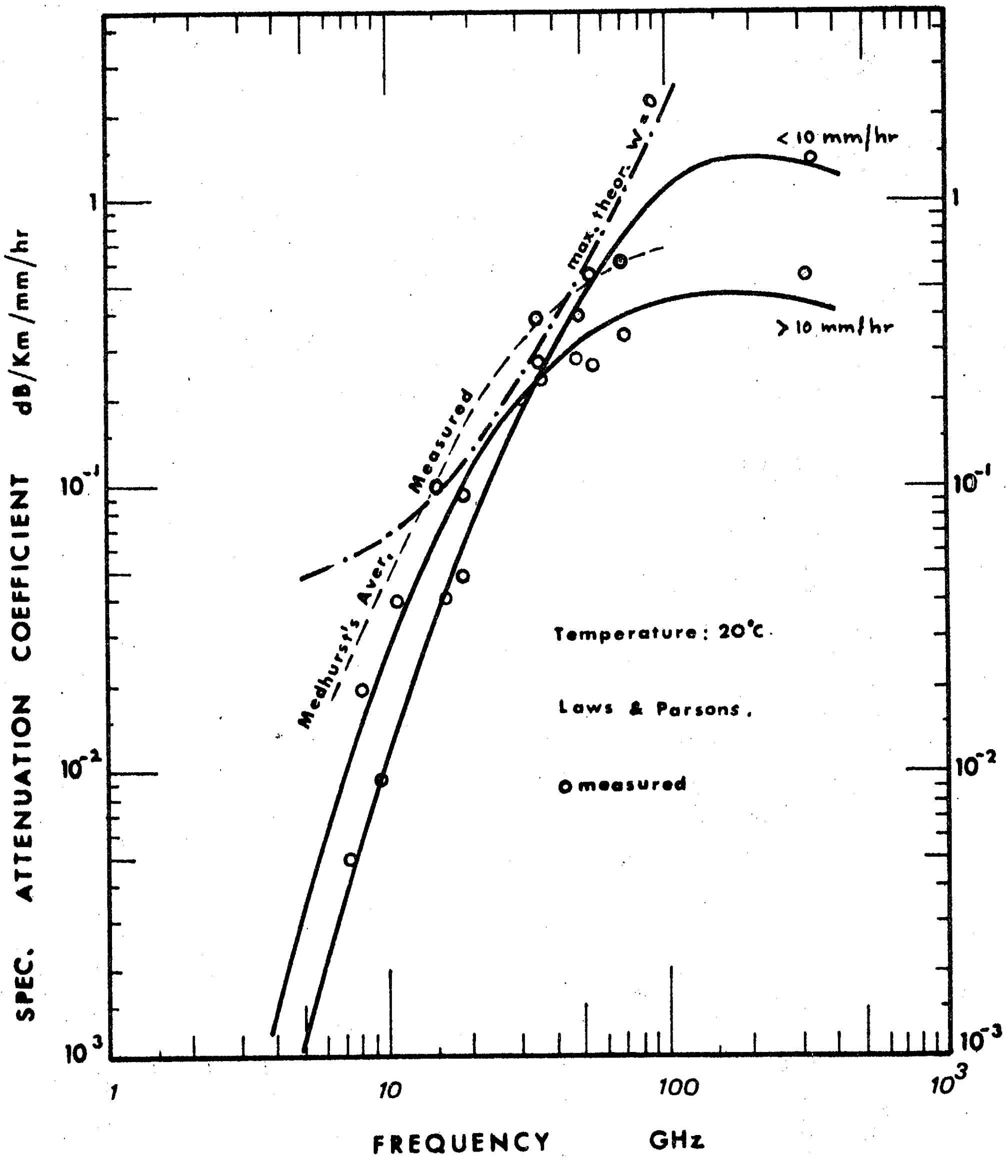

FIG. 22

LINEAR REGRESSION MODEL: THE SPECIFIC ATTENUATION COEFFICIENT. COMPARISON OF THEORY AND MEASUREMENTS

Experimental data points that have been published since Medhurst's survey (1965) are also shown in Figure 22. Unfortunately, most authors didn't make the distinction between light and intense rain, so that no strict comparison can be established. With the exception of two measurements, the one by Straiton (1970) at 15.3 GHz and the one by Roche (1970) at 35 GHz, the average measured specific attenuations do not exceed the theoretical maximum, calculated under the assumption of monodisperse rain (see section 5.8). This observation is somewhat different from the conclusion reached by Medhurst (1965) from the survey of measurements made before that year. The curve for average measured attenuation taken from his paper tends to be an upper bound to more recently obtained data.

Another important observation from Figure 22 is that for frequencies larger than about 37 GHz, light rains have a specific attenuation coefficient that is larger than that for intense rain. This is due to the important scattering effect of small drops, which reach the Mie region at those frequencies. For a similar reason, fog droplets will have a more severe effect than raindrops at still higher frequencies. For intense rain, a better linear fit would be

$$\langle\gamma\rangle = K'(\lambda)\ R_{av} + M(\lambda) \qquad \text{(5.3 bis)}$$

where $K'(\lambda)$, $M(\lambda)$ are constants to be determined.

(e.g., see Lammers 1967).

5.5. A logarithmic regression model

From a plot of the attenuation coefficient versus rainfall rate in a log-log graph, it appears that the curves can be fairly well approximated by two segments of straight lines, intersecting at a rainfall rate of approximately 10 mm/hr. This fact made us decide to distinguish between light and intense rain, with 10 mm/hr as a turning point, and to calculate values of the parameters in those two regions. These two straight lines are described by an equation of the form

$$\langle\gamma\rangle = A(f,T)\ R_{av}^{B(f,T)}\ (\mathrm{dB/Km}) \qquad (5.4)$$

The parameters A(f,20 °C) and B(f,20 °C) have been obtained in each domain from our previously calculated values for the attenuation coefficient, by a least-square error regression method; they are plotted in Figures 23 and 24 and also listed in Table II. The parameter B fixes the slope of the line whereas the parameter A controls its position in the plane. From Figure 23 it is apparent that the curvature of the attenuation curve versus rainfall rate is upward for frequencies between 1 and 8.5 GHz, then downward for frequencies up to 85 GHz, and then upward again. Figure 24 shows a slight variation of the parameter A for intense rains, compared to light rains.

FIG. 23

LOGARITHMIC REGRESSION MODEL: THE EXPONENT FACTOR. COMPARISON WITH MEASUREMENTS

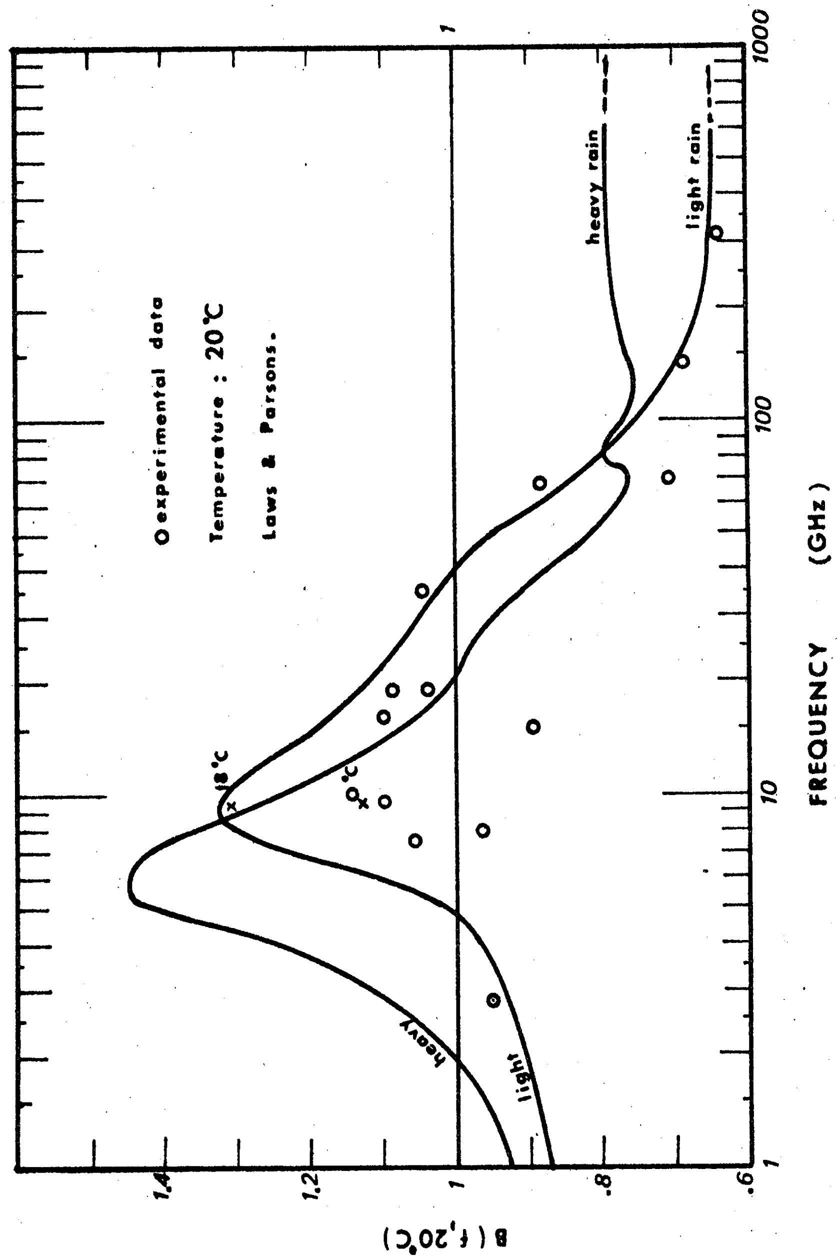

Again, experimental data published in the literature since Medhurst's survey (1965) are indicated by dots on both graphs. Only few of the authors adopting the logarithmic regression model made the distinction between light and intense rain, so that no systematic comparison can be made. It looks like a number of points in the 10 GHz region fall below the curves (Figure 23); however, computation of the parameter B at 9.4 GHz for two different temperatures (as indicated by crosses on the graph) shows the extreme sensitivity of this parameter to temperature. Since no temperature is indicated for the measured data, nothing definitive can be infered. The parameter A shows good agreement in general between calculated and measured values.

5.6. Temperature sensitivity

The temperature dependence of the refractive index of water makes the attenuation coefficient also sensitive to temperature. An investigation of this dependence in the case of a single water drop was carried out in Chapter 3 (section 3.10). In the case of uniform rain the curves of Figures 7 and 8 have to be weighted by the drop-size distribution. We obtain roughly the same tendency as in the single-drop case, where the drop diameter has to be replaced by the rainfall intensity. Figure 25 shows that, for a given temperature difference, very light rains are the most sensitive; this sensitivity

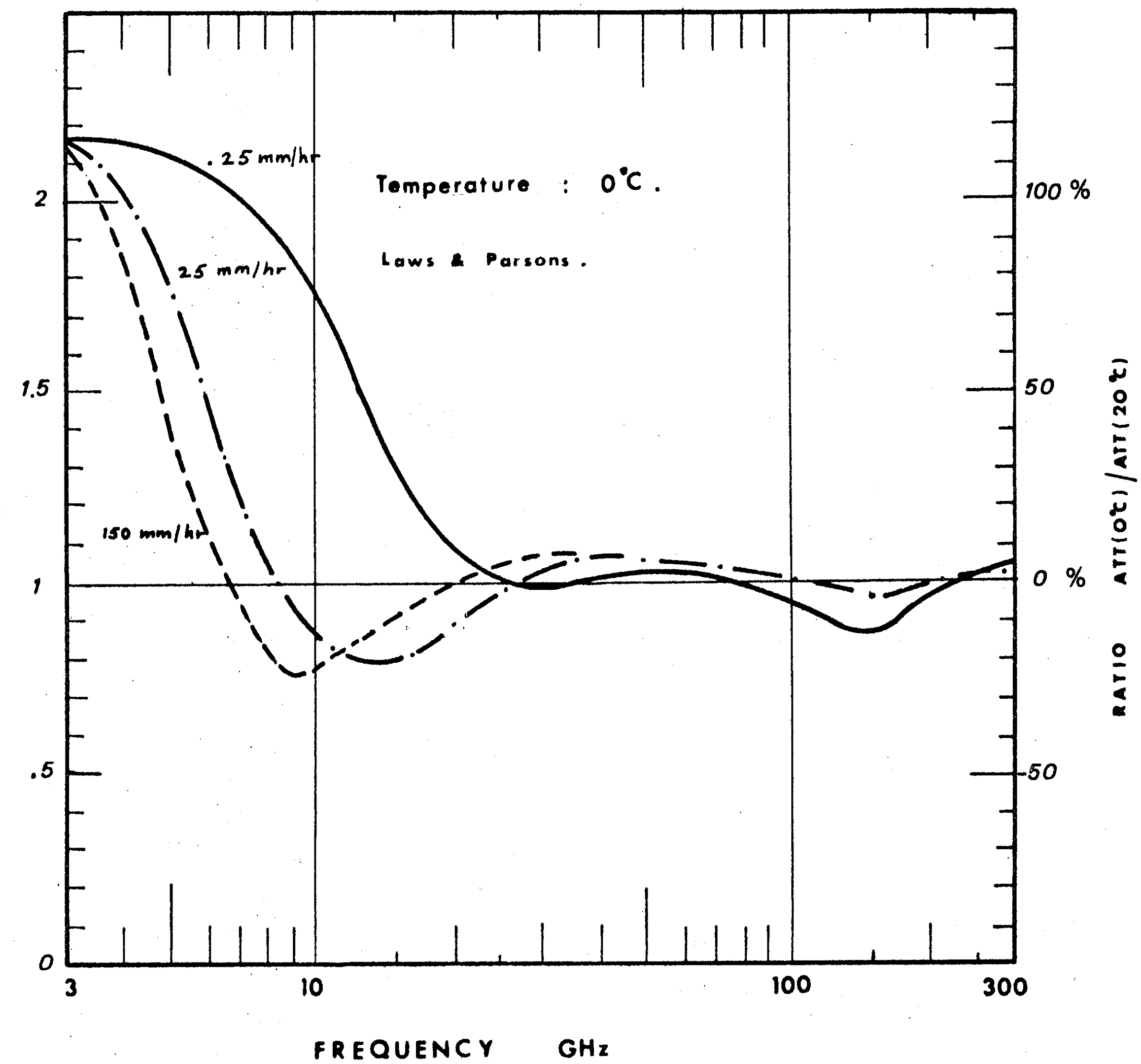

FIG. 25

THE RATIO OF THE AVERAGE ATTENUATION COEFFICIENT AT 0°C TO THE ATTENUATION COEFFICIENT AT 20°C, FOR VARIOUS RAINFALL RATES

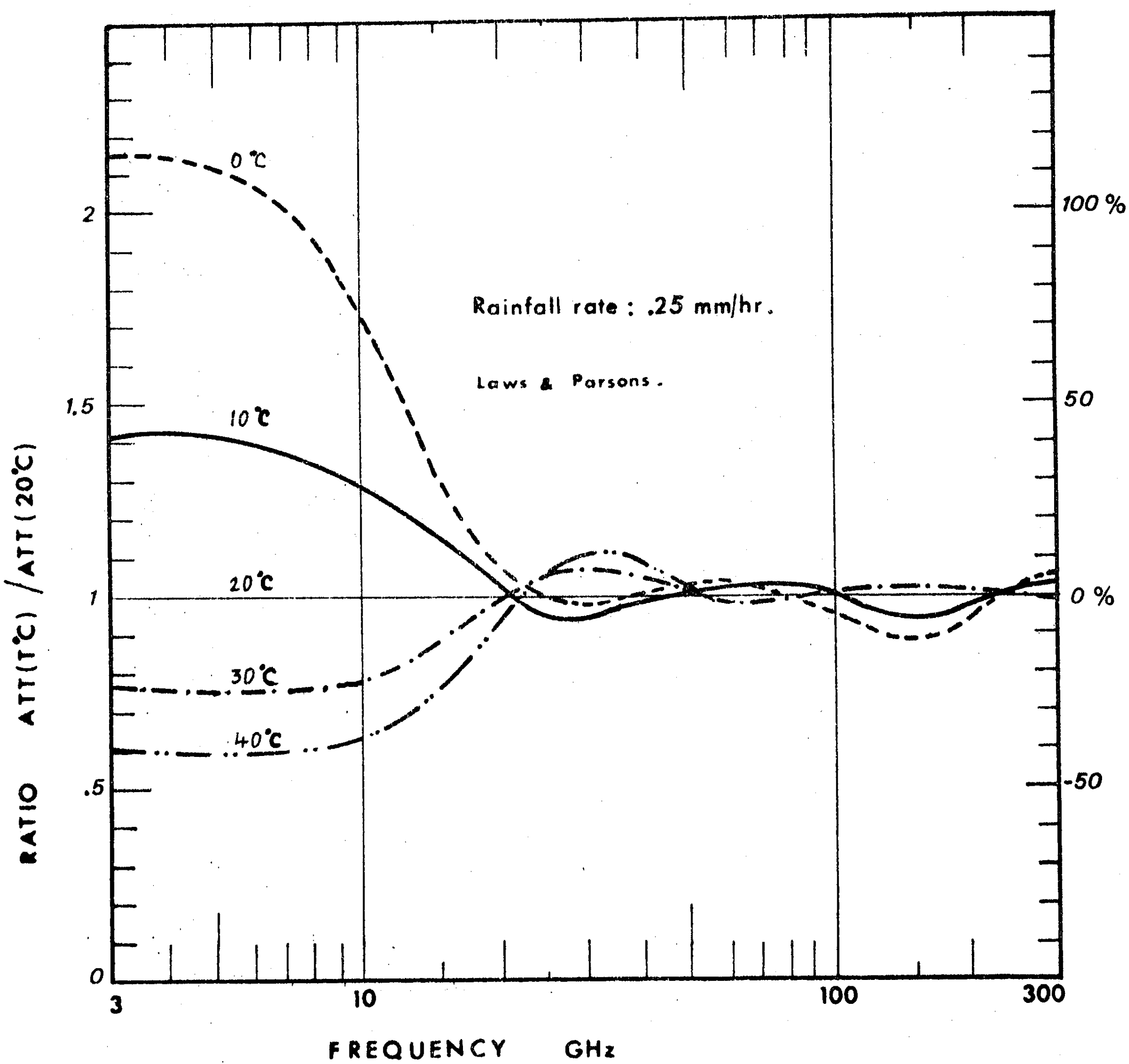

FIG. 26

THE RATIO OF THE ATTENUATION COEFFICIENT AT DIFFERENT TEMPERATURES FOR THE ATTENUATION COEFFICIENT AT 20°C, FOR A 0.25 MM/HR RAINFALL RATE may extend to frequencies as high as 20 GHz, whereas for more intense rains it may not be very critical for frequencies larger than 10 GHz. Figure 26 shows the correction factor for different temperatures at the most critical rainfall rate (0.25 mm/hr). The correction for temperatures less than 20 °C is larger than the one for temperatures in excess. For frequencies larger than 25 GHz the correction factor is within 15% at all temperatures. As a general rule we can state that the correction factor for temperature has a maximum importance for low frequencies at low rainfall rates; no very important temperature effects are to be expected in the millimeter wavelength range for all rainfall rates. The value of ± 15% can be adopted as an uncertainty bound in that case.

5.7. Sensitivity to drop-size distribution

A comparison between the attenuation coefficient obtained using the Laws and Parsons drop-size distribution and the one obtained using Marshall and Palmer's distribution (see Chapter 4) was carried out for a temperature of 20 °C. The ratio M.P./L.P. is plotted in Figure 27 for three different rainfall rates. An analysis of the results shows that the Marshall and Palmer distribution gives values of the attenuation coefficient that are usually larger than the one obtained from Laws and Parsons distribution; the largest difference occurs for low rainfall rates at high frequency.

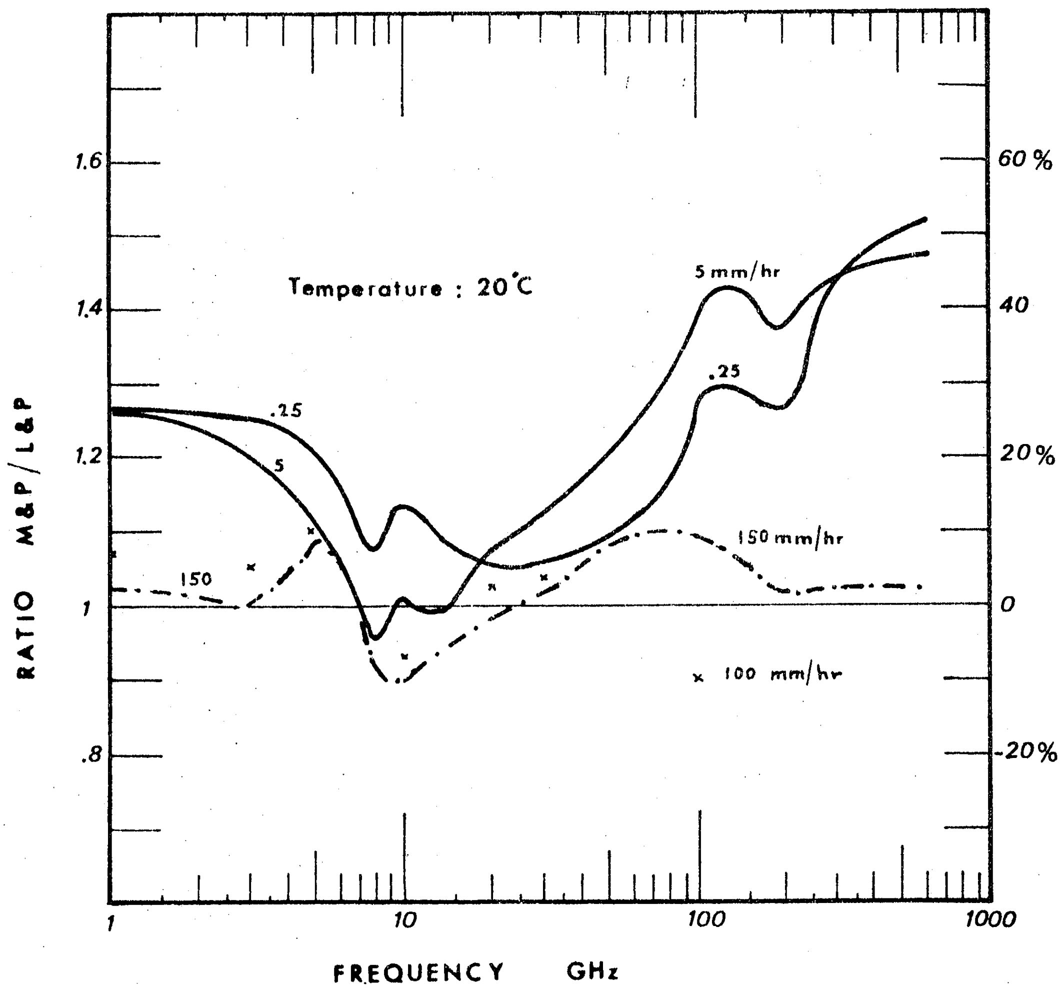

FIG. 27

THE RATIO OF THE AVERAGE ATTENUATION COEFFICIENT OBTAINED USING A MARSHALL-PALMER DROP-SIZE DISTRIBUTION TO THE ONE OBTAINED USING A LAWS AND PARSONS MODEL

This illustrates the fact that the Marshal and Palmer distribution exaggerates the number of small drops, which have their maximum contribution at low rainfall rates and high frequencies. A minimum sensitivity seems to be obtained for a wavelength of about 1 cm. This may be due to the fact that at this wavelength all rain drops have about the same influence on attenuation, independently of their diameter. It was also found that a shift of the drop size distribution towards smaller diameters, scaling the new distribution such as to get the same rainfall intensity, resulted in less attenuation for frequencies less than about 30 GHz and in a reversed trend at higher frequencies. It may be noticed here that at frequencies less than 15 GHz, the most important contribution comes from large drops, whereas drop diameters less than 2 mm play the important role at frequencies larger than 60 GHz. In between there is a zone of transition where almost all drop diameters play an equivalent role. On an average, the Marshall and Palmer distribution gives results that are larger than those obtained from the Laws and Parsons distribution; this is especially true at low rainfall rates. For intense rains the difference is contained within $\pm$ 10%.

5.8. A comparison of theory and measurements

In comparing the theory with experimental results we shall examine two points: a) compare the mean measured attenuation coefficient with the one obtained using Laws

Name	Year	Frequency [GHz]	Place
Crane	1966	1.29 to 94	New England
Lammers	1967	54	Germany
Blevis et al.	1967	8.39	Ottawa
		14.916	Canada
Weibel et al.	1967	90.5	New York
Harrold	1967	35	England
Semplak et al.	1969	18.5	New Jersey
Hogg et al.	1968	48.5	
		69.7	
Semplak	1970	30.9	New Jersey
Roche et al.	1970	34.47	Washington, DC
Straiton et al.	1970	15.3	Texas
Godard	1970	35	France
Babkin et al.	1970	314	Russia
Skerjanec et al.	1971	10	Mississippi
		14.43	
Ippolito	1971	15.3	North Carolina
		31.65	

TABLE III

List of new data sources for attenuation by rain since Medhurst's survey (1965).

and Parsons drop-size distribution (we arbitrarily selected a rainfall rate of 10 mm/hr for this comparison), b) compare the maximum measured attenuation coefficient with the one obtained for a monodisperse rain.

Figure 28 is a plot of the attenuation coefficient as a function of frequency at a rainfall intensity of 10 mm/hr. The tendency for the Marshall and Palmer distribution to give larger values of the attenuation coefficient at frequencies larger than 30 GHz is evidenced again from this plot. Average measured values of the attenuation coefficient at 10 mm/hr, taken from the literature published after 1965, are indicated by white dots on the same figure. Black dots indicate values calculated at 10 mm/hr from measurements at another rainfall rate. A list of the data sources for experimental values of the attenuation coefficient is given in Table III. Measurements before 1965 are summarized in the average measured curve from Medhurst's survey (1965); this curve is also plotted in Figure 28.

A first conclusion from this plot is that Medhurst's average measured curve is not a good fit for the more recent experimental data. With the exception of two or three points, it lies constantly above the measured data. A possible explanation for this tendency towards exaggeration is the considerable weight given by Medhurst to the experiment at 24 GHz by Anderson et al; also Medhurst's curve was derived for the specific attenuation

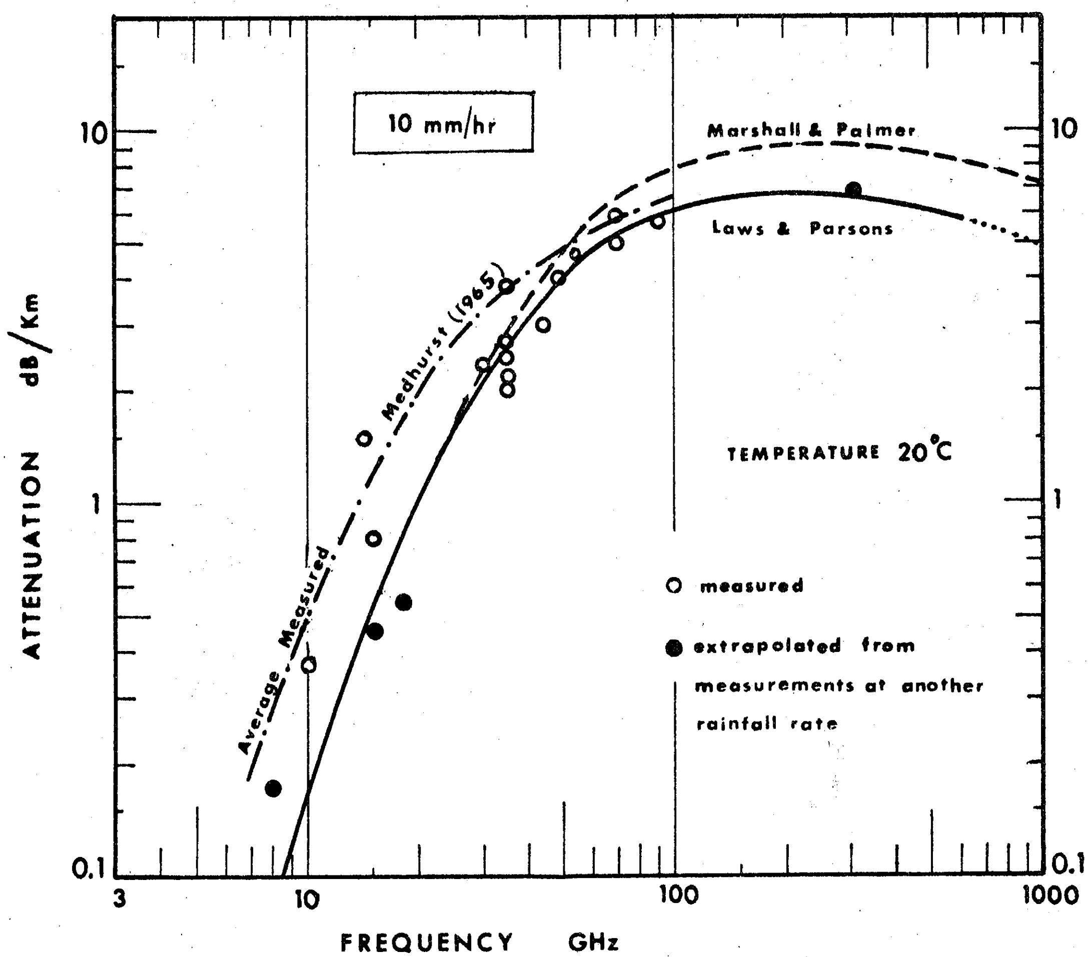

FIG. 28

THE AVERAGE ATTENUATION COEFFICIENT AS A FUNCTION OF FREQUENCY FOR A 10 MM/HR RAINFALL RATE. COMPARISON OF THEORY WITH MEASUREMENTS.

coefficient (in dB/Km/mm/hr) and not at 10 mm/hr. This tendency towards exaggeration may thus be due to errors introduced by the linear regression model used and also to the fact that the average regression curve is different from that obtained averaging upper and lower bound. But it is evident from Figure 22 that his curve for specific attenuation coefficient also lies above most of the data points.

Another conclusion is that the Laws and Parsons distribution seems to provide the best fit to experimental data, at least for a rainfall rate of 10 mm/hr. This doesn't seem to be the case at lower rainfall rates, where a general tendency for the points to lie above the Laws and Parsons average curve has been reported by almost all experimentalists. Two explanations may account for this fact: either the meteorological data are not suitably interpreted, due to the imprecision of the instruments at low rainfall rates and turbulent effects, or the Laws and Parsons distribution underestimates the number of small drops at low values of the precipitation rate. Modern drop-size measurement methods seem to be more sensitive to small drops than the flour-pellet method, and new measurements of the drop-size distribution at low rainfall rates are suggested in order to solve this undertemination.

It was shown in section 5.4 that, with the exception of two cases, the average measured attenuation coefficient was less than a theoretical maximum calculated under the assumption of monodisperse rain. Medhurst (1965) introduced this upper-bound by considering an artificial rain consisting of drops having all the same diameter (monodisperse) and in such a number as to give a 1 mm/hr intensity. The curves for the specific attenuation obtained this way, at a given frequency, show a maximum and a minimum which occur for two well-defined drop diameters. It seems evident that the attenuation for actual rain, consisting of several diameters, cannot be larger than if it were composed exclusively of drops giving the maximum attenuation.

These attenuation coefficients for monodisperse rain have been recalculated, using our program, and show good agreement with Medhurst's data. Both theoretical maximum and minimum as a function of frequency are shown in Figure 29; as expected the average attenuation coefficient for actual rain, using the Laws and Parsons distribution, lies within those boundaries. Many experimentalists, however, have measured points that lie above this theoretical maximum, even if their averages do not. The maximum measured values reported by Medhurst are shown in Figure 29, and the curve is seen to lie well above the theoretical maximum. In order to explain this fact, we have to recall an assumption that was introduced when relating the point rainfall rate to the average drop-size distribution, namely that the uncertainty on the vertical com-

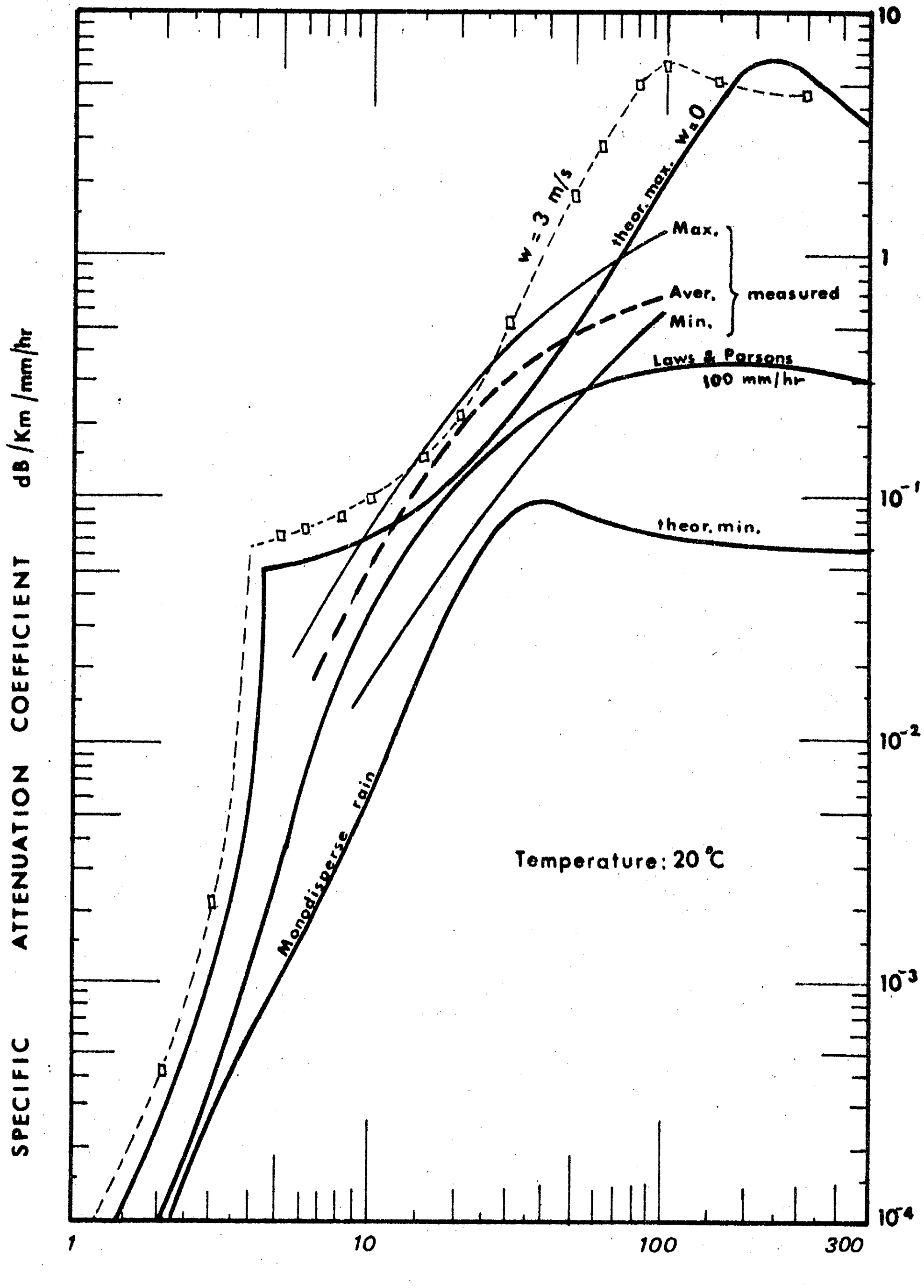

FIG. 29

THE THEORETICAL MAXIMUM AND MINIMUM OF THE SPECIFIC ATTENUATION COEFFICIENT, FOR MONODISPERSE RAIN. EFFECT OF THE UNCERTAINTY OF THE DROP VELOCITY.

distribution for calculating the average attenuation coefficient still remains to be demonstrated; this is especially true for low rainfall intensities, for which several experimentalists have reported a tendency for measured data to exceed the theoretical value: Godard (1970), Blevis et al. (1967), Straiton et al. (1970), Skerjanec et al. (1971). Also the use of an average rainfall rate over the path for predicting average attenuation still needs experimental evidence.

Experiments involving more careful handling of the meteorological data still need to be carried out. Alternatively, one way of avoiding meteorological measurements consists of carrying measurements at two different frequencies along the same path. One can then compare the experimentally measured ratio of the two attenuations with the one predicted by the theory. Such results for New Jersey rain have recently been published by Semplak (1971) and show that the Laws and Parsons distribution provides the best fit to the average measured data. Similar experiments should be carried on for different climates before definitive conclusions can be drawn.

When carrying on experiments where the path-averaged rainfall rate is measured, it is suggested that the comparison be established in the specific attenuation versus rainfall rate plane (see Figure 21) rather than in the $(\langle\beta\rangle, R_{av})$ plane. This would take care of the variation of the specific attenuation coefficient with rainfall intensity.

CHAPTER 6

THE DISPERSIVE PROPERTIES OF RAIN

6.1. Introduction

Rain not only causes attenuation of the coherent signal, but also modifies its velocity of propagation, as compared to free space conditions. This variation in propagation time would cause no harm to the signal if it would be the same for all frequency components. In rain, however, the phase velocity is frequency dependent, as is characteristic of a dispersive medium, and causes delay distortion.

Most communication systems are not sensitive to the absolute value of the velocity of propagation. It is the rate of change with frequency that is relevant in causing delay distortion. The bandwidth limitations imposed on a transmission system by the dispersive properties of rain cannot be established in general; it largely depends on the type of transmission system that is used (coherent, non-coherent) and also on the choice of modulation techniques. In the EHF band, in order to take full advantage of the bandwidth capabilities, the baseband signal is very likely to be in a digital form. But, even in that case, several modulation techniques are still possible.

The only known published study of this problem is the one by Crane (1967); the author investigated the theoretical value for pulse broadening after propagation through intense rain, at four different frequencies 4, 8, 15.5, and 34.86 GHz. Setzer (1971) published tabulated data for the excess phase at different rainfall rates and frequencies. Unfortunately, the published values show unexplained discontinuities. In the following treatment, we shall attempt to determine bandwidth limitations due to rain by a study of the complex transfer function in the frequency domain (rather than in the time domain like Crane did). This approach implies linearity in the scattering process, so that the effect on a signal is equal to the sum of the effects on its spectral components.

6.2. The dispersive phase constant

The complex transfer function for a rainy atmosphere was found in Chapter 4. For a monochromatic sinusoidal signal propagating through such a medium, the total average phase delay, per unit path length, is given by

$$\langle\Phi(\lambda\ ,R_{av})\rangle = k_o(1 + \langle m_e'(\lambda,R_{av})\rangle\ )\ \ (\text{rad/Km}) \tag{6.1}$$

where k_o is the free space wave number (Km^{-1}) and

$\langle m_e'(\lambda,R_{av})\rangle$ is given by equation 4.10 and is plotted in Figure 16.

Since the real part of the equivalent refractive index is very small compared to one (10^{-6}) and since the

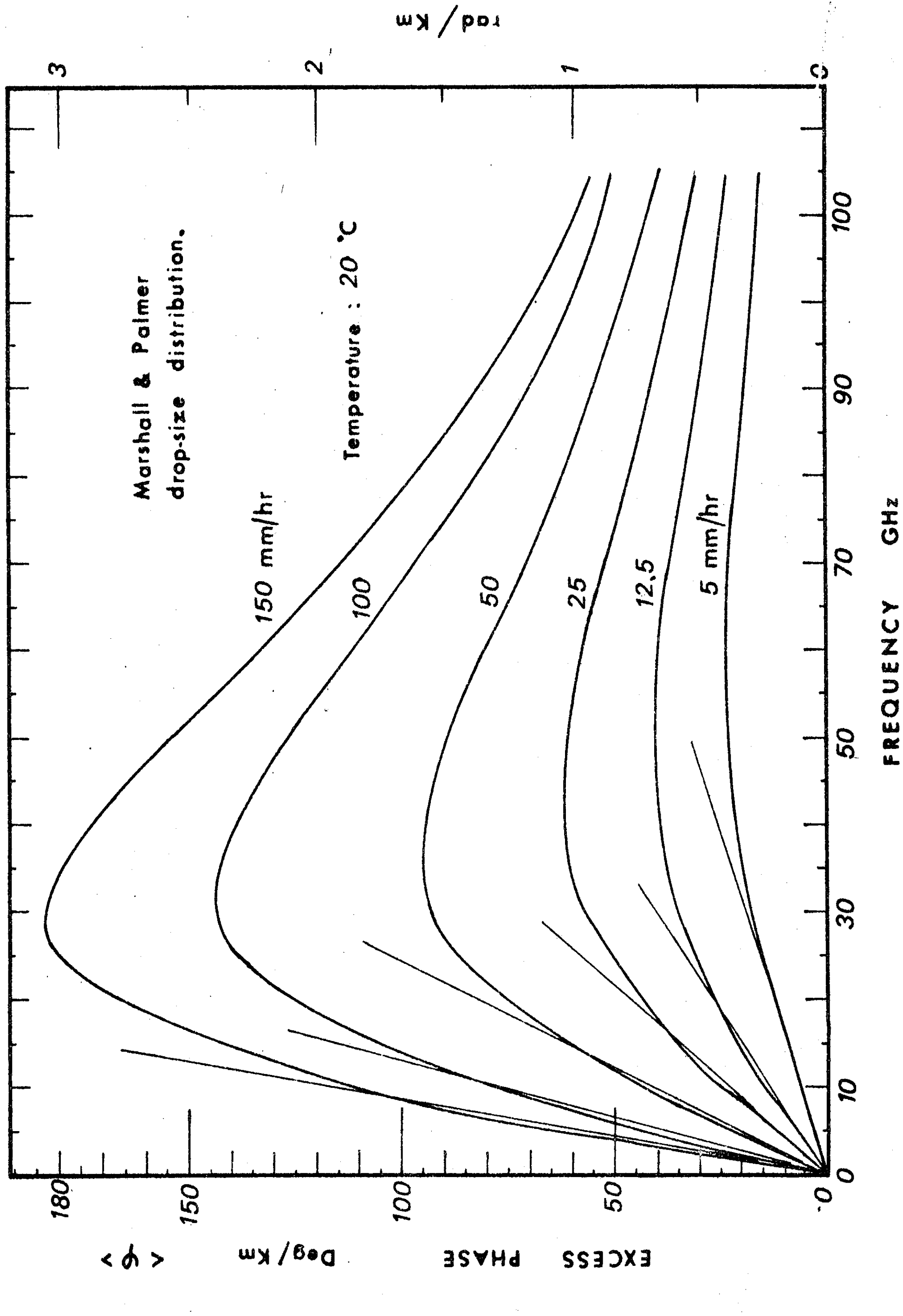

FIG. 30

THE AVERAGE DISPERSIVE PHASE CONSTANT, FOR DIFFERENT RAINFALL RATES.

second term in (6.1) is the only one responsible for dispersion, it seems convenient to analyze it separately. We define the dispersive phase constant as

$$<\varphi(\lambda,R_{av})> = k_o <m_e'(\lambda,R_{av})> \tag{6.2}$$

which is expressed in rad/km or in deg/km according to the definition adopted for k_o.

Values of $<\varphi(\lambda,R_{av})>$ were easily obtained from our computer program; several drop-size distribution models were even tried. The Marshall-Palmer model gave smoother results than others models in the far-end of the millimeter wavelengths range, and therefore was preferred to other models, although it is known to exaggerate the number of small drops. The advantage of the Marshall-Palmer model over other models is partly due to the fact that we can use a Gaussian two points integration method, which gives better accuracy in the region where the integrand function is changing sign.

Figure 30 is a plot of the excess phase delay versus frequency, for different rainfall rates. It shows that a maximum in the absolute delay is reached in the 30 to 50 GHz range, depending on precipitation intensity. At 30 GHz the delay after propagation through one kilometer of intense rain can reach values as large as half a wavelength. But it takes about ten kilometers at low rainfall rates to bring forth the same result. As it appears from Figure 15 (Chapter 4), the equivalent refractive index becomes negative at higher frequencies, thus leading to a phase advance as compared to free space propagation. This is explained by the fact that the drops having a major contribution at those frequencies yield a phase lag of more than 180° for the scattered wave (see Section 4.7, Figure 17).

The specific dispersive phase constant in deg/km/mm/hr is defined as the ratio of the dispersive phase constant to the rainfall rate that caused it. This ratio is plotted in Figure 31 a and b versus R_{av}, for different frequencies. This plot shows that the dispersive phase constant is not a linear function of rainfall rate. This non-linearity is especially marked in the lower millimeter wavelength range, where the ratio can vary over several orders of magnitude.

The sensitivity of the dispersive phase constant to temperature was also investigated. For frequencies less than 10 GHz, it showed less than $\pm$ 3% variation for all temperatures and rainfall rates. In the 10 to 150 GHz band, the variations were bounded by $\pm$ 10%, whereas at higher frequencies variations of several hundred percent were noted. The extreme variations occurred for a temperature of 0 °C (as referred to 20 °C) at moderate rainfall rates (5 - 25 mm/hr). Thus, at the opposite of the attenuation coefficient, the phase constant is rather insensitive to temperature at low

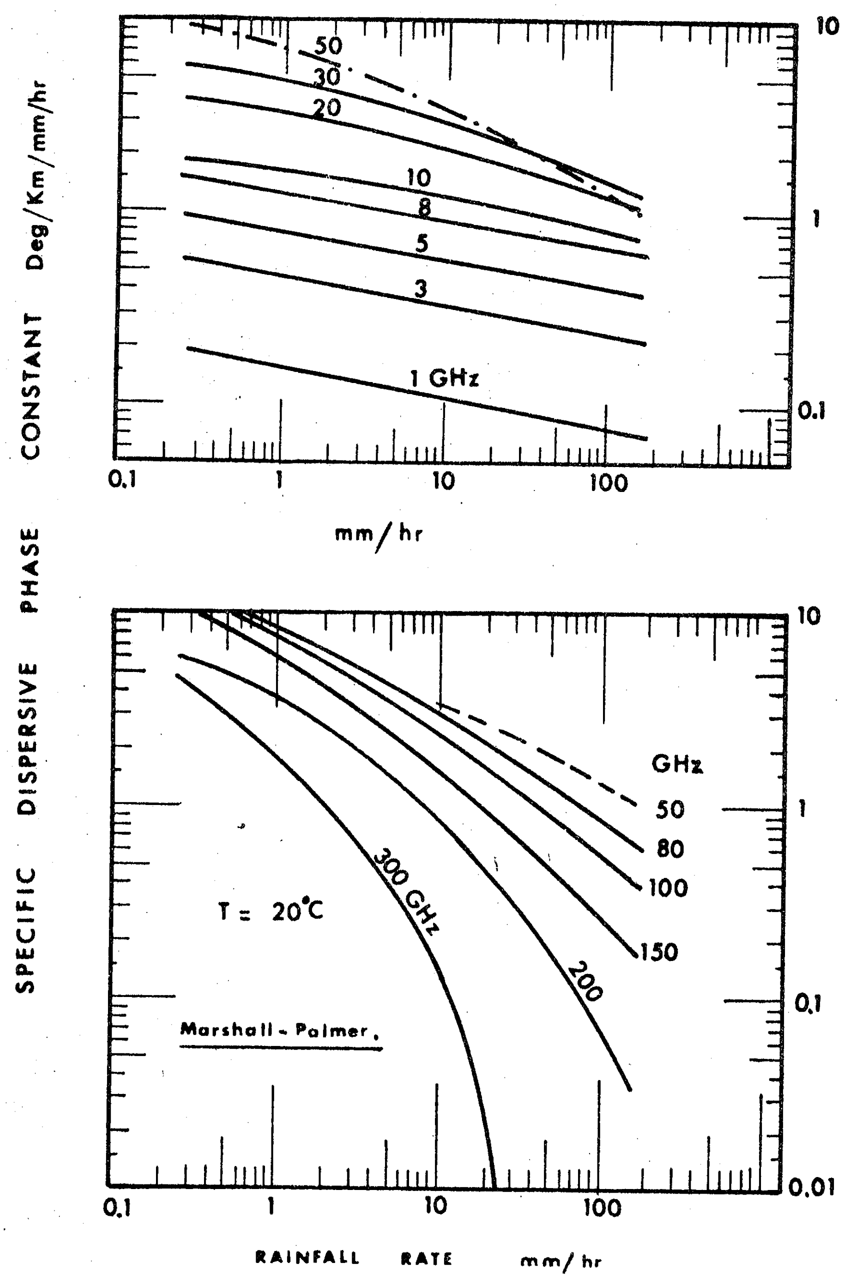

FIG. 31

THE SPECIFIC DISPERSIVE PHASE CONSTANT AS A FUNCTION OF RAINFALL RATE

a. centimeter

wavelengths

b. millimeter

frequencies and very sensitive at short millimeter wavelengths. It may be pointed out here that in both cases, however, the maximum sensitivity to temperature occurs in regions where the absolute value of the attenuation or phase constant are very low and almost negligible.

The sensitivity of the dispersive phase constant to drop-size distribution may be tested by comparing the Marshall-Palmer distribution to the Laws and Parsons distribution. The results plotted in Figure 32 as the ratio of the two phase constants, show the tendency for the M.P. distribution to predict more phase delay than the L.P. distribution. However, it is remarkable that, for frequencies below 40 GHz, this difference is quite independent of frequency and is just a function of rainfall intensity, low rainfall rates showing the largest difference. At higher frequencies where the effects of small drops are important, the differences become very large; it is interesting to note the tendency towards larger phase shifts at low and moderate rainfall rates and a reverse trend at intense rains. The 50 mm/hr curve seems rather undecided between those two extremes and, after some hesitations, finally decides for the intense rain trend.

Unlike the attenuation coefficient for which the drop diameter for maximum influence varied from large values at cm wavelengths to small values in the millimeter band, small drops always cause the largest phase

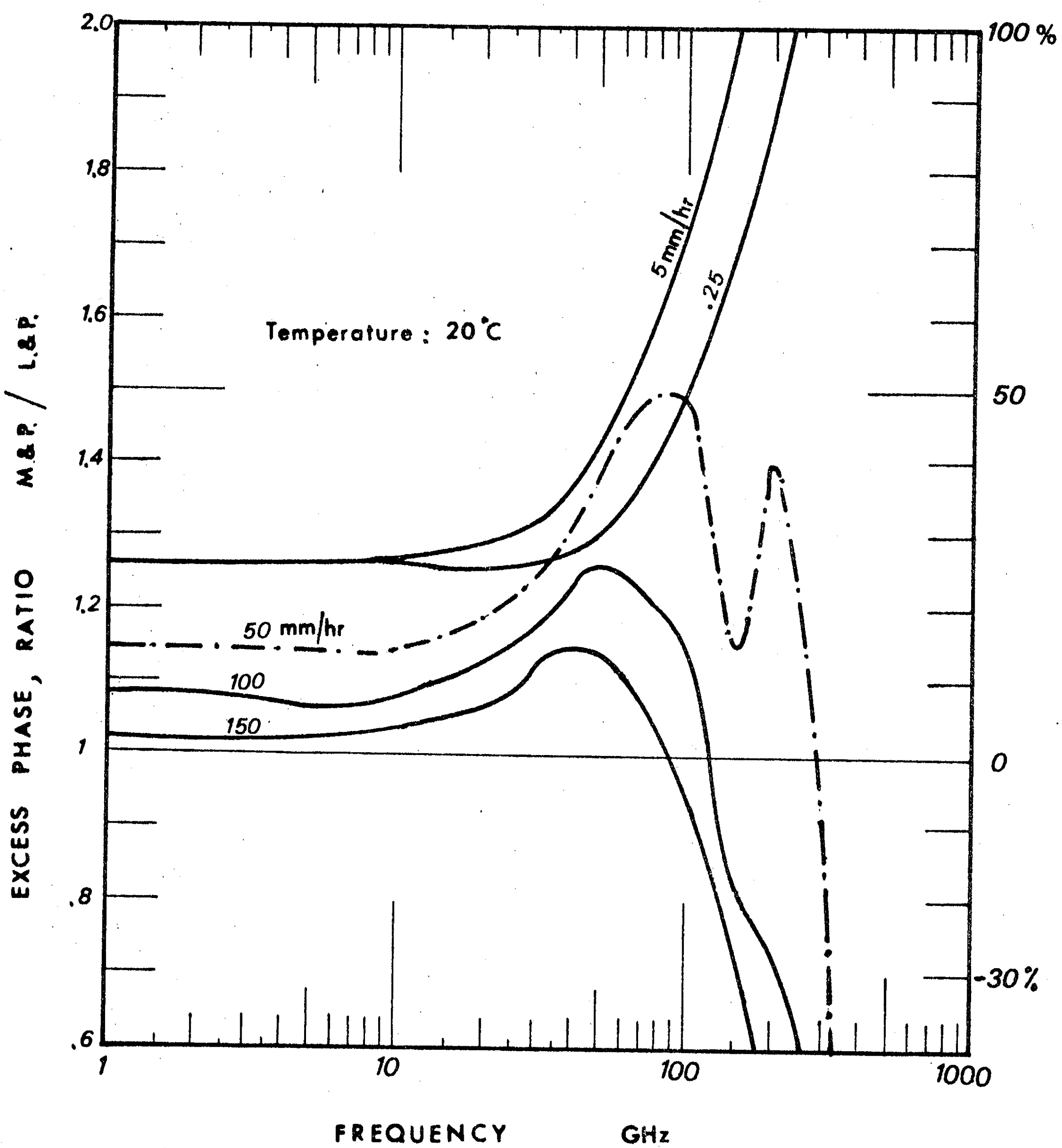

FIG. 32

SENSITIVITY OF THE DISPERSIVE PHASE CONSTANT TO THE DROP-SIZE DISTRIBUTION. RATIO MARSHALL-PALMER TO LAWS AND PARSONS shifts. This appeared from a study of monodisperse rain in order to evaluate upper- and lower-bounds for the specific dispersive phase constant. The upper-bound is thus very sensitive to the minimum drop diameter chosen in the drop-size distribution function. In Figure 33 two such upper bounds are shown, one assuming a minimum drop diameter of 0.5 mm and the other for 0.25 mm. The lower-bound becomes negative at frequencies larger than 60 GHz. Three curves for different rainfall rates, assuming a Laws and Parsons drop-size distribution, are also shown in Figure 33. They all lie well within the boundaries.

6.3. <u>Delay distortion caused by rain</u>

In the previous sections, we have discussed extensively the absolute value of the dispersive phase constant. However, the absolute value itself is of little importance in determining the amount of distortion. The rate of change of the value of the phase constant with frequency is the parameter that fixes the amount of delay distortion.

A linear variation of the phase constant with frequency causes a constant time-delay for all frequency components of the signal and hence no distortion. This is not the case, however, for a rainy atmosphere, as can be seen from Figure 30, except for the longest centimeter wavelengths. A zero excess phase constant is yet admissible and this is nearly the case for the

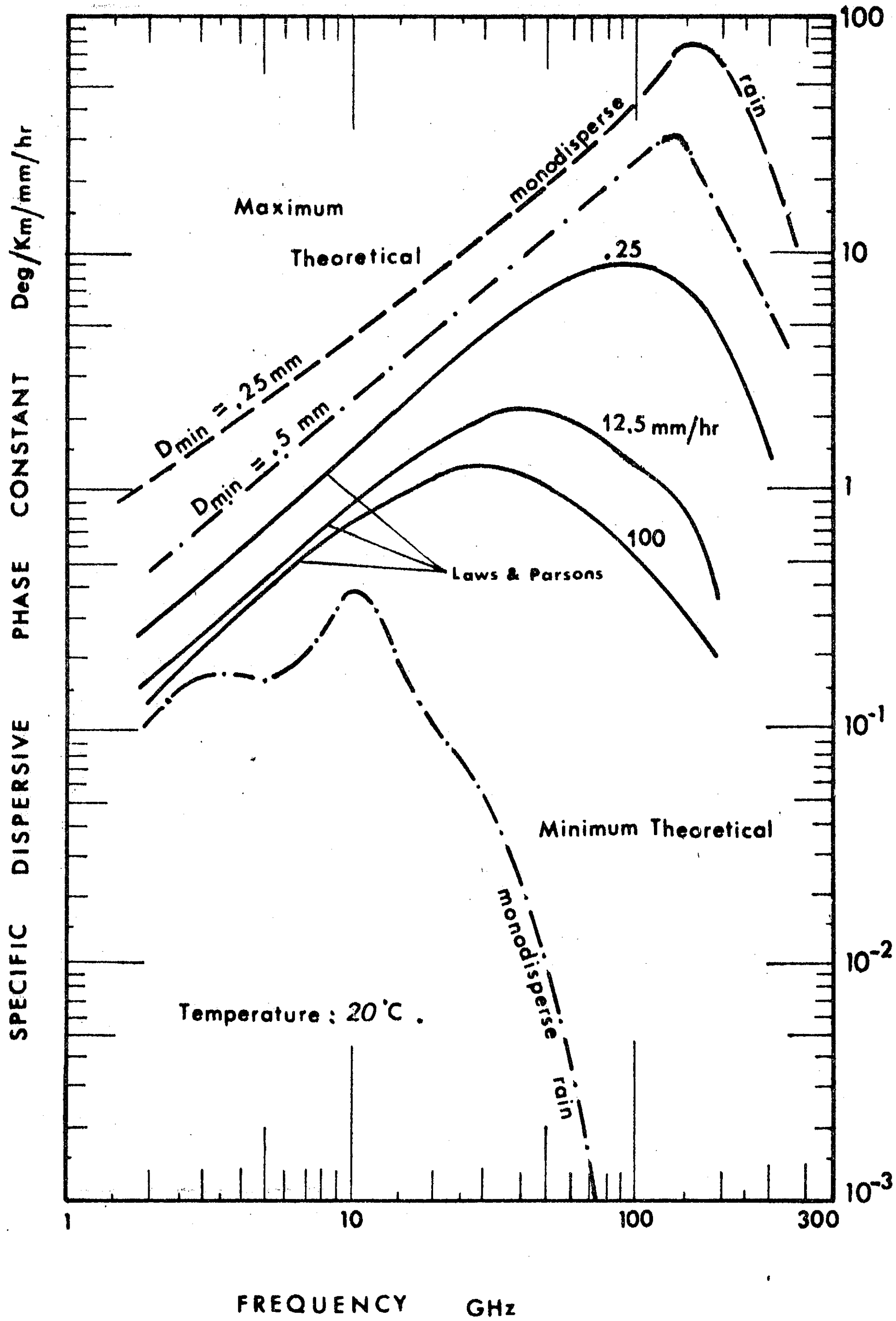

FIG. 33

THEORETICAL MAXIMUM AND MINIMUM OF THE SPECIFIC DISPERSIVE PHASE CONSTANT, UNDER THE ASSUMPTION OF MONODISPERSE RAIN shortest millimeter wavelengths. For intermediate wavelengths, that is in the region from 5 to 100 GHz, the excess propagation time will be different for all frequency components. They will be scrambled in time and delay distortion will result.

In the case of linear modulations techniques, where all the frequency components are usually concentrated in a relatively narrow band around the carrier frequency, the delay distortion may be characterized in terms of envelope delay, which is defined as the reciprocal of the group velocity

$$\tau_e = \frac{1}{v_g} = \frac{1}{c} + \frac{d\langle\varphi\rangle}{d\omega} \quad \text{(sec/km)} \qquad (6.3)$$

or

$$\tau_e = \tau_o + \Delta\tau(\omega) \qquad (6.4)$$

where τ_o is a constant, approximately equal to 3 μsec/km and $\Delta\tau(\omega)$ is the relative envelope delay time (picosec/km) which is a function of frequency ($\omega = 2\pi f$).

Only the relative envelope delay is of importance in determining the delay distortion. In a region where $\Delta\tau(\omega)$ as a function of frequency is relatively flat, no significance distortion in the envelope of the signal will result.

It must be pointed out here that this method of characterizing the delay distortion is only valid for narrow-band modulation systems and slightly dispersive stronger variations at high rainfall rates, whereas in the millimeter wavelengths region the theory is no longer valid.

For non-linear modulation techniques, which are more likely to be used at those frequencies, the approach chosen consists in studying the carrier delay time as a function of frequency. This time delay is given by

$$t_c = \frac{k_o(1 + \langle m_e' \rangle)}{\omega} = \frac{1}{c} + \frac{\langle m_e' \rangle}{c} \qquad (6.5)$$

or

$$t_c = \tau_o + \Delta t(\omega) \qquad \text{(sec/Km)} \qquad (6.6)$$

where $\Delta t(\omega)$ represents the relative carrier delay time (picosec/Km) for a purely sinusoidal signal .

The envelope and carrier time delays are related by

$$\Delta\tau(\omega) = \Delta t(\omega) + \frac{2\pi}{\lambda_o} \frac{d\langle m_e' \rangle}{d\omega} \qquad (6.7)$$

emphasizing the fact that the excess propagation time for the envelope of the signal is due to first order non-linearities in the variation of the equivalent refractive index with frequency (see Figure 16).

As can be seen from equations (6.5) and (6.6), the relative carrier delay time is proportional to $\langle m_e' \rangle$ and thus must show the same behavior versus frequency as the curves of Figure 16. However, this delay time is presented here again (see Figure 35) for the case of a

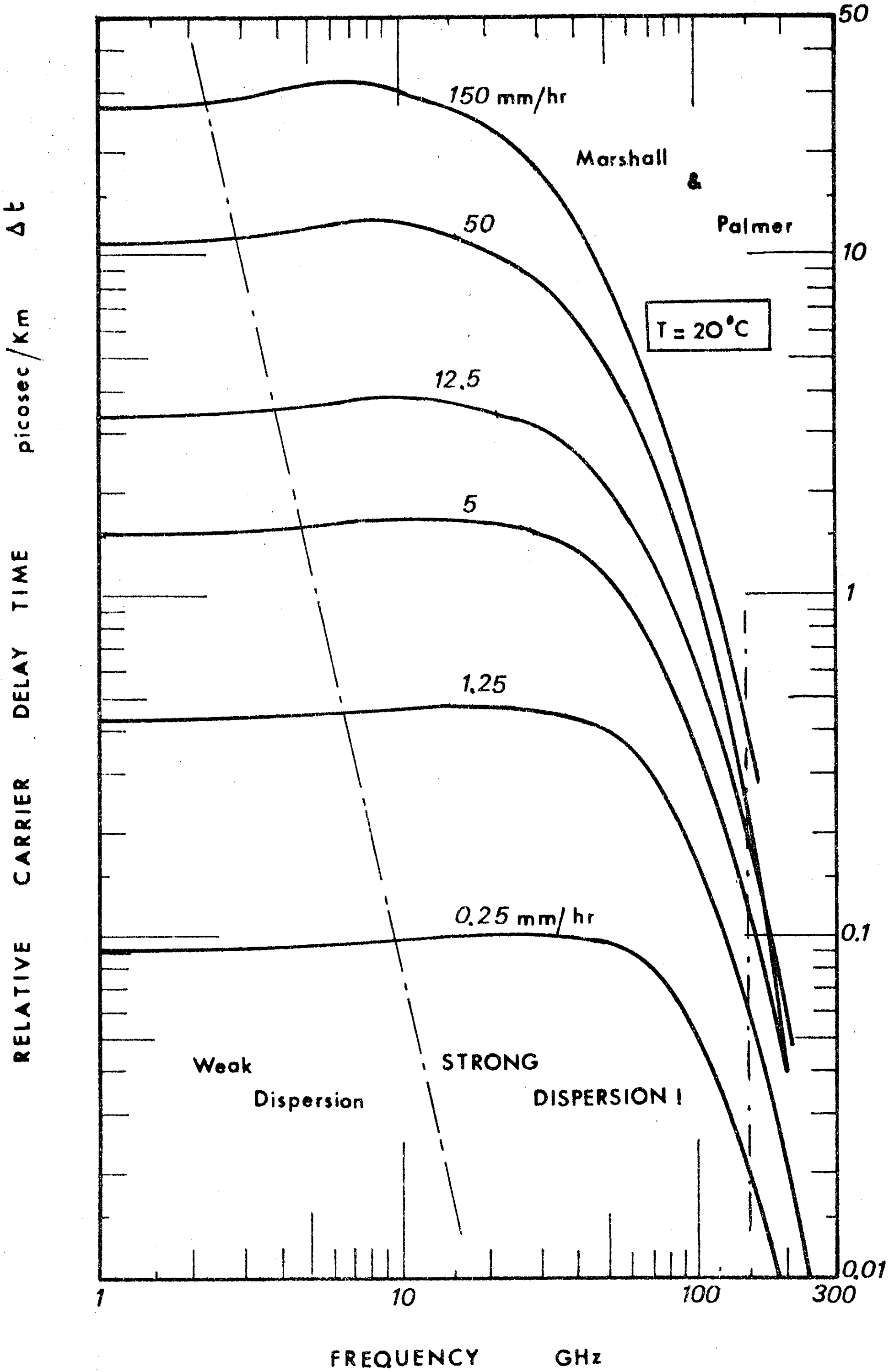

FIG. 35

THE RELATIVE CARRIER DELAY TIME,
FOR DIFFERENT RAINFALL RATES

Marshall-Palmer drop-size distribution. The dashed curve on the same figure separtes the regions of weak and strong dispersion. It also indicates their extent in the frequency domain as a function of rainfall rate. There is also a region of weak dispersion at frequencies larger than 150 GHz.

The relative carrier delay itself is not very important in calculating the signal distortion due to phase delays. When using frequency keyed transmissions, however, the maximum transmission rate can be found from these curves, looking for the condition that the pulses do not get scrambled in time. Since these delays are very small, practically the path lengths that would produce pulse overlapping are much larger than those usable at millimeter wavelengths. This may not be the case if frequencies are chosen far apart, but this situation is not practical either.

Of greater significance is the rate of change of the carrier delay-time with frequency, given by

$$D(f) = \frac{d(\Delta t(\omega))}{d\omega} \qquad (6.7)$$

This function is shown in Figure 36 for intense rainfall rates. The curves show a zone of maximum sensitivity at frequencies ranging from 4 - 6 GHz, depending on the rainfall intensity, and another zone of strong frequency dependence ranging from about 10 to 40 GHz, where the slope becomes negative. Practically rain below 25 mm/hr intensity will produce only a negligible

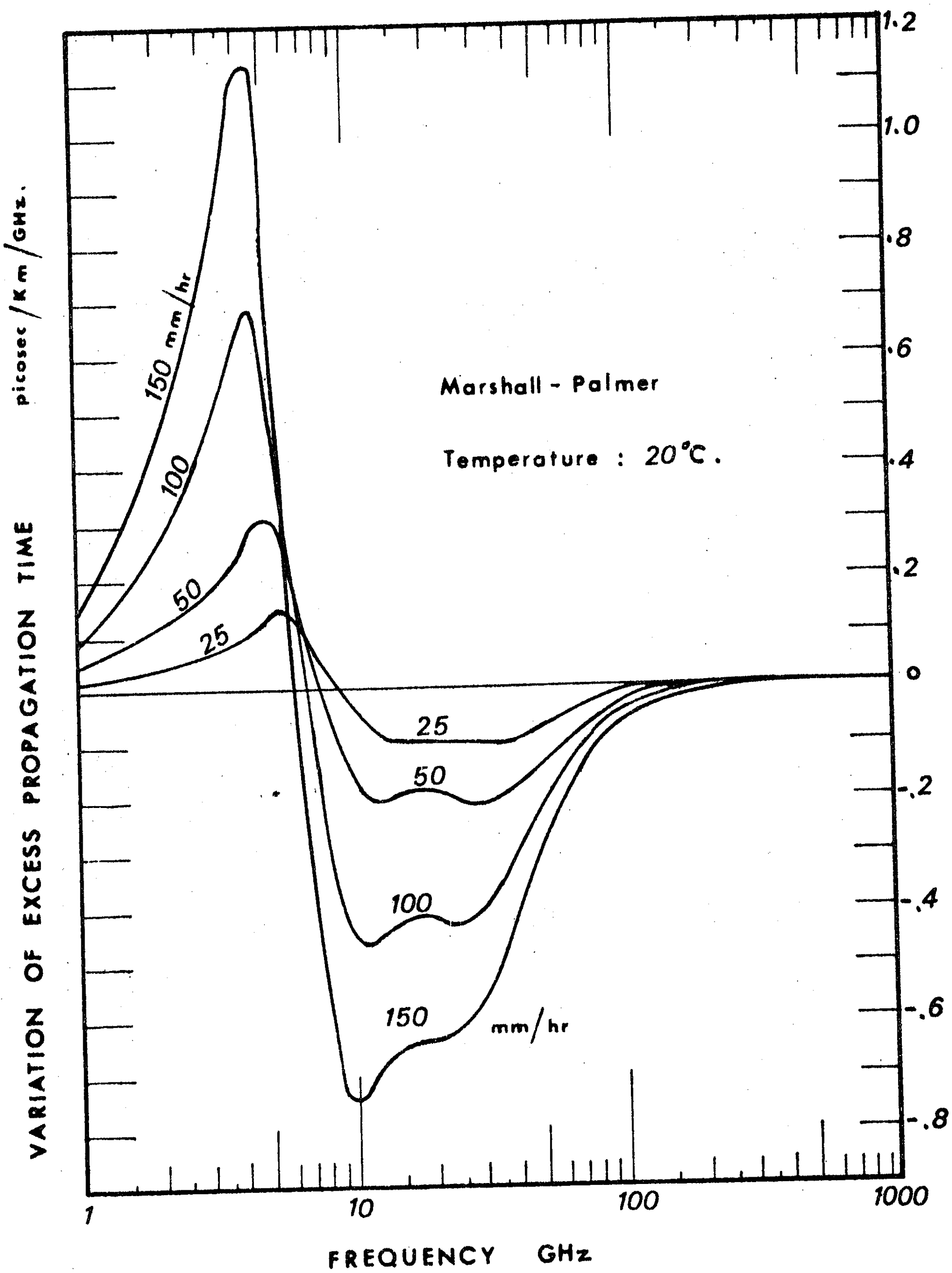

FIG. 36

THE SLOPE OF THE RELATIVE CARRIER DELAY TIME

CHAPTER 7

CONCLUSION

This study deals mainly with the propagation of a plane electromagnetic wave in a rainy atmosphere. A simple model, analogous to the transfer function concept in system analysis, is shown to describe adequately the statistical average influence of rain on the phase and amplitude of a coherent wave. The limits within which this model can be used to describe incoherent propagation through rain are also investigated.

From our survey of the 1 to 600 GHz spectrum range, the main characteristics of the interaction of electromagnetic energy with rain are demonstrated and summarized below.

a. The complex refractive index of water is described adequately by a Debye relaxation-type formula for frequencies up to 300 GHz. The parameters to be used in this formula are listed in Table I; the asymptotic value for the dielectric constant at high frequencies (ε_∞) may be taken equal to 4.9 rather than 5.5 (Saxton 1952). The influence on the propagation parameters of a slight change in the refractive index of water is minor (a few percents) compared to the variations caused by other parameters.

b. The attenuation due to rain reaches a maximum for incident radiation having a free space wavelength of the order of 1.5 to 2 mm, depending on the rainfall intensity. The values of this maximum as a function of precipitation rate are listed below

rain intensity	150	100	50	12.5	mm/hr
max. attenuation	50 (36)	37 (26)	21 (15)	8 (6)	dB/km

The figures inside the bracket are the asymptotic values at optical wavelengths, obtained using the geometric cross-section. For frequencies up to 35 GHz the rainfall intensities that cause serious handicaps in propagation are in excess of 50 mm/hr.

c. The excess phase delay, as compared to free space propagation, is maximum in the 30 to 50 GHz band, depending on rainfall intensity. A phase lag of 180 deg/km is reached at 30 GHz for a 150 mm/hr rain. The apparent phase advance which is encountered at frequencies larger than 200 GHz in very intense rain, and at 600 GHz for all rainfall rates, does not exceed 30 deg/km, however.

d. No serious bandwidth limitations due to delay distortion are expected in the whole range considered. The dominant distortion effects occur in the region from 4 to 40 GHz and for rainfall rates larger than 25 mm/hr. A maximum change in the relative propagation time of 1.1 picosec/km/GHz is obtained at 4.5 GHz for a rainfall intensity of 150 mm/hr. More serious bandwidth limitations may occur due to the fluctuations of the propagation delay.

e. Drop diameters that yield the maximum attenuation vary from 7 mm to 0.5 mm when the frequency varies from 1 to 600 GHz. The smallest drops, however, always cause the maximum contribution to the imaginary part of the scattering function, which yields the phase shifts.

f. The attenuation coefficient is relatively insensitive to the drop-size distribution in a region around 35 GHz. This frequency marks the beginning of the frequency range for which small drops play the major role in the scattering process.

g. The sensitivity of both propagation parameters to the raindrop temperature is maximum in the regions where these parameters have their smallest values. For frequencies larger than 30 GHz, the influence of temperature on the attenuation coefficient is within $\pm$ 15% at all rainfall rates. For the excess phase, the correction for temperature changes is less than 10% for frequencies less than 150 GHz.

h. Small drops, and hence light rains, are sensitive to temperature up to the millimeter wavelengths range. Attenuation due to fog is expected to be very sensitive to temperature over the whole range considered. Also, a change of temperature in excess of 20 °C has less effect, usually, on the propagation parameters than a similar change in the reverse direction.

i. The correction factors for a change in temperature or drop-size distribution are of the order of several tens of percent; a variation in the drop velocity of a few m/sec produces changes of several hundred percent. This last factor is the only one that can explain the fact that certain measured values are about twice as large as the maximum theoretical value calculated.

j. The Laws and Parsons drop-size distribution seems to provide the best agreement between measured and predicted attenuation coefficient when a path-averaged rainfall rate is used. The tendency for the Marshall-Palmer distribution to exaggerate the number of small drops appears clearly to arise from the fact that this model predicts too much attenuation at frequencies larger than 50 GHz.

k. However, the Laws and Parsons distribution may underestimate the number of drops at low rainfall rates, since measurements have a tendency to lie above the predicted value at those rainfall intensities.

l. In view of the agreement between measurement and theory, the correction for forward scattering in the case of incoherent transmission systems seems to be negligible for frequencies up to 100 GHz at least.

The model developed in this study gives satisfactory results in estimating the average effects of rain on electromagnetic waves, when the influence of wind turbulence is taken into account. It could be improved by introducing a finite beam geometry and a shape factor for the receiving antenna, instead of assuming an infinite plane wave. Also polarization effects could be accounted for by considering raindrops of spheroidal shape. The question whether such a refinement of the theory is worthwhile, given the crude way in which meteorological parameters are handled, is a good one.

In this work, we have only been concerned with the statistical average value of the signal parameters after propagation through rain. But even in the case of spatially uniform rain, the signal will be phase and amplitude modulated, due to the random discrete structure of the medium. Frequency modulation may also occur if the random motion of the drops is sufficient to cause noticeable Doppler effect. Polarization fluctuations and cross-polarization effects will also be noticed in actual rain with non-spherical drops.

The design of microwave links requires a knowledge of the statistical outage time due to attenuation by rain. This can not be obtained from an average model; isolated attenuation spikes in excess of the average value play an important role. The uncertainty due to temperature fluctuations and to wind turbulence can be evaluated if adequate meteorological data are made available. The undetermination due to the drop-size distribution for a given rainfall rate, in the coherent case, may be bounded by considering the incoherent channel. In that case, the conditions for obtaining a

Rice-Nakagami distribution (independent scattering - $\sigma_n << N$) seem to be satisfied, and the mean and variance of the distribution are readily obtained (see also Oguchi 1962). Preliminary calculations of the standard deviation showed values less than 10% for all rainfall intensities and frequencies up to 100 GHz. Thus the fluctuations due to drop-size variation for a given rainfall rate seem negligible in comparison of the effects due to fluctuations of the rainfall intensity along the path. These effects still have to be evaluated. The problem looks very complicated, since it has been shown by Freeny and Gabbe (1969) that, for intense rain, the time series cannot even be considered as piecewise stationary, thus making the classical approach by means of the correlation function useless.

Although we consider this theory to give satisfactory results, the applicability of the Laws and Parsons drop-size distribution for predicting average effects in different types of rain remains to be demonstrated. In order to avoid measuring rainfall rates, experiments to establish this fact can be designed, using two different frequencies propagating along the same path (Semplak 1971). When doing so, it is expected that greater sensitivity can be attained by using two frequencies located on both sides of 35 GHz, the variation of the attenuation coefficient being of opposite directions for these two frequencies.

At the end of this study we should be able to answer the question: are the great expectations placed in the EHF band for channel capacity annihilated by atmospheric effects? Of all the atmospheric phenomena that have an effect on millimeter waves, rain is certainly the one that causes the most severe limitations. If a system is to be designed to overcome 40 dB of attenuation and yet maintain an acceptable signal-to-noise ratio, with an outage time less than 6 min. a year (which corresponds to the time per year a rainfall rate of 100 mm/hr is exceeded in New Jersey), the maximum repeater spacing decreases from 33 km at 6 GHz, to 4 km at 18.5 GHz, to 2 km at 30 GHz, and to only 1.4 km at 60 GHz. These figures illustrate the drastic effects of rain on millimeter waves which make such links practical only over short distances. However, intense rains, that exert the most severe effects, seldom occur over large areas; thus the path lengths could be slightly increased. But, although the electromagnetic aspect of the problem is adequately known, the meteorological data that would permit an optimum design of millimeter links through the use of path-diversity are still largely missing today.

The relatively short paths through the troposphere at high elevation angles make the use of millimeter wavelengths very attractive for earth-space links. But in this case too, the meteorological data for a slant path through the atmosphere are still largely unknown. How does the drop-size distribution vary with altitude, and how does this variation affect the attenuation coefficient? What is the relationship between ground measured rainfall rate and the path averaged rate? The cost of one unit of fade margin being very expensive in space communications, a more precise estimation of the atmospheric effecs would be justified in such a case. The average value of the path length through rain of a given intensity for an earth-space path is given by Hogg (1971). His values allowed us to calculate the order of magnitude of the attenuation due to rain to be expected in a satellite communication system at different frequencies. Attenuation up to 14 dB may be expected at 15.3 GHz in intense rain; values can reach 37 dB at 31.65 GHz and be in excess of 60 dB at 94 GHz. The first two figures do not seem to be excessive for a telecommunication link and allow us to conclude that these two candidate frequencies will be in use in the near future. Space diversity techniques will make the 94 GHz band more tractable in the far future. The values predicted by the theory show very good agreement with experimental data obtained from the ATS-V satellite (Ippolito 1971).

Although atmospheric effects are very annoying in the millimeter wavelengths range, radio-engineers have started to live with the problem and find ingenious ways for taking advantage of the great potentialities of this part of the electromagnetic spectrum. All that remains is that the need for a millimeter system be great enough to justify its cost.

BIBLIOGRAPHY

1. Abramowitz, M., Stegun, I.A., (1968), Handbook of Mathematical Functions, Dover ed. 1968, p. 437.

2. Aden, A.L., (1951), Electromagnetic Scattering from Spheres with Sizes Comparable to the Wavelength, Jour. of Appl. Physics, 22, 5, May 1951, pp. 601-605.

3. Babkin, Y.S., et al., (1970), Measurement of Attenuation in Rain over 1 km Path at a Wavelength of 0.96 mm, Radio Eng. and Electronic Physics, 15, 12, December 1970, pp. 2164-2166.

4. Beach, C.D., Brockway, R.J., (1970), A Review of Wave Propagation and Noise from 10 to 100 GHz, Westinghouse Georesearch Lab. Tech. Rep. 71-141-COMSY-R2, CCPE 605, December 70, Boulder, Colorado, 53 pages.

5. Blevis, B.C., et al., (1967), Measurements of Rainfall Attenuation at 8 and 15 GHz, IEEE Trans. AP, 15, 2, May 1967, pp. 394-403.

6. Bussey, H.E., (1950), Microwave Attenuation Statistics Estimated from Rainfall and Water Vapor Statistics, Proc. IRE, 38, 7, July 1950, pp. 781-785.

7. Chamberlain, J.E., et al., (1966), Submillimetre Absorption and Dispersion of Liquid Water, Nature, 210, 5, May 1966, p. 790.

8. Chandrasekhar, S., (1960), Radiative Transfer Theory Dover ed. New York 1960.

9. Chu, T.S., Hogg, D.C., (1968), Effects of Precipitation on Propagation at 0.63, 3.5, and 10.6 microns, Bell System Tech. Journal, 47, 5, May-June 1968, pp. 723-759.

10. Crane, R.K., (1966), Microwave Scattering Parameters for New England Rain, MIT Lincoln Lab Report 426, Lexington Mass., 3 Oct. 1966, AD 647798.

11. Crane, R.K., (1967), Coherent Pulse Transmission Through Rain, IEEE Trans. AP, 15, 2, March 67, pp. 252-256.

12. Crane, R.K., (1971), Propagation Phenomena Affecting Satellite Communication Systems Operating in

the Centimeter and Millimeter Wavelengths Bands, Proc. IEEE, 59, 2, Feb. 1971, pp. 173-188.

13. Debye, P., (1929), Polar Molecules, The Chemical Catalog Co. Inc. New York, Chapter 6.

14. Deirmendjian, D., (1963), Complete Microwave Scattering and Extinction Properties of Polydispersed Cloud and Rain Elements, Rep. RAND-R-422-PR, Rand Corp. Santa Monico Calif., December 1963, AD 426139.

15. Fannin, B.M., et al., (1971), Calculation of Rain Scattering Effects in Radiometric Measurements, Paper presented at the IEEE Meeting, Los Angeles, Calif., September 22-24, 1971, (Session 13).

16. Fowler, M.S., LaGrone, A.H., (1969), A Survey of Gaseous or Hydrometeors Absorption in the 10-100 GHz, University of Texas, Rep. P-37, October 1969, 108 pages, (exhaustive bibliography).

17. Freeny, A.E., Gabbe, J.D., (1969), A Statistical Description of Intense Rainfall, Bell System Tech. Journal, 48, 6, July-Aug, 1969, pp. 1789-1851.

18. Godard, S.L., (1970), Propagation of Centimeter and Millimeter Wavelengths through Precipitation, IEEE Trans. AP, 18, 4 July 1970, pp. 530-534.

19. Grant, E.H., et al., (1957), Dielectric Behavior of Water at Microwave Frequencies, J. Chem. Phys. 26, 1, Jan. 1957, 156.

20. Gunn, K.L.S., Kinzer, G.D., (1949), The Terminal Velocity of Fall for Water Droplets in Stagnant Air, J. Meteorol., 6, 4, p. 243.

21. Gunn, K.L.S., East, T.W.R., (1954), The Microwave Properties of Precipitation Particles, Quart. J. Roy. Meteorolog. Soc., 80, pp. 522-545.

22. Hardy, K.R., (1962), A Study of Raindrop Size Distribution and Their Variation with Height, University of Michigan, Rep. 05016-1-S, AFCRL 62-1091, 174 pages.

23. Harrold, T.W., (1967), Attenuation of 8.6 mm-wavelength Radiation in Rain, Proc. IEE, 114, 2, Feb. 1967, 201-203.

24. Hogg, D.C., (1967), Path Diversity in Propagation of Millimeter Waves Through Rain, IEEE Trans. AP, 15, pp. 410-415.

25. Hogg, D.C., (1968), Millimeter-Wave Communication Through the Atmosphere, Science, 159, 3810, Jan. 1968, pp. 39-46.

26. Hogg, D.C., (1968), Statistics on Attenuation of Microwaves by Intense Rain, Bell Syst. Tech. J., 48, 9, Nov. 1969, 2949-2962.

27. Hogg, D.C., (1971), Rain on Earth-Space Paths, Paper presented at the IEEE Meeting in Los Angeles, Calif., Sept. 22-24, 1971, Session 13.

28. Van de Hulst, H.C., (1957), Light Scattering by Small Particles, John Wiley, New York , 1957.

29. Ippolito, L.J., (1971), Effects of Precipitation on 15.3- and 31.65- GHz Earth-Space Transmissions with the ATS-V Satellite, Proc. IEEE, 59, 2, Feb. 1971, pp. 189-205.

30. Jones, P.M.A., (1959), The Shape of Raindrops, J. Meteorol., 16, 1959, pp. 504-510.

31. Kerker, M., (1969), The Scattering of Light and other Electromagnetic Radiation, Academic Press, New York, 1969.

32. Kerr, D.E., (ed.), (1951), Propagation of Short Radio Waves, MIT Rad. Lab Series, Vol. 13, McGraw Hill, New York, 1951.

33. Lammers, U., (1967), The Attenuation of mm Waves by Meteorological Precipitation, Neue Technische Zeitschrift--Comm. Journal (English ed.), N. 516, pp. 230-236.

34. Lane, J.A., Saxton, J.A., (1952), Dielectric Dispersion in Pure Polar Liquids at Very High Radio Frequencies Part I, Proc. Roy. Soc. London, A 213, p. 400.

35. Laws, J.O., Parsons, D.A., (1943), The Relation of Rain Drop-Size to Intensity, Trans. Amer. Geophys. Union, 24, 1943, pp. 452-460.

36. Lerner, R.M., Holland, A.E., (1970), The Optical Scatter Channel, Proc. IEEE, 58, 10, October 70, pp. 1547-1563.

60. Setzer, D.E., (1971), Anisotropic Scattering Due to Rain at Radio-Relay Frequencies, Bell Syst. Tech. Journal, 50, 3, March 1971, pp. 861-868.

61. Skerjanec, R.E., Samson, G.A., (1971), Rain Attenuation Measurements in Mississippi, IEEE Trans. AP, 19, 4, July 1971, pp. 575-578.

62. Stanevich, A.E., Yaroslavskii, N.G., (1961), Absorption of Liquid Water in the Long Wavelength Part of the Infrared Spectrum (42-2000μ), Optics and Spectroscopy, 10, 4, April 1961, pp. 278-279.

63. Straiton, A.W., et al., (1970), Amplitude Variations of 15 GHz Radio Waves Transmitted Through Clear Air and Through Rain, Radio Science, 5, 3, March 1970, pp. 551-557.

64. Straiton, A.W., et al., (1971), Propagation of 15.3 and 35 GHz over a 15.5 km Path, Paper presented at the IEEE Meeting in Los Angeles, Calif. Sept. 22-24, 1971, Session 13.

65. Stratton, J.A., (1941), Electromagnetic Theory, McGraw Hill, New York, 1941, pp. 563-573.

66. Thomas, D.T., (1971), Cross-Polarization Distortion in Microwave Radio Transmission Due to Rain, Radio Science, 6, 10, Oct. 71, pp. 833-839.

67. Twersky, V., (1962), On Scattering of Waves by Random Distributions. Part I: Free Space Scatterer Formalism, Journ. of Math Phys., 3, 4, July-Aug 1962, pp. 700-715.

68. Weibel, G.E., Dressel, H.O., (1967), Propagation Studies in Millimeter-Wave Link Systems, Proc. IEEE, 55, 4, April 67, pp. 497-513.

APPENDIX 1

DATA FOR THE COMPLEX REFRACTIVE INDEX OF WATER

This appendix presents the variation of the real and imaginary part of $\hat{m}$ versus frequency. It was plotted in the complex plane in Figure 1 (Chapter 2). The real part is a measure of the excess phase delay and the imaginary part of the excess attenuation over free space propagation, according to:

$$\exp(-jk_o\hat{m}l) = \exp(-k_o m''l) \cdot \exp(-jk_o m'l) \qquad (1)$$

Those curves are typical for non-resonant, viscously damped, Debye type absorption phenomena. The effect of an increase in temperature is to shift the breaking point of the real part and the absorption peak of the imaginary part towards higher frequencies (see Figures I.1 and I.2). Practically, all these phenomena occur in the cm and mm wavelength region; the absorption for 20°C has its peak around 30 GHz (1 cm). Real and imaginary part do not vary independently; they are related by the so-called Krönig-Kramers relationship. Some values of the refractive index of water, for selected wavelengths, are listed in Table I.3.

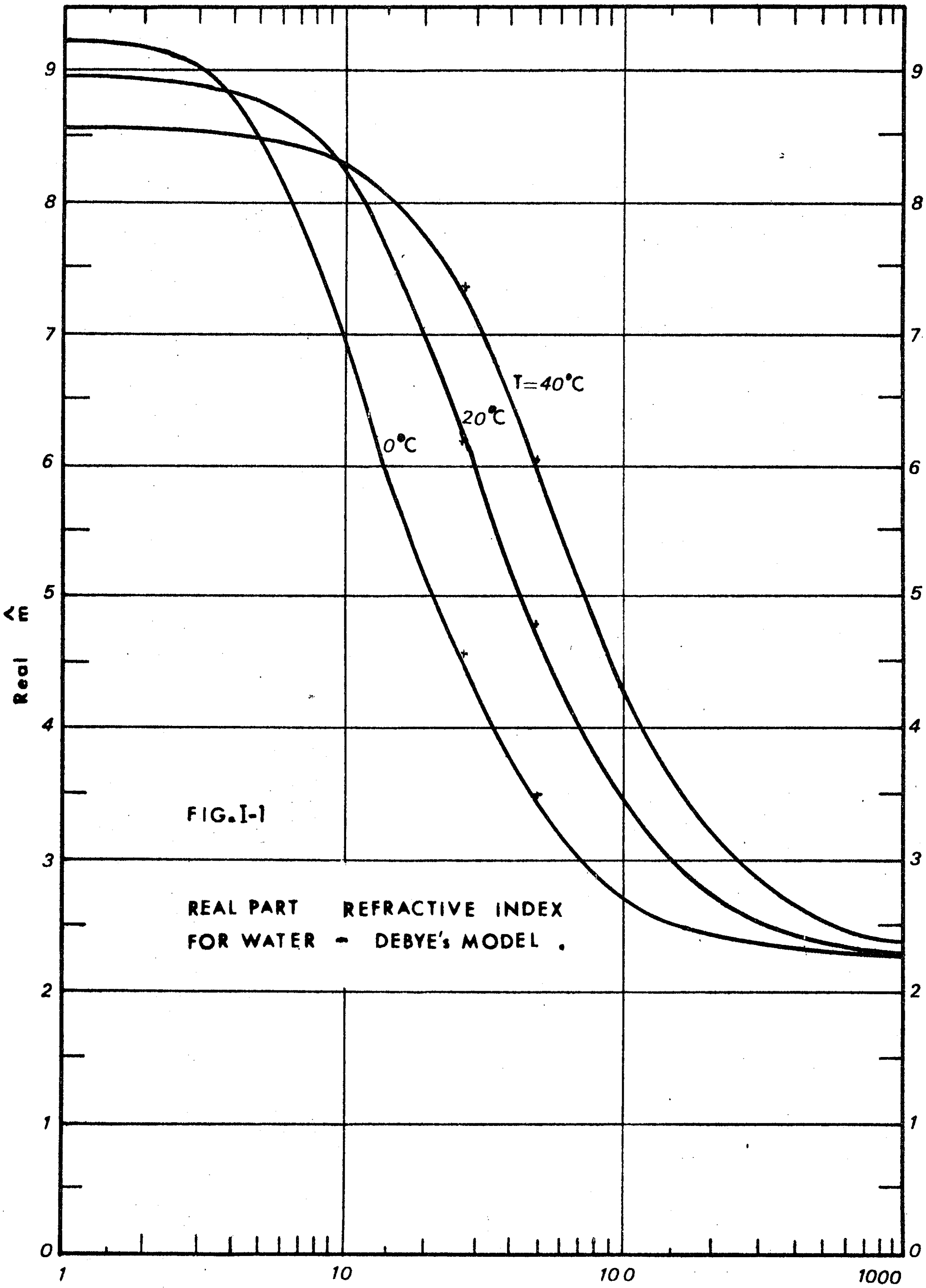

FIG. I-1 FREQUENCY GHz

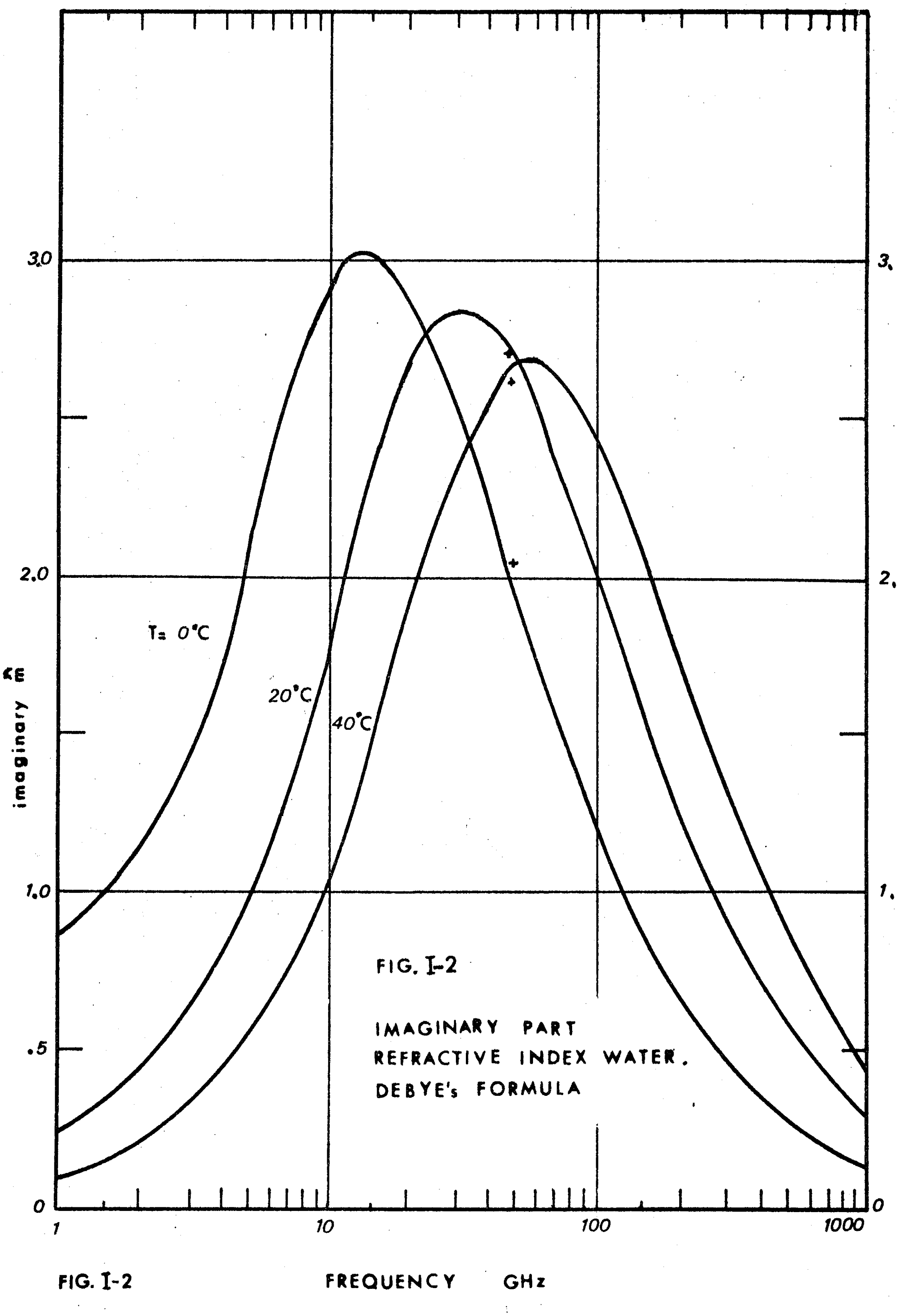
3.0
2.0
1.0
.5
0
3.
2.
1.
0
1
10
100
1000
imaginary m
T= 0°C
20°C
40°C
FIG. I-2
IMAGINARY PART
REFRACTIVE INDEX WATER.
DEBYE's FORMULA
FREQUENCY GHz

FIG. I-2

Wavelength [cm]	Frequency [GHz]	Index (10°C)	Index (20°C)
10	3	9.006-j0.930	8.871-j0.628
7.5	4	8.890-j1.211	8.815-j0.828
5	6	8.590-j1.705	8.664-j1.203
3.2	9.4	7.971-j2.313	8.317-j1.743
2	15	6.943-j2.808	7.620-j2.359
1.62	18.5	6.399-j2.913	7.182-j2.589
0.86	35	4.802-j2.735	5.607-j2-838
0.62	48.5	4.130-j2.443	4.821-j2.689
0.43	70	3.537-j2.054	4.077-j2.380
0.3	100	3.106-j1.663	3.505-j2.007
0.2	150	2.773-j1.254	3.039-j1.575
0.1	300	2.481-j0.705	2.587-j0.937

TABLE I-3

SOME SELECTED VALUES OF THE REFRACTIVE INDEX
FOR LIQUID WATER, USING DEBYE'S FORMULA

APPENDIX 2

A SUBROUTINE FOR CALCULATING THE MIE COEFFICIENTS

2.1. The method of the logarithmic derivative function

This appendix is a treatment of the numerical computation of Mie's coefficients given in Chapter 3 (formulas 3.9 and 3.10). The convergence of those series is examined for a particular example and an evaluation of the required number of terms, for a reasonable accuracy, is also presented. A listing of the Fortran subroutine for computing the coefficients is included at the end of this appendix.

It can be shown (e.g. see Aden (1951)) that, by introducing the function

$$\sigma_n(x) = \frac{d}{dx} \ln(x \cdot j_n(x)) \qquad (1)$$

the expressions (3.9) and (3.10) for $\hat{a}_n$ and $\hat{b}_n$ reduce to:

$$\hat{a}_n = \frac{j_n(z)\sigma_n(\hat{m}z) - \hat{m}\left(j_{n-1}(z) - \frac{n}{z} j_n(z)\right)}{h_n^{(2)}(z)\sigma_n(\hat{m}z) - \hat{m}\left(h_{n-1}^{(2)}(z) - \frac{n}{z} h_n^{(2)}(z)\right)} \qquad (2)$$

$$\hat{b}_n = \frac{j_{n-1}(z) - \frac{n}{z} j_n(z) - \hat{m}\sigma_n(\hat{m}z)\; j_n(z)}{h_{n-1}^{(2)}(z) - \frac{n}{z} h_n^{(2)}(z) - \hat{m}\sigma_n(\hat{m}z) h_n^{(2)}(z)} \qquad (3)$$

Notice that $\hat{a}_n$ and $\hat{b}_n$ in Aden's paper are of opposite sign and interchanged with ours.

The functions $j_n(z)$ and $h_n^{(2)}(z)$ can be evaluated by the classical formula for spherical Bessel functions

$$f_n(z) = (2n-1)\,\frac{f_{n-1}(z)}{z} - f_{n-2}(z) \tag{4}$$

with $$h_n^{(2)}(z) = j_n(z) - i\,y_n(z) \tag{5}$$

and

$$j_o(z) = y_{-1}(z) = \sin(z)/z \tag{6}$$

$$j_{-1}(z) = -y_o(z) = \cos(z)/z \tag{7}$$

The advantage of this procedure lies in the fact that there exists also a recurrence formula for $\sigma_n(\hat{m}z)$

$$\sigma_n(\hat{m}z) = \frac{(\hat{m}z)^2 - n(\hat{m}z)\;\sigma_{n-1}(\hat{m}z) - n^2}{n(\hat{m}z) - (\hat{m}z)^2\;\sigma_{n-1}(\hat{m}z)} \tag{8}$$

with

$$\sigma_o(\hat{m}z) = \cot\;(\hat{m}z) \tag{9}$$

Thus, by writing the classical solution for the scattering function coefficients in terms of a suitably defined logarithmic derivative function, the coefficients can be calculated by formulas from which all derivatives have disappeared. All the functions treated can be evaluated by simple recurrence formulas.

Since recurrence formulas accumulate errors at each step, we have to work with double-precision arithmetic in the computer; the price we have to pay for that, since double-precision complex numbers are not allowed, is to separate those expressions into their real and imaginary part, which is a tedious but straightforward job.

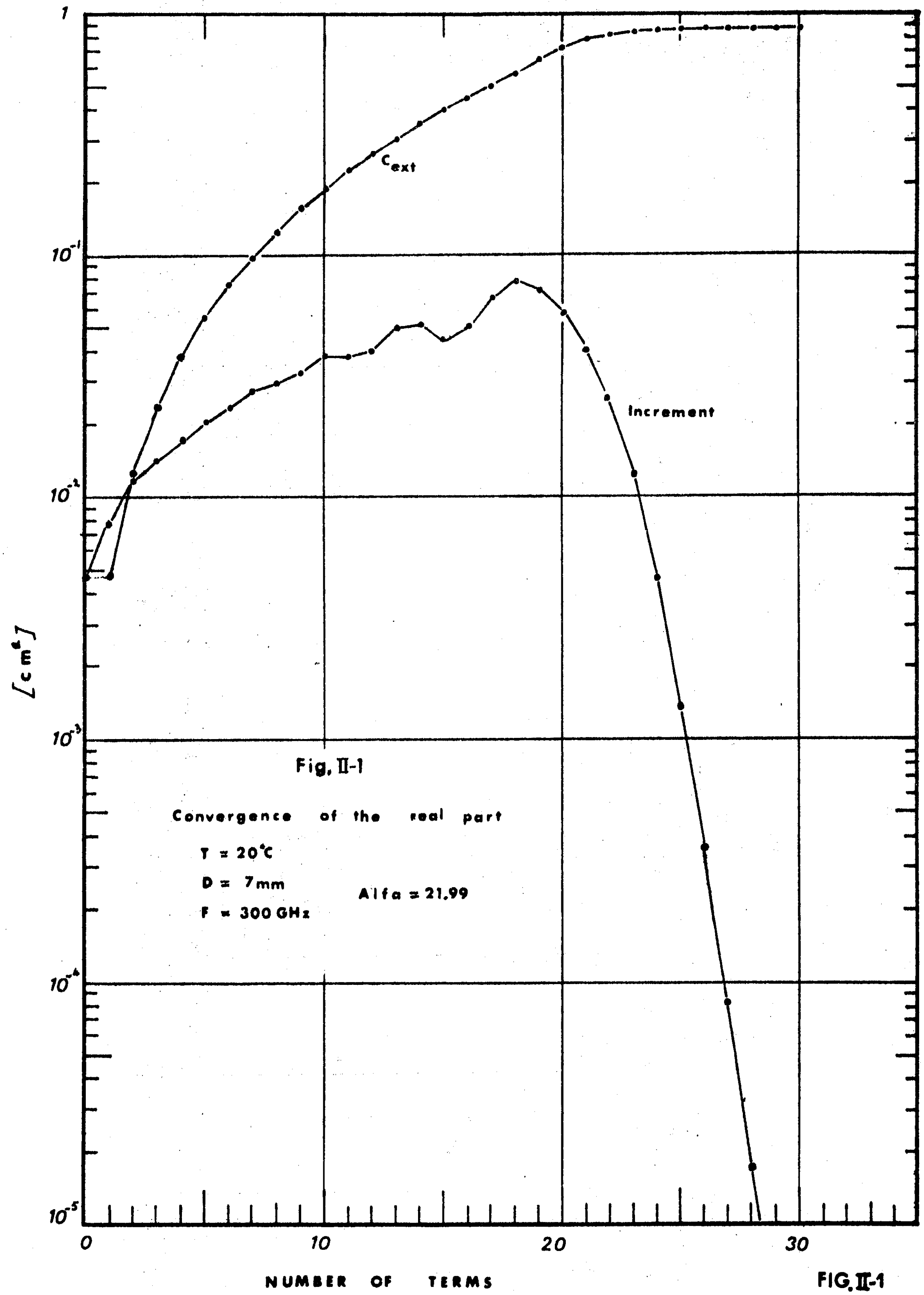
1
10^{-1}
10^{-2}
10^{-3}
10^{-4}
10^{-5}
$[cm^2]$
C_{ext}
Increment
Fig, II-1
Convergence of the real part
T = 20°C
D = 7mm
F = 300 GHz
Alfa = 21.99
0
10
20
30
NUMBER OF TERMS

FIG. II-1

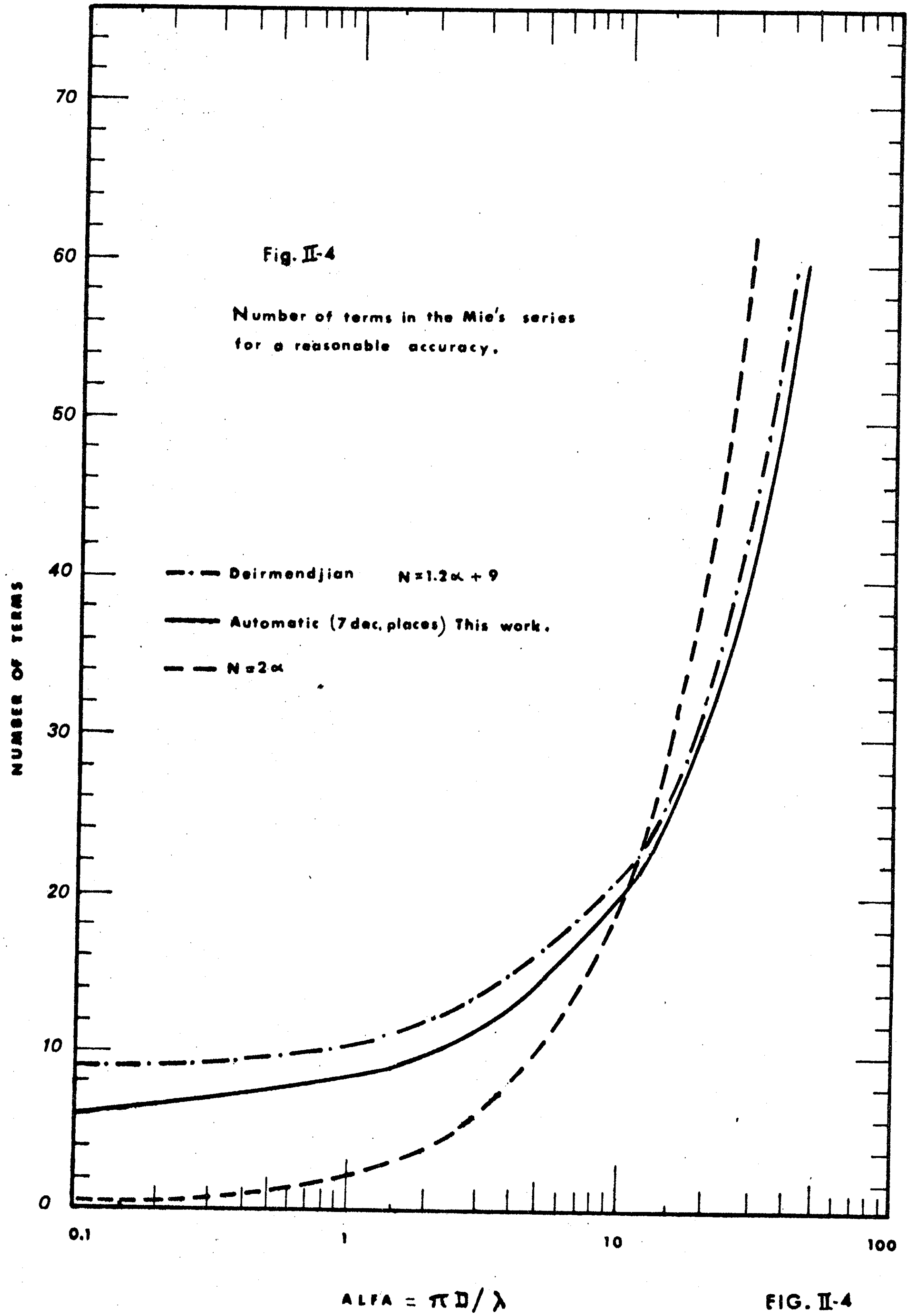
Fig. II-4
Number of terms in the Mie's series
for a reasonable accuracy.
Deirmendjian N = 1.2α + 9
Automatic (7 dec. places) This work.
N = 2α
NUMBER OF TERMS
0
10
20
30
40
50
60
70
0.1
1
10
100
ALFA = πD/λ

FIG. II-4

expressions for these functions should be used instead of the recurrence relation, whenever $n >> |\hat{m}z|$.

The convergence of this subroutine has nevertheless been tested at optical wavelengths, where the extinction cross-section was found to converge in an oscillatory manner towards twice the value of the geometrical cross-section.

If the Fortran program, as written, is not optimum for calculating the Mie coefficients for raindrops in the infrared region, it is perfectly suitable for evaluating the effect of fog up to visible frequencies. Fog droplets reach their Mie region in the near infrared only, and the number of iterations still remains reasonable.

In the case of rain at visible frequencies, the geometric cross-section approximation seems to be a reasonable one.

2.3. Subroutine ADEN

The input variables of this subroutine are

WAVE : free-space wavelength in cm (double-precision)

R : raindrop radius in cm (double-precision)

EN1,EN2: real (imaginary) part of the complex refractive index of water (double-precision)

EC,ED : real (imaginary) part of the complex dielectric constant for water.

The output values are the efficiency factors (normalized cross-sections) as defined in Chapter 3.

QAN : absorption

QSN : scattering

QTN : extinction

QIN : imaginary

SBACK : backward-scattering

SFOR : forward-scattering

The Mie coefficients are represented inside the program by ANSR + j ANSI = $\hat{a}_n$, and BNSR + j BNSI = $\hat{b}_n$.

This subroutine uses the Rayleigh approximation for values of the Mie parameter less than 0.01. The number of iterations can be adjusted, according to the number of accurate decimal places desired. Finally, this program has been written for a CDC 6400 system. A listing of the subroutine is presented next.

```
      SUBROUTINE ADEN(WAVE,R,EN1,EN2,EC,ED,QAN,QSN,
     1QTN,QIN,SBACK,SFOR)

               *  *  *  *  *  *  *   *

      TYPE DOUBLE WAVE,R,EN1,EN2,ALFA,PI,SIGOR,
     1SIGOI,U,V,BESA,BESB,BESC,
     2EM,YMA,YMB,YMC,SEM,TEM,SM,TM,A,B,C,D,SIGAR,
     3SIGAI,EMA,
     4ANSR,ANSI,QEM,REM,BNSR,BNSI
      TYPE DOUBLE D1,COEF,SUMSRB,SUMSIB,SUMS
      TYPE COMPLEX EPS,ANS,BNS,ID
      ID=(0.,1.)
      EPS=EC + ID*ED
      DM=2.*R
      PI=3.14159265358979323846264338З DO
      AREA = PI*(R**2)
      ALFA = (2.DO*PI*R)/WAVE
      Z=ALFA
      COEF = (WAVE**2)/(2.0DO*PI)
      IF(Z.LT.0.01)  31,32
C
C     RAYLEIGH REGION     ***********************
C
   31 I=0
      ANS=-(ID/15.)*(EPS - 1.)*(Z**5)
      BNS=-(2.*ID)*((EPS-1.)/(EPS+2.))*(Z**3)*
     1(1.+.6*((EPS-2.)/(EPS+2.))
     2*(Z**2) -(.666666*ID)*((EPS-1.)/(EPS+2.))*
     3(Z**3))-(3.*ID) *
     4 ((EPS-1.)/(2.*EPS+3))*(Z**5)
      X1=REAL (ANS)
      X2=AIMAG(ANS)
      X3=REAL(BNS)
      X4=AIMAG(BNS)
      QS=((WAVE**2)/(2.0DO*PI))*((X1**2)+(X2**2)+
     1(X3**2)+(X4**2))
      QT=-(WAVE**2)/(2.*PI)*(X1+X3)
      QI=-(WAVE**2)/(2.*PI)*(X2+X4)
      QA=QT-QS
      QSN=QS/AREA   $ QAN=QA/AREA   $  QTN=QT/AREA
      QIN=QI/AREA
      SFOR=(1./(Z**2))*((X1+X3)**2+(X2+X4)**2)
      SBACK = 1.5*QSN
      GO TO 45
```

```
C
C     MIE  REGION  ******************************
C
C
C     FIRST  STEP    *****     ( N=0 )
C
   32 I=1
      U=2.D0*ALFA*EN1
      V=2.D0*ALFA*EN2
      SIGOR=DSIN(U)/((DEXP(V)+DEXP(-V))/2.0D0 - DCOS(U))
      SIGOI=((DEXP(V)-DEXP(-V))/2.0D0)/((DEXP(V)+
     1DEXP(-V))/2.0D0-DCOS(U))
      BESA = DCOS(ALFA)/ALFA
      BESB = DSIN(ALFA)/ALFA
      YMA=BESB
      YMB=-BESA
      X1=0.0   $X2=0.0   $X3=0.0   $X4=0.0
      X6=0.0    $ X7=0.0
      QS=0.0
      QT1=0.0
      KT=0
C
C     START  ITERATIONS    **********************
C
   36 EM=I
      BESC=(2.0D0*EM-1.D0)*BESB/ALFA - BESA
      YMC = (2.D0*EM -1.D0)*YMB/ALFA -YMA
      SM=EN1*SIGOR + EN2*SIGOI
      TM = EN1*SIGOI - EN2 * SIGOR
      A = (ALFA**2)*((EN1**2)-(EN2**2))-(EM**2)+
     1EM*ALFA*SM
      B = EM*ALFA*TM - 2.D0*EN1*EN2*(ALFA**2)
      C = ALFA*(EM*EN1-((EN1**2)-(EN2**2))*ALFA*
     1SIGOR-2.D0*EN1*EN2*ALFA*SIGOI)
      D = ALFA*(2.D0*EN1*EN2*ALFA*SIGOR -((EN1**2)-
     1(EN2**2))*ALFA*SIGOI-EM*EN2)
      CALL SEPAR (A,B,C,D,SIGAR,SIGAI)
      SEM = EN1*SIGAR+EN2*SIGAI
      TEM = EN1*SIGAI - EN2*SIGAR
      EMA = EM/ALFA  + SEM
      A = BESB -EMA*BESC
      B = - BESC*TEM
      C = BESB - BESC*EMA -YMC * TEM
      D = EMA*YMC - YMB - BESC*TEM
      CALL SEPAR(A,B,C,D,ANSR,ANSI)
      QEM = BESB - EM * BESC / ALFA
      REM = YMB - EM * YMC/ALFA
```

```
      A= BESC*SIGAR - EN1*QEM
      B = BESC * SIGAI + EN2*QEM
      C= BESC*SIGAR + YMC*SIGAI - EN1*QEM + EN2*REM
      D=BESC*SIGAI - YMC*SIGAR + EN1*REM+EN2*QEM
      CALL SEPAR (A,B,C,D,BNSR,BNSI)
      BESA=BESB
      BESB=BESC
      YMA=YMB
      YMB=YMC
      SIGOR = SIGAR
      SIGOI = SIGAI
      D1=-(2.D0*EM+1.D0)
      X1=X1+D1*ANSR
      X2=X2+D1*ANSI
      X3=X3+D1*BNSR
      X4=X4+D1*BNSI
      SUMS=COEF*((ANSR**2)+(ANSI**2)+(BNSR**2)+
     1(BNSI**2))*(2.0D0*EM+1.0D0)
      SUMSRB=D1*(ANSR-BNSR)*((-1.)**I)
      SUMSIB= D1*(ANSI-BNSI)*((-1.)**I)
      QS=QS+SUMS
      X6=X6+SUMSRB
      X7=X7+SUMSIB
      X5=X1+X3
C
C     AUTOMATIC  CONVERGENCE  CRITERION *********
C
      QTT=ABS((X5-QT1)/X5)
C
C     SET FOR 6 DECIMAL PLACES -----------------
C
      IF(QTT.LT.5.E-7)  83,84
   84 I=I+1
      KT=0
      QT1=X5
      GO TO 36
   83 KT=KT+1
      IF(KT.GE.4)  86,87
   87 I=I+1
      QT1=X5
      GO TO 36
C
```

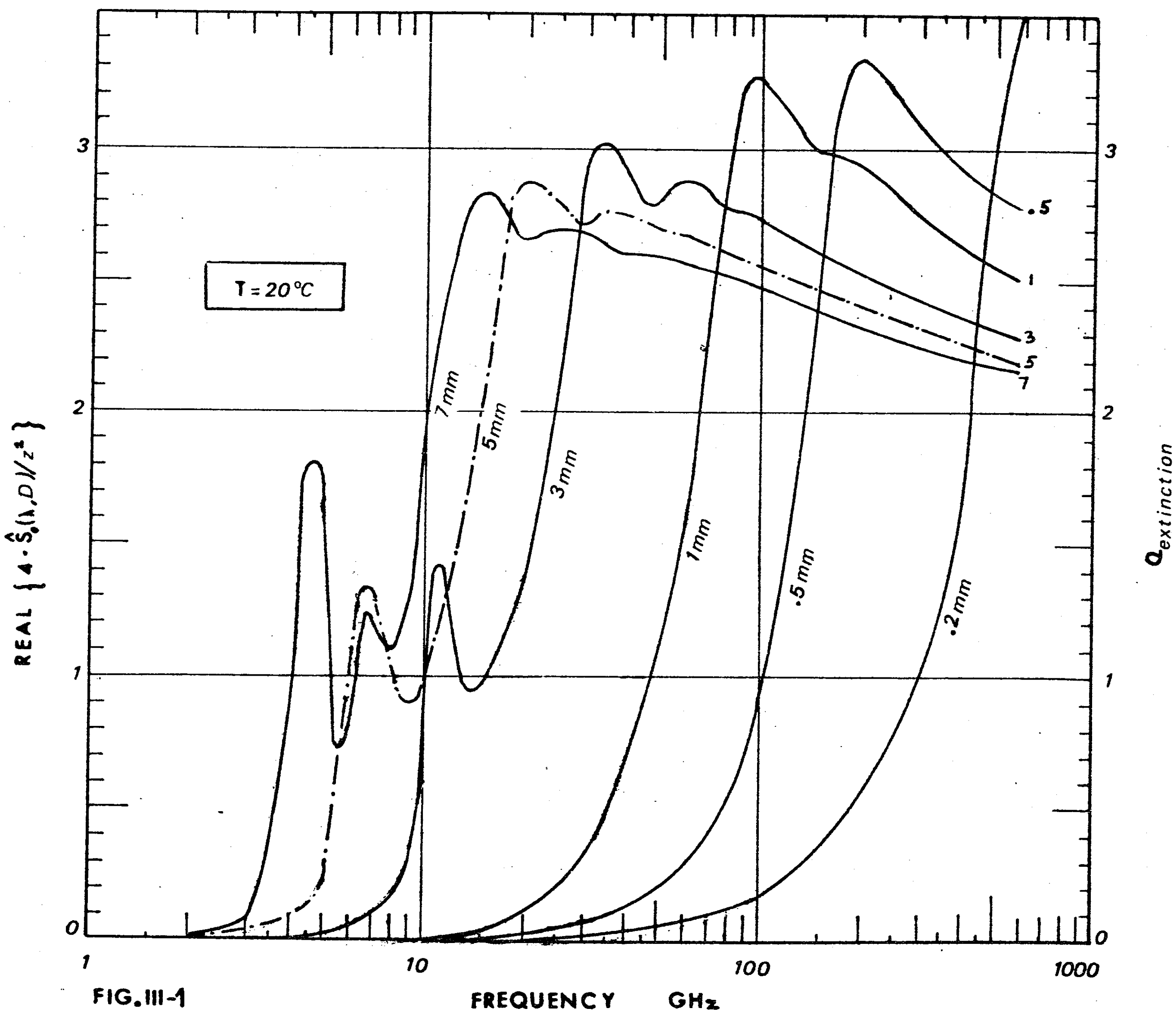
T = 20°C
7 mm
5 mm
3 mm
1 mm
.5 mm
.2 mm
.5
1
3
5
7
REAL $\{4 \cdot \hat{S}_o(\lambda, D)/z^2\}$
$Q_{extinction}$
0
1
2
3
1
10
100
1000
FREQUENCY GHz

FIG. III-1

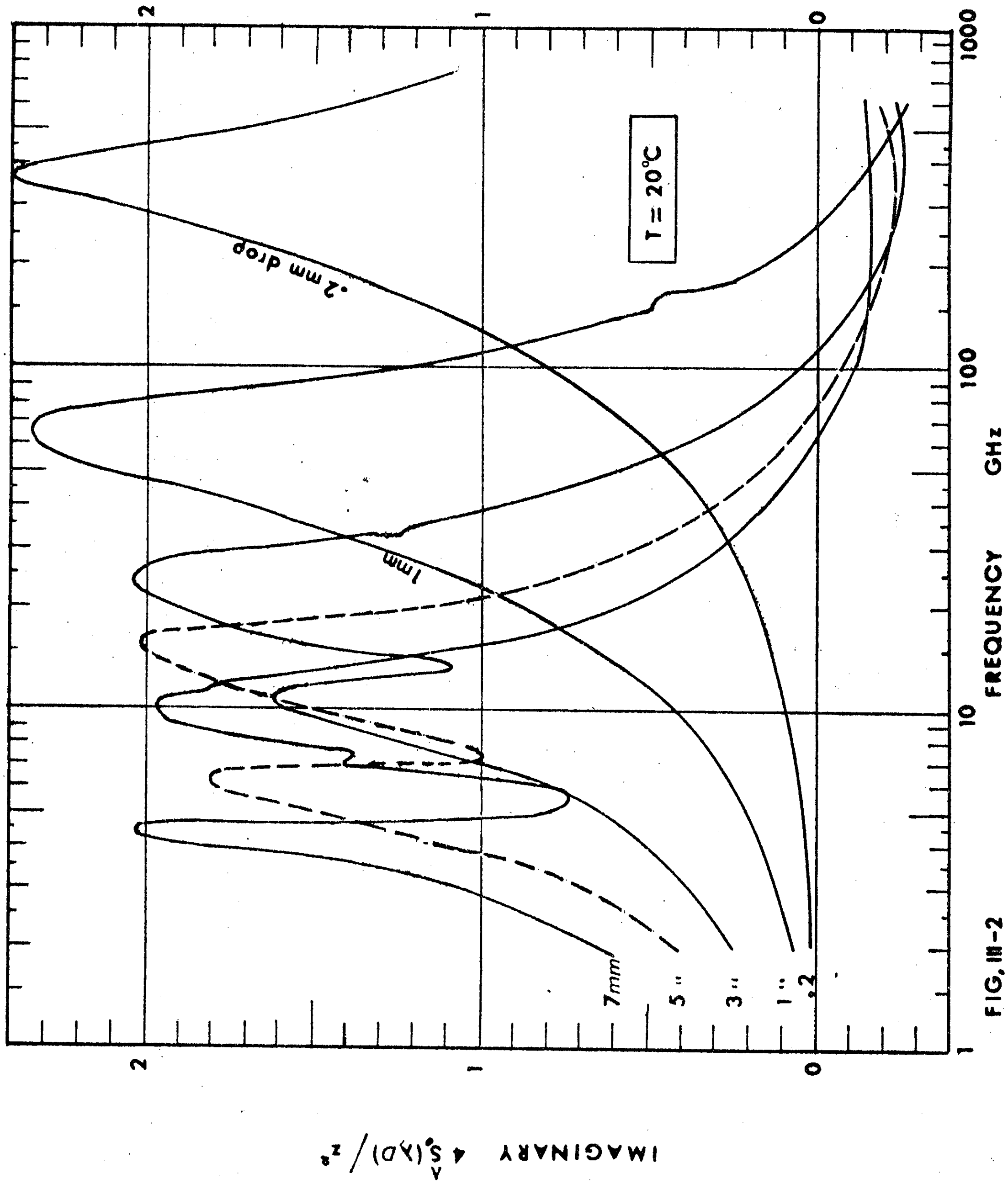
T = 20°C
.2 mm drop
1mm
7mm
5 "
3 "
1 "
.2
FREQUENCY GHz
1
10
100
1000
0
1
2
IMAGINARY 4 Ŝ(λD)/z²

FIG. III-2

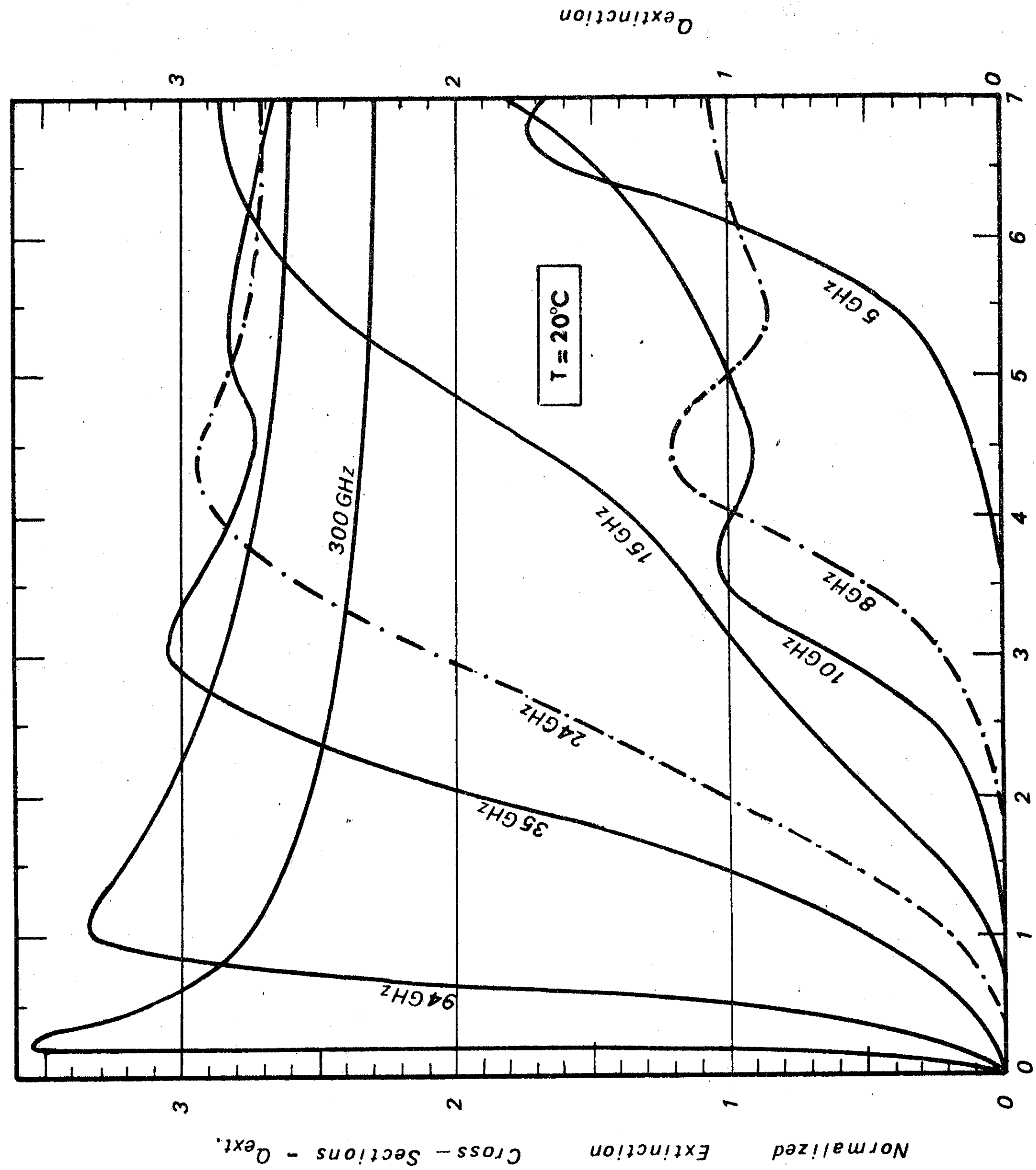
Q extinction
0
1
2
3
T = 20°C
5 GHz
8 GHz
10 GHz
15 GHz
24 GHz
35 GHz
94 GHz
300 GHz
DROP DIAMETER (mm)
Normalized Extinction Cross – Sections – Q ext.

FIG. III-3

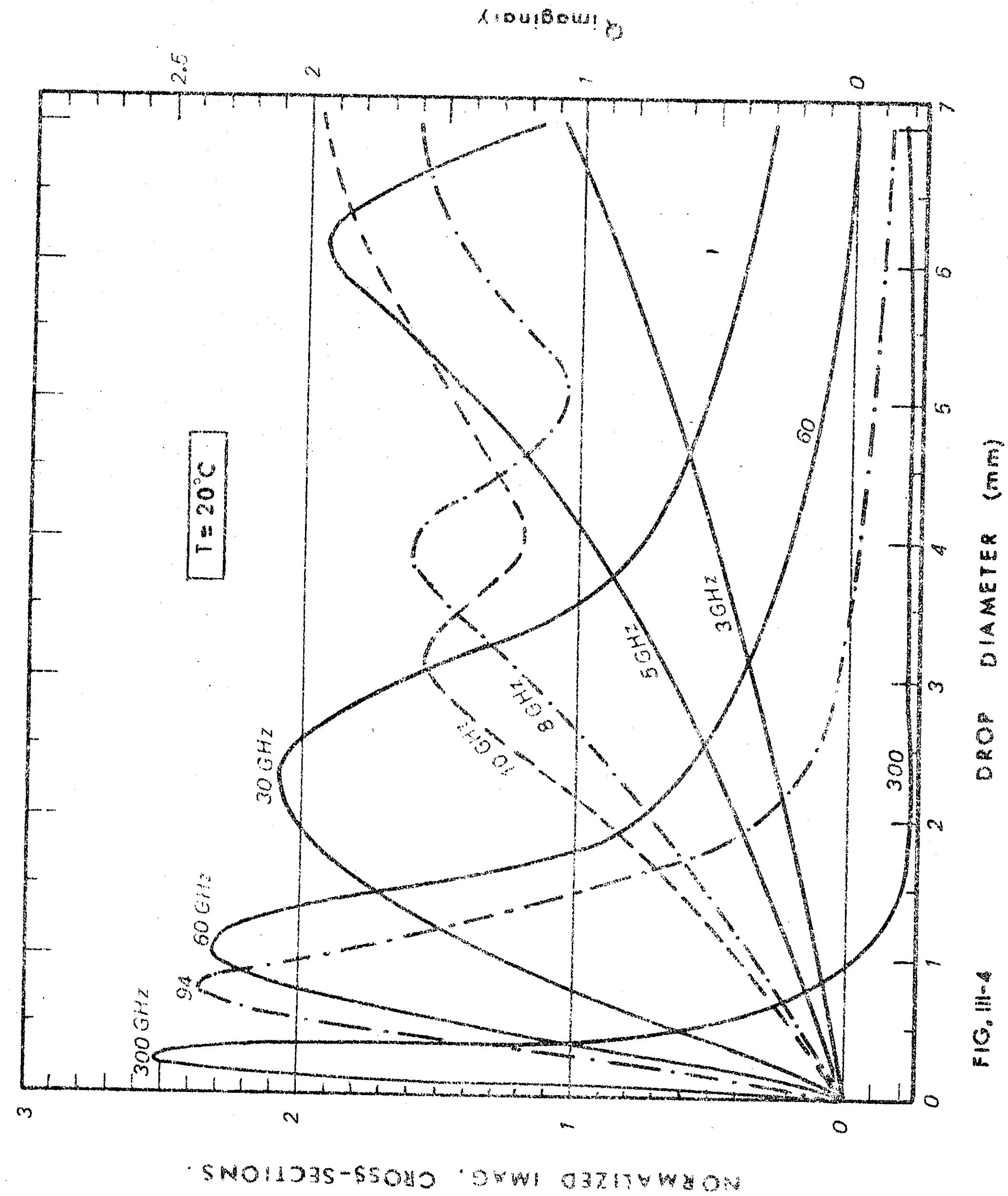
T = 20°C
300 GHz
94
60 GHz
30 GHz
10 GHz
8 GHz
5 GHz
3 GHz
60
300
DROP DIAMETER (mm)
NORMALIZED IMAG. CROSS-SECTIONS.
Q imaginary

FIG. III-4